



School of Physics and Astronomy  
University of Birmingham  
Edgbaston  
Birmingham  
B15 2TT

---



<sup>1</sup>

# Linear Electron Positron International Collider Design Report

March 27, 2015

Lucy BIGNELL  
Aaron BYRNE  
Andrew CLARKE  
John COTTERILL  
Adrian CROSS  
Thomas DACK  
Raveena DEOL  
Chris FRANCIS  
Daniel HATTON  
Matthew HEATH  
Ryan JONES  
Antony JUDD  
Thomas LANE  
Lewis SIMMONS  
Dwayne SPITERI  
Russell TURNER

---

<sup>1</sup>LEPIC logo designed by Gala Jackson-Coombs (Gala@prettyneatdesign.com)

## **Abstract written by Daniel Hatton and Lewis Simmons**

This report outlines the feasibilities of a future high energy electron-positron linear collider system. The proposed centre of mass energy for the various phases of experimentation are 300GeV, 1TeV, 3TeV and 6 TeV in order to precisely investigate the Standard Model (SM) Higgs boson and to conduct searches for theorised heavy particles at the TeV scale. The focus of these heavy particle searches will be the Supersymmetric (SUSY) and U(1) gauge group extensions to the SM.

1. The Higgs phase will aim to verify LHC results as well as improve upon these using a cleaner electron-positron collider environment, in which there are lower hadronic backgrounds. In particular the branching ratios for a variety of decay channels will be isolated to a higher precision. For instance the  $b\bar{b}$  branching ratio will be investigated to a theorised precision of 0.12% and the  $WW$  ratio to 0.44%. Certain decay modes have been excluded from investigation due to luminosity constraints.
2. Experimentation on SUSY models will occur at the 1 and 3 TeV energies. Simulations indicate that within regions of the Next to Minimally Supersymmetric Standard Model (NMSSM) parameter space a range of new particles can be excluded up to a mass of 1.5 TeV within the scope of this collider design. This exclusion may be achievable with  $1510 fb^{-1}$  of data at both 1 and 3 TeV energies.
3. Additional neutral heavy gauge bosons resulting from SM U(1) gauge group extensions will also be examined. In particular, an electron-positron environment is ideal for producing theorised  $Z'$  bosons. Running at 6 TeV, simulations have displayed that it is possible to exclude these particles up to a mass of  $\sim 6 TeV$  via direct production and approximately  $10 TeV$  via indirect methods.

The collider system features a single detector which has been designed to be sufficient for investigating the above areas with desired resolutions.

## **Acknowledgements**

We would like to acknowledge the support of Dr. Chris Hawkes, Dr. Nigel Watson and Dr. Juraj Bracinik throughout the undertaking of this project. We would also like to thank Dr. Paul Thompson for taking the time to give us feedback on our final seminar. Our thanks also goes to Gala Jackson-Coombs for designing the LEPIC logo.

# Contents

<b>1 Project Brief written by Russell Turner and Dwayne Spiteri</b>	<b>7</b>
<b>2 The Standard Model Higgs Boson</b>	<b>8</b>
2.1 Introduction <i>written by Matthew Heath</i> . . . . .	8
2.2 The Higgs Field . . . . .	9
2.2.1 Justification <i>written by Russell Turner</i> . . . . .	9
2.2.2 Implications on Measurable Quantities <i>written by Ryan Jones</i> . . . . .	10
2.3 Higgs Production <i>written by Andrew Clarke</i> . . . . .	11
2.3.1 Higgs-Strahlung . . . . .	12
2.3.2 W and Z fusion . . . . .	12
2.3.3 Radiation Off of Tops . . . . .	13
2.3.4 Double Higgs Production . . . . .	13
2.3.5 Cross-sections of the Production Processes . . . . .	14
2.4 Higgs Decays <i>written by Aaron Byrne</i> . . . . .	15
2.4.1 Higgs Decay Processes . . . . .	15
2.4.2 Higgs Decay Branching Ratios . . . . .	15
2.5 Coupling <i>written by Raveena Deol</i> . . . . .	16
2.5.1 Higgs Coupling to Fermions <i>written by Ryan Jones</i> . . . . .	17
2.5.2 Higgs Coupling to Photons <i>written by Russell Turner</i> . . . . .	17
2.5.3 Higgs Coupling to Weak Bosons <i>written by Matthew Heath</i> . . . . .	18
2.5.4 Higgs Self-Coupling <i>written by Raveena Deol</i> . . . . .	19
2.6 Other Higgs Properties . . . . .	21
2.6.1 Mass <i>written by Andrew Clarke</i> . . . . .	21
2.6.2 Spin and Parity <i>written by Aaron Byrne</i> . . . . .	23
2.7 Required Collider Parameters <i>written by Thomas Lane</i> . . . . .	24
2.7.1 Luminosity . . . . .	24
2.7.2 Energy . . . . .	26
<b>3 Beyond the Standard Model</b>	<b>27</b>
3.1 Introduction <i>written by Christopher Francis</i> . . . . .	27
3.2 Unexplored Considerations . . . . .	27
3.2.1 Compositeness <i>written by Dwayne Spiteri</i> . . . . .	27
3.2.2 Extra Dimensions <i>written by Christopher Francis</i> . . . . .	27
3.2.3 Technicolour <i>written by Lewis Simmons and John Cotterill</i> . . . . .	27
3.3 Exotic Heavy Neutral Gauge Bosons . . . . .	28
3.3.1 Introduction to Z' <i>written by Lewis Simmons</i> . . . . .	28
3.3.2 Motivations <i>written by Lewis Simmons</i> . . . . .	28
3.3.3 Search Strategy and Current Limits <i>written by Lewis Simmons</i> . . . . .	30
3.3.4 Detector Mechanisms <i>written by John Cotterill</i> . . . . .	30
3.3.5 Ramifications for the Detector <i>written by John Cotterill</i> . . . . .	34
3.4 Supersymmetric Extensions of the Standard Model . . . . .	35
3.4.1 Model Summary <i>written by Christopher Francis and Adrian Cross</i> . . . . .	35
3.4.2 Motivations <i>written by Daniel Hatton</i> . . . . .	35
3.4.3 Benchmarking . . . . .	36
3.4.4 Simulation Methodology <i>written by Dwayne Spiteri</i> . . . . .	38
3.4.5 Sparticles Phenomenology and Search Strategy . . . . .	39
3.5 Conclusion <i>written by Christopher Francis</i> . . . . .	48
<b>4 The Collider Design</b>	<b>49</b>
4.1 Introduction <i>written by Lucy Bignell</i> . . . . .	49
4.2 Circular vs. Linear Colliders <i>written by Lewis Simmons</i> . . . . .	49
4.3 The Collider Layout <i>written by Lucy Bignell</i> . . . . .	51
4.4 Energy Losses <i>written by Matthew Heath</i> . . . . .	52
4.4.1 Acceleration Radiation Losses . . . . .	52

4.4.2	Linearly Accelerated Particles . . . . .	52
4.4.3	Circularly Accelerated Particles . . . . .	53
4.5	Beam-Beam Interactions <i>written by Thomas Dack</i> . . . . .	54
4.6	Guinea Pig Simulations <i>written by Thomas Dack</i> . . . . .	54
4.6.1	GuineaPig Output . . . . .	54
4.6.2	Beam Energy Output . . . . .	55
4.6.3	Pair Data Output . . . . .	55
4.7	Beam Dimensions and Bunch Structure <i>written by Thomas Lane</i> . . . . .	57
4.8	Particle Production <i>written by Christopher Francis</i> . . . . .	58
4.9	Damping Rings and Boosters . . . . .	60
4.9.1	Particle Injector <i>written by Aaron Byrne</i> . . . . .	60
4.9.2	Damping Rings <i>written by Aaron Byrne</i> . . . . .	60
4.9.3	Storage Rings <i>written by Aaron Byrne</i> . . . . .	63
4.9.4	Pre Linac Booster <i>written by Aaron Byrne</i> . . . . .	63
4.9.5	Energy Losses at the Bends <i>written by Matthew Heath</i> . . . . .	64
4.9.6	Bunch Compressors <i>written by Aaron Byrne</i> . . . . .	64
4.10	Main Linac <i>written by Thomas Lane</i> . . . . .	64
4.10.1	Focusing . . . . .	65
4.10.2	Main Linac Design . . . . .	67
4.10.3	Measuring the energy of the collider particle beams <i>written by Lewis Simmons</i> . . . . .	68
4.11	Collimation <i>written by Lucy Bignell</i> . . . . .	68
4.12	Machine-Detector Interface <i>written by Raveena Deol</i> . . . . .	69
4.13	Final Focusing . . . . .	70
4.14	Stabilising the beam . . . . .	71
4.15	Beam Dump <i>written by Lewis Simmons</i> . . . . .	71
4.16	Location of the Collider <i>written by Aaron Byrne</i> . . . . .	73
<b>5</b>	<b>The Detector Design</b> . . . . .	<b>74</b>
5.1	Introduction <i>written by Adrian Cross</i> . . . . .	74
5.2	The Detector Layout <i>written by Adrian Cross</i> . . . . .	74
5.3	Coordinate System <i>written by Andrew Clarke</i> . . . . .	75
5.4	Solenoid <i>written by Adrian Cross and Dwayne Spiteri</i> . . . . .	75
5.4.1	CMS . . . . .	76
5.4.2	ATLAS . . . . .	76
5.4.3	Setup . . . . .	76
5.5	Forward Calorimetry <i>written by Adrian Cross and Dwayne Spiteri</i> . . . . .	77
5.5.1	Luminosity Calorimeters - LumiCal . . . . .	77
5.5.2	Beam Calorimeters - BeamCal <i>written by Dwayne Spiteri</i> . . . . .	79
5.6	Trackers <i>written by Ryan Jones</i> . . . . .	79
5.6.1	Tracking Detector . . . . .	79
5.6.2	Vertex Detector . . . . .	80
5.6.3	Parameters . . . . .	80
5.7	ECAL <i>written by Andrew Clarke and John Cotterill</i> . . . . .	82
5.7.1	ECAL Requirements <i>written by John Cotterill</i> . . . . .	82
5.7.2	Homogenous vs Sampling <i>written by John Cotterill</i> . . . . .	83
5.7.3	ECAL Selection <i>written by John Cotterill</i> . . . . .	83
5.7.4	Resolution and Efficiency <i>written by Andrew Clarke</i> . . . . .	84
5.7.5	Parameters . . . . .	84
5.8	HCAL <i>written by Daniel Hatton</i> . . . . .	86
5.8.1	Hadronic Showers . . . . .	86
5.8.2	Particle Flow Algorithm Calorimetry . . . . .	87
5.8.3	Materials . . . . .	87
5.8.4	Resolution . . . . .	88
5.8.5	Parameters . . . . .	88
5.9	Muon System <i>written by Russell Turner</i> . . . . .	89
5.9.1	Design . . . . .	89
5.9.2	Parameters . . . . .	90

5.10 Time Resolution <i>written by Adrian Cross</i>	90
5.11 Detector Card <i>written by Andrew Clarke and Adrian Cross</i>	91
<b>6 The Five Year Plan</b>	<b>92</b>
<b>7 Conclusion by Dwayne Spiteri, Lucy Bignell, Andrew Clarke, Adrian Cross and Chris Francis</b>	<b>94</b>
<b>References</b>	<b>95</b>
<b>A MSSM and NMSSM slha file outputs for the benchmarks used throughout the report</b>	<b>102</b>
<b>B Total Ionisation Energy Loss (IEL) in the collider</b>	<b>107</b>
<b>C GuineaPig Data Plots</b>	<b>108</b>
C.1 300 GeV Centre of Mass Energy plots	108
C.2 1 TeV Centre of Mass Energy plots	109
C.3 6 TeV Centre of Mass Energy plots	110
C.4 Refined 6 TeV Centre of Mass Energy plots	111

## List of Figures

2.1 Fit of Higgs couplings for particles with coupling dependent on their own mass [4].	11
2.2 Diagram of possible situations and interactions that can occur with an example of a top quark as a result of the Higgs mechanism [6].	12
2.3 The Higgs-Strahlung process with the Z boson decaying via different processes.[23]	12
2.4 The Feynman diagram for the W fusion process.[23]	13
2.5 The Feynman diagram for the Z fusion process.[23]	13
2.6 The Feynman diagram for the radiation off of tops process.[24]	13
2.7 The Feynman diagram for the double Higgs-Strahlung process.[25]	14
2.8 The Feynman diagram for the double W fusion process.[25]	14
2.9 The cross sections for different production processes. $H\nu_e\bar{\nu}_e$ is the W fusion process.	14
2.10 The Higgs decay branching ratios for varying Higgs masses.[14]	16
2.11 Feynman diagram depicting Higgs coupling to fermions, with the proportionality of such coupling displayed.	17
2.12 Feynman diagrams of the 2 basic mechanisms for Higgs to photon decay [11]	17
2.13 Histogram of the invariant mass of photon pairs. The peak seen can be attributed to the Higgs particle	18
2.14 Feynman diagrams showing the production of two Higgs particles via Higgs-Strahlung [27].	20
2.15 Feynman diagrams showing the production of two Higgs particles from the WW fusion process [27]	20
2.16 Graph to show how the cross section for Higgs pair production varies with the centre of mass energy via the processes double Higgs-Strahlung and double WW-fusion [28].	20
2.17 The mass of the Higgs reconstructed using jets at energies of a)300 GeV and b) 1TeV.	21
2.18 The Higgs mass peaks fitted at a)300GeV and b)1TeV.	22
2.19 The Higgs mass peaks fitted at a)300GeV and b)1TeV.	22
2.20 The mass of the Higgs found indirectly.	23
2.21 The indirect mass of the Higgs boson fitted with a Gaussian.	23
2.22 A simulation of the pinch effect for two colliding beams[32].	25
3.1 The conflicting production mechanisms for $Z'$ boson production in lepton and hadron collisions. The Drell-Yan process (right) used in hadronic collisions has a greater background as a result of the non-interacting hadron fragments.	30
3.2 Feynman diagrams of the potential decay modes of the $Z'$ boson.	31
3.3 Cross section for di-muon production with varying centre-of-mass energy given $M(Z')=3\text{TeV}$ . Values have been calculated using the Whizard [36] program.	31
3.4 Expanded Beamstrahlung tail for $M(Z')=3\text{TeV}$ . The dashed line represents the point that the SM and the additional $Z'$ interference cross sections are equal.	32
3.5 $Z'$ effects on di-muon cross section at a 6TeV centre-of-mass energy with varying $Z'$ mass.	33
3.6 Diagram to illustrate the particle content of Supersymmetry <i>designed by Dwayne Spiteri</i>	35

3.7	example SLHA input file . . . . .	37
3.8	Predicted mass of the higgs particle with R-parity conservation, $m_0 = 300\text{GeV}$ , $m_{1/2} = 2000\text{GeV}$ , $A_0 = -2000\text{GeV}$ and varying $\tan\beta$ .[70] [71]	37
3.9	Predicted mass of the higgs particle with R-parity conservation, $m_0 = 300\text{GeV}$ , $m_{1/2} = 2000\text{GeV}$ , $\tan\beta = 20$ and varying $A_0$ [70] [71]	37
3.10	Plot of event number against missing $E_T$ with higher energy jets of momentum $< 225\text{ GeV}$ using the NMSSM01 benchmark with $\sqrt{s} = 1\text{ TeV}$ and integrated luminosity $100\text{ fb}^{-1}$ . The result for $e^+e^- \rightarrow W^+W^-$ and $e^+e^- \rightarrow \nu_e\bar{\nu}_e W^+W^-$ background (black) is shown with the result for the background and $e^+e^- \rightarrow \chi_1^+\chi_1^-$ (blue).	40
3.11	Data of number of events with missing $E_T$ against the energy of that missing $E_T$ and a 400GeV electron momentum cut-off for 501GeV selectron benchmark.	42
3.12	Data of number of events with missing $E_T$ against the energy of that missing $E_T$ and a 400GeV electron momentum cut-off for 1TeV selectron benchmark.	43
3.13	Data of number of events with missing $E_T$ against the energy of that missing $E_T$ and a 400GeV electron momentum cut-off for 1.47TeV selectron benchmark.	43
3.14	In a lepton collider neutralinos are produced which can subsequently decay into the lightest pseudoscalar Higgs and another neutralino of lower mass.	44
3.15	Feynman diagrams for the pseudoscalar Higgs decay to jets (a) and the corresponding standard model background processes. The background events are direct electron-positron annihilation to quark-antiquark pair (b), $Z$ boson production (c) and charged $W$ boson production (d).	45
3.16	Fitted peaks of the number of jet events versus invariant mass of jet events in the detector (left). Showing only background contributions (right). Data acquired using the NMSSM02 benchmark with a centre of mass energy of 3TeV and an integrated luminosity of $100\text{fb}^{-1}$ .	45
3.17	Showing the background contributions (red) overlaid on top of the total jet events (black) from Figure 3.16.	46
3.18	Feynman diagram describing stop squark decay	47
3.19	Results of a Delphes smearing simulation of Stop squark decay at 3TeV	48
4.1	A schematic of LEPIC <i>designed by Lewis Simmons</i>	51
4.2	Histograms and CDFs produced from GuineaPig outputs for a centre of mass for 3 TeV	56
4.3	Plot showing the Magnetic field required to keep electrons with $\cos(\theta)$ inside a vertex detector with radius of 0.014m. The blue line shows the proposed magnetic field of 5T.	57
4.4	Plot showing the inner vertex radius required to encapsulate electrons with $\cos(\theta)$ experiencing a B field of 5T. The blue line shows the proposed inner radius of 0.014m.	58
4.5	Diagram illustrating electron oscillations in helical undulators [133]	59
4.6	CAD example of pair production target on a rotating axis [134]	60
4.7	The layout of the wiggler magnets and the RF cavities inserted to compensate for the energy loss due to the wigglers. ( <i>Not to Scale</i> )	62
4.8	The setup of the bunch compressor. The purple line represents the path followed by the high energy particles at the back of the bunch the red is the lower energy particles at the front of the bunch. The green line represents the path the average energy particles would follow [101].	64
4.9	The basic components of an RF cavity[117].	65
4.10	An example of a basic focusing lens [120].	66
4.11	A quadrupole magnet [120].	66
4.12	An example of a FODO lattice [120].	67
4.13	The layout of the FODO lattice that we shall be using for our collider, where the red boxes are the 9 cell cryomodules and the yellow boxes are the 8 cell cryomodules.	67
4.14	A schematic of a 4 magnet chicane with ILC like dimensions [114]	68
4.15	The smaller aperture spoilers cause angular beam divergence such that damage is not caused to the absorbers upon impact [89]	69
4.16	Tapering of the spoilers reduces the risk transverse wakefields.	70
4.17	Schematic of an adjustable-strength PMQ divided in to five rotatable rings [129].	70
4.18	Schematic of the intra-train feedback system at the interaction point [128].	71
4.19	Schematic of the two stripline kickers, three BPMs and the ATF quadrupole magnets. [129].	72
4.20	A simple schematic of the main beam dump.	73
5.1	Cross section of LEPIC detector with each component labelled	74
5.2	Scale diagram of detector components with radii at the component borders	75

5.3	Interaction of particle types with different detector components . . . . .	75
5.4	The coordinate system used within the detector. $p$ is the momentum of the particle . . . . .	76
5.5	The left and centre Feynmann diagrams are for Bhabha scattering and the one on the right shows a process that competes with this. . . . .	77
5.6	Particle shower in a luminosity calorimeter . . . . .	78
5.7	Process of ionisation and track detection [148] . . . . .	80
5.8	An outline of a typical vertex detector [152] . . . . .	81
5.9	Schematic diagram of a sampling ECAL. White and grey regions represent the absorber and active medium respectively. Solid lines represent electrons and dashed lines represent photons produced through bremsstrahlung <i>designed by John Cotterill.</i> . . . . .	82
5.10	Plot of constituent particle energies in jets from 1000 $W^+W^-$ and $ZZ$ events at $\sqrt{s} = 1, 3$ and $6\text{TeV}$ . . . . .	87
5.11	Schematic Diagram of one detector layer . . . . .	89
5.12	Basic design of (a) the barrel and (b) the endcap muon system (not to scale) . . . . .	90
C.1	The distribution of macro-particle energy after beam-beam interactions for a 300 GeV centre of mass. . . . .	108
C.2	The distribution of macro-particle energy within Beam 1, after beam-beam interactions, for a 300 GeV centre of mass. . . . .	108
C.3	The distribution of macro-particle energy within Beam 2, after beam-beam interactions, for a 300 GeV centre of mass. . . . .	109
C.4	The cumulative frequency distribution of macro-particle energy within Beam 1, after beam-beam interactions, for a 300 GeV centre of mass. . . . .	109
C.5	The cumulative frequency distribution of macro-particle energy within Beam 2, after beam-beam interactions, for a 300 GeV centre of mass. . . . .	110
C.6	The distribution of macro-particle energy after beam-beam interactions for a 1 TeV centre of mass. . . . .	110
C.7	The distribution of macro-particle energy within Beam 1, after beam-beam interactions, for a 1 TeV centre of mass. . . . .	111
C.8	The distribution of macro-particle energy within Beam 2, after beam-beam interactions, for a 1 TeV centre of mass. . . . .	111
C.9	The cumulative frequency distribution of macro-particle energy within Beam 1, after beam-beam interactions, for a 1 TeV centre of mass. . . . .	112
C.10	The cumulative frequency distribution of macro-particle energy within Beam 2, after beam-beam interactions, for a 1 TeV centre of mass. . . . .	112
C.11	The distribution of macro-particle energy after beam-beam interactions for a 6 TeV centre of mass. . . . .	113
C.12	The distribution of macro-particle energy within Beam 1, after beam-beam interactions, for a 6 TeV centre of mass. . . . .	113
C.13	The distribution of macro-particle energy within Beam 2, after beam-beam interactions, for a 6 TeV centre of mass. . . . .	114
C.14	The cumulative frequency distribution of macro-particle energy within Beam 1, after beam-beam interactions, for a 6 TeV centre of mass. . . . .	114
C.15	The cumulative frequency distribution of macro-particle energy within Beam 2, after beam-beam interactions, for a 6 TeV centre of mass. . . . .	115
C.16	A 100 bin histogram of the distribution of macro-particle energy within Beam 1, after beam-beam interactions, for a 6 TeV centre of mass. . . . .	115
C.17	A 100 bin histogram of the distribution of macro-particle energy within Beam 2, after beam-beam interactions, for a 6 TeV centre of mass. . . . .	116

## List of Tables

2.1	A table of some properties of the fundamental fermions of the Standard Model . . . . .	8
2.2	A table of some of the properties of the gauge bosons that mediate interactions in the Standard Model . . . . .	8
2.3	Decay Modes and their corresponding branching ratios for a Standard Model Higgs boson [16]. . . . .	16
2.4	The Higgs decay modes and our desired precision measurements of their branching fractions. . . . .	25
3.1	The current (2015) limits on $Z'$ boson mass from LHC experiments [64] [65] . . . . .	30
3.2	$Z'$ mass limit analysis for the LEPIC collider investigations at 6TeV . . . . .	34
3.3	Constrained MSSM parameters [69] . . . . .	36
3.4	NMSSMTools grid scan parameters . . . . .	38
4.1	A variety of circular colliders with their beam energy, radii and corresponding energy losses per turn . . . . .	51
4.2	Table Showing the percentage of particles remaining at the original beam energy after beamstrahlung effects . . . . .	55
4.3	The beam structure that we shall be using for our collider. . . . .	58
4.4	The Higgs decay modes and the predicted precision of our measurements of their branching fractions. . . . .	58
4.5	Characteristics of some superconducting materials[118]. . . . .	65
4.6	The number of RF units required to be turned on for the chosen centre of mass energy collisions and how much power these RF units will use. . . . .	67
4.7	Expected beam dump paramaters for this collider system. . . . .	72
5.1	Typical energy resolutions for an electromagnetic calorimeter. All energies are in GeV. [22] . . . . .	85
5.2	Rate of Higgs producing mechanisms at 1TeV with an instantaneous luminosity of $1.98 \times 10^{-4} fb^{-1}s^{-1}$ . . . . .	91
6.1	The general outline of our five year plan. . . . .	92

# **1 Project Brief written by Russell Turner and Dwayne Spiteri**

The discovery of a new scalar boson by the LHC experiments at CERN represents a step towards a complete Standard Model of Particle Physics. Assuming the new particle is a Standard Model Higgs particle, the measurement of its mass allows us to predict the way that the particle couples to the other particles in the model. However, due to the hadronic nature of the LHC, some of these predictions are difficult to confirm. This is where the use of an electron positron collider becomes necessary. Since the electron and positron are both elementary particles, and they annihilate, an electron positron collider produces much less background than a hadron collider, allowing us to measure the decays of a Higgs particle much more easily. This collider could then operate at a larger energy scale in order to look for “new” Physics phenomena such as SuperSymmetry and exotic heavy neutral gauge bosons. With this in mind, we have designed a Particle Physics experiment, to be undertaken over five years after the construction of an electron positron collider. The initial brief for this design project was to:

- Investigate the potential of an  $e^+e^-$  collider to measure Higgs properties in order to confirm theoretical predictions for a Standard Model Higgs Boson
- Investigate the potential of an  $e^+e^-$  collider to search for evidence for new exotic particles.
- Evaluate the effectiveness of different collider designs to reveal new physics phenomena at high energies.
- Analyse the detectors used with these colliders to detect the new physics phenomena at high energies.

The aim of this report is to summarise the progress that LEPIC has made in regards to fulfilling the initial brief of this project. This shall be done by addressing each of these bullet points in turn within their own section and coming up with a five year runtime plan of the collider.

## 2 The Standard Model Higgs Boson

### 2.1 Introduction *written by Matthew Heath*

The current version of the Standard Model for particle physics describes the interactions between three generations of fermions and their antiparticles with three of the four fundamental forces of electromagnetism, the strong nuclear force, and the weak nuclear force while the gravitational interaction currently has no known role. Table 2.1, shows the fundamental fermions of the Standard Model along with some of their properties where all the particles have a spin of  $\frac{1}{2}$ .

Table 2.1: A table of some properties of the fundamental fermions of the Standard Model

Generation	Fermion	Symbol	Baryon Number	Charge (e)	Mass (GeV)
I	Up Quark	u	$\frac{1}{3}$	$+\frac{2}{3}$	0.0023
	Down Quark	d	$-\frac{1}{3}$	$-\frac{1}{3}$	0.0048
	Electron	e	0	-1	0.000511
	Electron Neutrino	$\nu_e$	0	0	negligible
II	Charm Quark	c	$\frac{1}{3}$	$+\frac{2}{3}$	1.275
	Strange Quark	s	$-\frac{1}{3}$	$-\frac{1}{3}$	0.095
	Muon	$\mu$	0	-1	0.105658
	Muon Neutrino	$\nu_\mu$	0	0	negligible
III	Top Quark	t	$\frac{1}{3}$	$+\frac{2}{3}$	173.5
	Bottom Quark	b	$-\frac{1}{3}$	$-\frac{1}{3}$	4.65
	Tau	$\tau$	0	-1	1.77682
	Tau Neutrino	$\nu_\tau$	0	0	negligible

The antiparticles of the fermions in Table 2.1 have opposite charge and baryon number, while all the other quantities described in the table are identical. The three fundamental forces involved in the interactions of the Standard Model are mediated by the gauge bosons that are shown in Table 2.2. All of these particles bar the photon are self-interacting and they all have a spin of 1.

Table 2.2: A table of some of the properties of the gauge bosons that mediate interactions in the Standard Model

Force	Gauge Boson	Symbol	Charge (e)	Mass (GeV)
Strong	Gluon	$g$	0	0
Electromagnetic	Photon	$\gamma$	0	0
Weak	W Boson	$W^\pm$	$\pm 1$	80.385
	Z Boson	$Z^0$	0	91.1876

The Standard Model is a gauge theory with the group  $U(1) \times SU(2) \times SU(3)$  in which the right-handed components of the fermion wavefunctions, described by the U(1) part of the gauge group, interact differently to the left-handed components described by the SU(2) part. For nonzero mass quarks or leptons, the left and right-handed components can be transformed into each other using a Lorentz transform. For example, the mass term of an electron in relation to its left and right-handed components is

$$m_e \psi_e^* \psi_e = m_e (\psi_{eL}^* + \psi_{eR}^*)(\psi_{eL} + \psi_{eR}) = m_e \psi_{eL}^* \psi_{eR} + m_e \psi_{eR}^* \psi_{eL} \quad (2.1)$$

This shows that the left and right-handed components need to be coupled in order to produce a mass term, however this is not allowed as they transform differently under a gauge transform. A mechanism was required to give the fundamental particles mass.

In 1964, three independent papers ('Broken Symmetry and the Mass of Gauge Vector Mesons' written by Englert and Brout, 'Broken Symmetries and the Masses of Gauge Bosons' written by Higgs, and 'Global Conservation Laws and Massless Particles' written by Guralnik, Hagen, and Kibble) all developed an explanation of how mass would come about in gauge theories, this subsequently became known as the Higgs mechanism. The principle of the

mechanism introduced a field with a non-zero vacuum expectation value to the Standard Model that would induce a spontaneous symmetry breaking to produce inherent massive bosonic particles, with a spin of 0 and positive parity [2], that interact with other fields in the gauge theory to produce mass terms. The field is known as the Higgs field, and the particles as Higgs bosons. Though, in order to prove the validity of this theory, the Higgs boson must be observed and measured in experiment, but over the years it has proved quite elusive due to it having a mass that is theoretically impossible to predict, requiring a search over a large mass range.

However, in 2012, the ATLAS Collaboration and the CMS Collaboration at CERN announced the discovery of a new particle with properties that are so far consistent with the Higgs boson using the Large Hadron Collider. ATLAS has published a mass for this particle as  $125.36 \pm 0.37(stat) \pm 0.18(sys)GeV$  and CMS published the mass as  $125.03^{+0.26}_{-0.27}(stat)^{+0.13}_{-0.15}(sys)GeV$ . The combined efforts of these two experiments found a refined value of  $125.09 \pm 0.21(stat) \pm 0.11(sys)GeV$  [20]. A large part of the operation of our collaboration's collider will be focused on further investigating this particle in order to verify it as a Standard Model Higgs boson and to refine measurements of currently recorded properties.

## 2.2 The Higgs Field

### 2.2.1 Justification written by Russell Turner

The Higgs field arises as a consequence of trying to consolidate quantum field theory with the weak interaction (WI). In quantum field theory, every particle exists as an excitation of a field, which obeys an equation of the form

$$\frac{\partial^2 Z}{\partial t^2} - c^2 \frac{\partial^2 Z}{\partial x^2} = - \left( \frac{2\pi c^2}{h} \right)^2 m^2 Z(x, t) \quad (2.2)$$

where  $m$  is the mass of the particle and  $Z$  is the field. A simple example of this would be the electric field, which obeys the wave equation

$$\frac{\partial^2 E}{\partial x^2} = \frac{1}{c^2} \frac{\partial^2 E}{\partial t^2} \quad (2.3)$$

which is consistent with equation 2.2 for a particle with mass 0, which would of course be the photon. However, equation 2.2 does not take into account the effect of the weak interaction on a particle, which requires some modifications.

These modifications can be illustrated by looking at the electron field, since the weak interaction has a known effect on electrons ( $e^- \rightarrow W^- \nu_e$  or equivalent). Since the electron is spin- $\frac{1}{2}$ , the field can be split into two coupled fields:

$$\frac{\partial \psi}{\partial t} - c \frac{\partial \psi}{\partial x} = + \frac{2\pi m c^2}{h} \chi \quad (2.4)$$

$$\frac{\partial \chi}{\partial t} + c \frac{\partial \chi}{\partial x} = - \frac{2\pi m c^2}{h} \psi \quad (2.5)$$

It is implied that the amplitudes of these fields are proportional to each other. It is in these equations that the problems with including the weak interaction arise: it is known from experiment that the WI affects the  $\chi$  field, but not the  $\psi$  field. In order to account for this, a new field must be included, the Higgs field.

The Higgs field is made up of a doublet of two complex fields [22]:

$$H = \begin{pmatrix} \phi^+ \\ \phi^0 - ia^0 \end{pmatrix} \quad (2.6)$$

Including this new field in the field equations along with the fields for the weak interaction gives us three new equations

$$\frac{\partial\psi}{\partial t} - \frac{\partial\psi}{\partial x} = +\frac{2\pi c^2}{h}y(H^{0*}\chi + H^-\nu) \quad (2.7)$$

$$\frac{\partial\chi}{\partial t} + \frac{\partial\chi}{\partial x} + gW^-\nu = -\frac{2\pi c^2}{h}yH^0\psi \quad (2.8)$$

$$\frac{\partial\nu}{\partial t} + \frac{\partial\nu}{\partial x} + gW^+\chi = -\frac{2\pi c^2}{h}yH^+\psi \quad (2.9)$$

which implicitly obey all the symmetries of the weak interaction. In these equations, g represents the coupling of the weak interaction,  $H^+ = \phi^+$ ,  $H^0 = \phi^0 - ia^0$ ,  $H^- = H^{+*}$ ,  $\nu$  is the neutrino equivalent of  $\chi$  and  $y$  is the Yukawa coupling parameter. However, at the low energy scales, part of this symmetry is broken. This can be accounted for by saying that the Higgs field has a non-zero vacuum expectation value  $v$ , and for small disturbances it takes the form

$$H = \begin{pmatrix} 0 \\ v + h(x, t) \end{pmatrix} \quad (2.10)$$

and from this the equations 2.7, 2.8 and 2.9, are changed to

$$\frac{\partial\psi}{\partial t} - \frac{\partial\psi}{\partial x} = +\frac{2\pi c^2}{h}y(v + h(x, t))\chi \quad (2.11)$$

$$\frac{\partial\chi}{\partial t} + \frac{\partial\chi}{\partial x} + gW^-\nu = -\frac{2\pi c^2}{h}y(v + h(x, t))\psi \quad (2.12)$$

$$\frac{\partial\nu}{\partial t} + \frac{\partial\nu}{\partial x} + gW^+\chi = 0 \quad (2.13)$$

The value of  $v$  can be measured experimentally and has a value of  $246\text{GeV}$  [10]. This appears to break the symmetry, but it is really just hidden in the value of  $H$ . This also shows some of the required properties of the 2 fields involved, namely the coupling of the Higgs field to mass (via  $y$ ), the fact that the W field converts between  $\chi$  and  $\nu$  and the reconstruction of the original field equations for  $W = h = 0$  [8].

Another important motivation for the Higgs field is that it provides a mechanism for giving mass to particles. Consider a field  $Z$  which behaves in the same way as the EM field. Without interacting with the Higgs field, this field's associated particle would have no mass. But if you then consider the fields' interaction with each other

$$\frac{\partial^2 Z}{\partial t^2} - c^2 \frac{\partial^2 Z}{\partial x^2} = -\left(\frac{2\pi c^2}{h}\right)^2 y^2 H^2 Z \quad (2.14)$$

$$= -\left(\frac{2\pi c^2}{h}\right)^2 y^2 (v + h(x, t))^2 Z \quad (2.15)$$

and remove all the terms with factors of  $h(x, t)Z$  (or higher order) due to the assumed small size of  $h$ , the resulting equation is equivalent to equation 2.2

$$\frac{\partial^2 Z}{\partial t^2} - c^2 \frac{\partial^2 Z}{\partial x^2} = -\left(\frac{2\pi c^2}{h}\right)^2 y^2 v^2 Z \quad (2.16)$$

$$m_Z = yv \quad (2.17)$$

and so it can be seen that interacting with the non-zero Higgs field gives the particle mass.[9]

### 2.2.2 Implications on Measurable Quantities *written by Ryan Jones*

The Higgs field is important to consider as it provides a theoretical background for the Higgs coupling, and provides constraints for almost all of the various types of couplings, which are to be discussed later [Section 2.5]. Before the discovery of a Higgs-like particle at the LHC [3], this theoretical Higgs field was particularly important as the

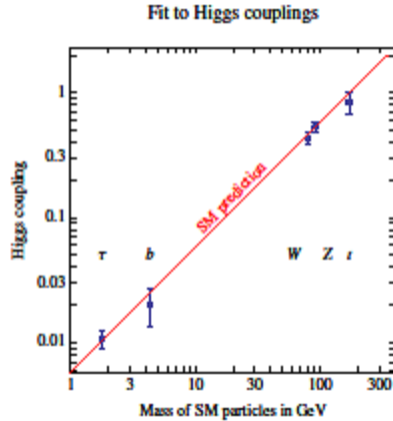


Figure 2.1: Fit of Higgs couplings for particles with coupling dependent on their own mass [4].

Standard Model does not predict a mass for the Higgs particle, therefore derivation of coupling constants had to be undertaken using this particular theory, where some of these significant values can be seen in Figure 2.1.

The Higgs field relates to coupling constants through the non-zero vacuum expectation value,  $v$ , which has a value of  $246\text{GeV}$ . This is defined as a function of the Fermi constant,  $G_F$ , which has an experimentally obtained value of  $1.166371(6) \times 10^{-5}\text{GeV}^{-2}$  [5], using the following relation:

$$v = (\sqrt{2}G_F)^{-\frac{1}{2}} \quad (2.18)$$

with such an equation coming into existence due to the relation between  $v$  and the mass of the W boson, which governs the Fermi interaction that  $G_F$  is obtained from. Each different type of particle interacts with the Higgs field in a slightly different way, resulting in a variety of equations that describe the relation between Higgs coupling and the mass of that particular particle, which will be explored later.

It has already been briefly mentioned how particles acquire mass due to the Higgs field; this will be covered in more detail. One way of looking at this is to consider the implications of a Higgs field with a vacuum expectation value of zero. Immediately, it can be seen that this would result in no particles of mass, however there would be additional implications, the most important being that each matter particle, with the exception of neutrinos, would instead be two particles; a left and a right counterpart, that interact strongly with each other and the Higgs particle. An interaction with a Higgs particle changes the alignment of one of these particles to its counterpart.

With a non-zero vacuum expectation value, these particles undergo mixing as a result of the aforementioned alignment changing, resulting in the single particle that we observe. An example can be seen in Figure 2.2. This mixing is very much particle dependant; referring back to a Higgs field of zero, the only difference between particles with zero mass would be their interactions with the Higgs particle, as certain particles interact more with the Higgs boson, as can be seen by the differences in coupling constants. Using the top quark example from Figure 2.2, this particular fermion interacts with the Higgs field in the order of  $10^{27}$  times per second. Such a large amount of interactions with a non-zero Higgs field results in a higher mass.

### 2.3 Higgs Production *written by Andrew Clarke*

There are four main processes that will occur inside an electron positron collider that will produce Higgs particles. The four process and how the cross section of the process vary with the centre of mass energy of the collision will be discussed.

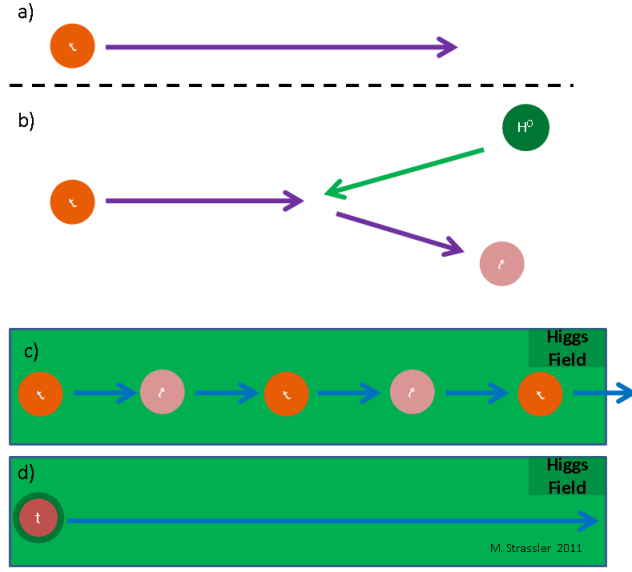


Figure 2.2: Diagram of possible situations and interactions that can occur with an example of a top quark as a result of the Higgs mechanism [6].

### 2.3.1 Higgs-Strahlung

The Higgs-Strahlung process will occur when the electron and positron collide and produce a virtual Z boson. The virtual Z boson can then decay into a Higgs boson and a real Z boson. The Z boson will then decay into a quark and anti-quark pair, a neutrino and anti-neutrino pair or a charged lepton and corresponding anti-lepton. The Feynman diagrams for this process can be seen in Figure 2.3. The Higgs-Strahlung process is a very good interaction to look

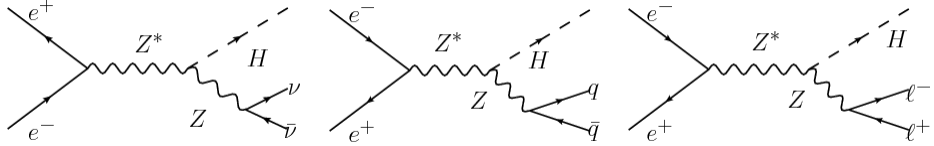


Figure 2.3: The Higgs-Strahlung process with the Z boson decaying via different processes.[23]

at as it produces a Higgs boson and a Z boson. The Z boson decays can be easily identified and measured. The Z boson will decay into neutrinos ( $20.00 \pm 0.06\%$ ) of the time.[22] If the Z produces two neutrinos then only the Higgs decay products will be viewed inside the detector. However, if the Z decays into a lepton anti-lepton pair (the branching fraction is  $(10.0974 \pm 0.0069)\%$ ) or a quark anti-quark pair (branching fraction of  $(69.91 \pm 0.06)\%$ ) then the energy and the momentum of the Z can be calculated.[22] Once the energy and momentum of the Z boson has been determined the mass of the Higgs can be calculated. Both energy and momentum must be conserved in any interaction and we can therefore infer information about the Higgs boson without directly measuring it. Using relativistic kinematic and the information provided from the Z boson an equation can be written that will determine the mass of the Higgs boson (equation 2.19). The mass of the Higgs can also be found directly by reconstructing the invariant mass of the decay products.

$$M_H = \sqrt{(\sqrt{s} - E_Z)^2 + (\underline{0} - \underline{P}_Z)^2} \quad (2.19)$$

Equation 2.19: The mass of the Higgs can be determined from the centre of mass energy  $\sqrt{s}$  and the energy of the Z boson. The two beams have the same energy and momentum so the net momentum is  $\underline{0}$ .

### 2.3.2 W and Z fusion

The W fusion event occurs when the electron and positron each emit virtual W bosons. The electron will turn into an electron neutrino and the positron into an anti-electron neutrino so that the lepton number will be conserved

when emitting the virtual W. The virtual W bosons will then interact and produce a Higgs boson. This method of production can be used for producing the Higgs particle, however, it is not possible to look at the Higgs boson indirectly as the neutrinos will pass straight through the detector. Figure 2.4 shows the Feynman diagram for the W fusion interaction. The Z fusion process works in a similar way to the W fusion process, but instead of the

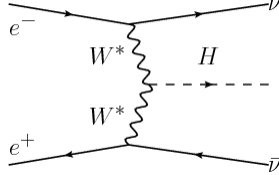


Figure 2.4: The Feynman diagram for the W fusion process.[23]

electron and positron each emitting a virtual W boson, virtual Z bosons are emitted. The electron and positron remain as an electron and a positron but have less energy. The virtual Z bosons can then interact and produce a Higgs boson. This process can be studied more easily than the W fusion process as the electron and positron in the final state can be measured as well as the Higgs boson. The Feynman diagram for this process can be seen in Figure 2.5.

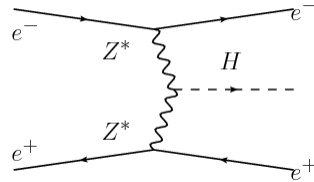


Figure 2.5: The Feynman diagram for the Z fusion process.[23]

### 2.3.3 Radiation Off of Tops

The radiation off of top quarks can occur when the electron and positron interact and produce a photon or a Z boson. The photon can then undergo pair production and produce a top and an anti-top quark. A Higgs boson can then be radiated off of the top quark. The process can work with a Z boson replacing the photon. However, if there is a Z boson, a Higgs boson can be emitted from the Z boson which remains as a Z boson. The Z boson can then produce a top and an anti-quark pair. The two processes can be seen in Figure 2.6. The process can be measured easily as there will be a Higgs boson and two jets produced by the top quarks.

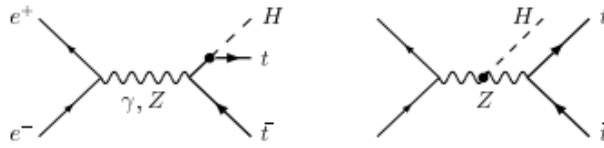


Figure 2.6: The Feynman diagram for the radiation off of tops process.[24]

### 2.3.4 Double Higgs Production

If the electron and positron have a sufficiently high enough energy then two Higgs bosons can be produced. There are two main process by which two Higgs bosons can be created via an electron positron collision. The first is the double Higgs-Strahlung process which produces a Higgs boson in the same way as described for the single Higgs-Strahlung process. However, the Higgs boson produced is able to radiate a second Higgs boson. The Feynman diagram for this process can be seen in Figure 2.7. There are variations of this process where the second Higgs

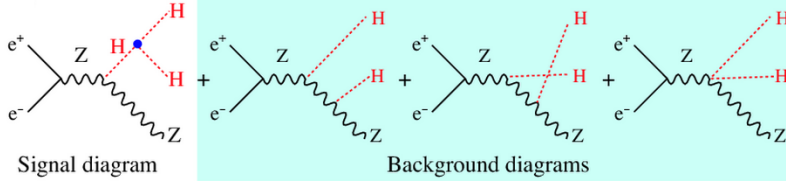


Figure 2.7: The Feynman diagram for the double Higgs-Strahlung process.[25]

boson is emitted by the Z boson as shown in Figure 2.7. The second process via which two Higgs bosons can be produced is double W fusion. The process is the same as single Higgs production but either the Higgs radiates a second Higgs boson or one of the W bosons emits a Higgs boson before interacting with the other W boson and producing a Higgs boson. The processes can be seen in Figure 2.8.

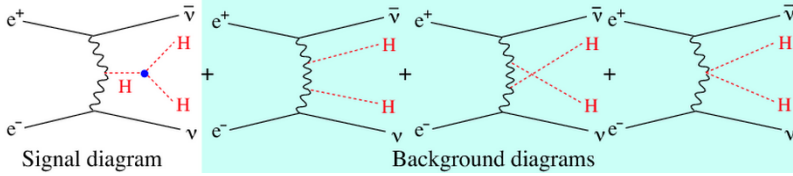


Figure 2.8: The Feynman diagram for the double W fusion process.[25]

### 2.3.5 Cross-sections of the Production Processes

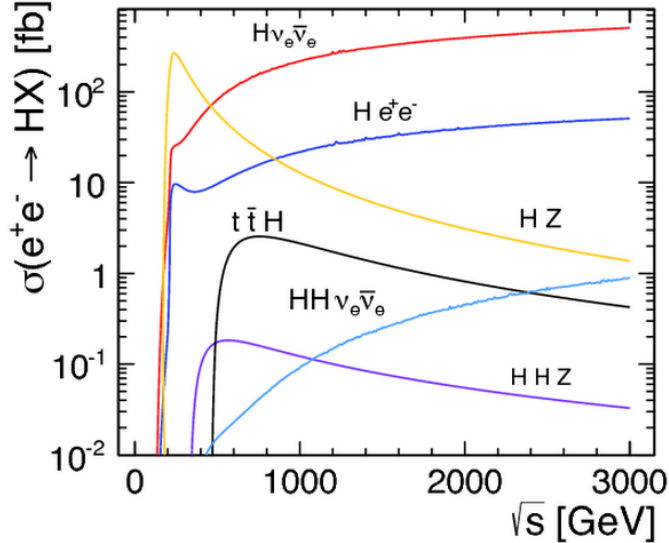


Figure 2.9: The cross sections for different production processes.  $H\nu_e\bar{\nu}_e$  is the W fusion process.  $He^+e^-$  is the Z fusion process.  $HZ$  is the Higgs-Strahlung processes.  $t\bar{t}H$  is the radiation off of tops process.  $HH\nu_e\bar{\nu}_e$  is the double Higgs production via W fusion.  $HHZ$  is the double Higgs boson production via the Higgs-Strahlung process.[26]

Figure 2.9 shows how the cross-section of the processes which produce the Higgs boson varies with centre of mass energy. There is a threshold energy for the W fusion, Z fusion and Higgs-Strahlung processes at a centre of mass energy just below 200GeV. The production of the Higgs boson from radiation off of tops does not begin until a centre of mass energy of 440GeV. This is due to the large mass of the top quarks that need to be produced for this process. Similarly the double Higgs production cannot happen with a centre of mass energy less than 380GeV for double Higgs-Strahlung and less than 400GeV for double W fusion. The cross-sections also vary with energy. The Higgs-Strahlung process is dominant at lower centre of mass energies and then decreases as the centre of mass

energy increases. The cross-section for the W fusion and Z fusion processes increases as the centre of mass energy increases. The cross-section for W fusion is larger than that of Z fusion at all centre of mass energies. At high centre of mass energies there is a factor of ten difference between the two processes. The radiation off of tops process sharply increases as the centre of mass energy increases but quickly drops off as the energy increases. The double Higgs-Strahlung cross-section varies in a similar way to that of the radiation off of tops but each stage changes more gradually. The cross-section for the double W fusion process gradually increases as the centre of mass energy increases. The variations of the cross-sections can be seen in Figure 2.9.

## 2.4 Higgs Decays *written by Aaron Byrne*

Once the Higgs bosons have been produced, they need to be detected. Due to the nature of the Standard Model Higgs, with zero spin and no charge, and due to its short lifetime of the order of  $10^{-22}$  seconds [12], it is impossible to measure the Higgs directly. Therefore, we need to know what the Higgs particles will decay into in order to be able to detect its decay products, which may allow some properties of the Higgs to be calculated by looking at the properties of the decay products.

### 2.4.1 Higgs Decay Processes

The Higgs boson can decay in a variety of ways. It can decay into a fermion - antifermion pair, a pair of massive gauge bosons (W and Z Bosons) or a pair of massless gauge bosons (gluons and photons). The main processes that it can decay via are shown below [13].

- Bottom - Anti Bottom pair
- Tau - Anti Tau pair
- Muon - Anti Muon pair
- Charm - Anti Charm pair
- Gluon - Gluon pair
- Photon - Photon pair
- Z - Photon pair
- WW Boson pair
- ZZ Boson pair

The majority of the decays are relatively simple to detect in a detector. However, the decay into a WW or ZZ boson pair can be hard to measure, as one of the bosons produced has to be virtual as the Higgs is not massive enough to be able to decay into two real versions of either of the bosons and obey conservation laws, as twice the mass of either of the bosons comes to a greater value than the Higgs mass we are going to be using, which is  $125\text{GeV}$ .

The properties of the virtual bosons cannot be measured in the detector, but they decay to real particles that can be detected. If the Higgs does decay into WW\* or ZZ\* pairs, then the decays of these bosons will have to be measured in order to obtain the Higgs properties. The W bosons can decay into a lepton and its corresponding neutrino, which causes problems as the neutrino cannot be detected in the detector so there will be missing information. W bosons can also decay into a up-type anti-down-type quark pair. However, background processes from electron and positron collisions produce similar pairs of particles, so telling these events apart is difficult. Z bosons, however, decay into a fermion and its anti-fermion equivalent. This is easy to distinguish from background processes, and so ideally ZZ\* decay is preferred to be measured over WW\* decay, but the WW\* decay mode is more likely for a  $125\text{GeV}$  Higgs, as shown in table 2.3. So errors will arise if WW\* and ZZ\* are used to calculate the Higgs properties.

This all has to be taken into account when measuring the properties of the Higgs via conservation laws, as particles may have to be separated from background particles, which may give rise to errors in the data.

### 2.4.2 Higgs Decay Branching Ratios

Each of the decay modes of the Higgs occurs a percentage of the time, so the probability of the Higgs decaying into each of these pairs of particles, also known as the branching ratio, needs to be found for each process. These branching ratios depend on the mass of the Higgs, as shown in Figure 2.10. From Figure 2.10, it can be seen that  $b\bar{b}$  decay dominates at low Higgs mass and WW decay dominates at high Higgs mass. The Higgs being searched for is a Standard Model Higgs with a mass of the order  $125\text{GeV}$  [15], as given by the analysis of data from the LHC collisions. The decay processes and their branching ratios, along with uncertainties [16], for the  $125\text{GeV}$  Higgs are shown in table 2.3. It is clear that the particles the Higgs will decay into the majority of the time is the  $b\bar{b}$  quark pair, decaying by this process in 57.7% of cases. When detecting the decays, this will be the main process looked for in the detector. The next most common decay is the decay into WW bosons, occurring 21.5% of the time. So

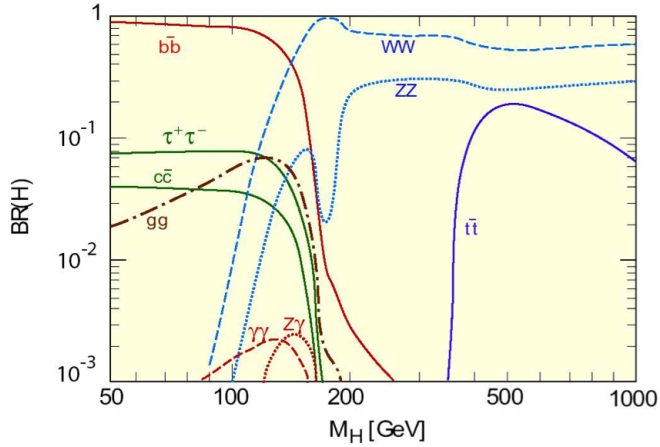


Figure 2.10: The Higgs decay branching ratios for varying Higgs masses.[14]

Table 2.3: Decay Modes and their corresponding branching ratios for a Standard Model Higgs boson [16].

Decay Mode	Branching Ratio	Uncertainty
$b\bar{b}$	0.577	+3.2% -3.3%
$WW^*$	0.215	+4.3% -4.2%
$gg$	0.0857	+10.2% -10.0%
$\tau^+\tau^-$	0.0632	+5.7% -5.7%
$c\bar{c}$	0.0291	+12.2% -12.2%
$Z\gamma$	0.00154	+9.0% -8.8%
$ZZ^*$	$2.64 \times 10^{-2}$	+4.3% -4.2%
$\gamma\gamma$	$2.28 \times 10^{-3}$	+5.0% -4.9%
$\mu^+\mu^-$	$2.19 \times 10^{-4}$	+6.0% -5.9%

when looking for decays of the Higgs, the two major processes to be looked for are decays to bottom - anti-bottom and  $WW^*$  boson decays. Also, it should be noted that the decay to  $t\bar{t}$ , or top - anti-top, does not occur at a Higgs mass of  $125\text{GeV}$ . As the Higgs couples to mass, and top quarks are the most massive, it would be expected that the Higgs would decay to  $t\bar{t}$  the majority of the time. However, the top is so massive that the Higgs cannot produce a  $t\bar{t}$  pair until it has a much higher mass, due to conservation laws. This is shown on Figure 2.10 where the  $t\bar{t}$  decay line does not occur until near a Higgs mass of  $350\text{GeV}$ .

## 2.5 Coupling *written by Raveena Deol*

The interaction of the Higgs boson with other particles can be described by coupling. In the Standard Model, this type of coupling is fixed and is proportional to the mass of the particle that the Higgs couples to. The strength of the force exerted in this interaction is determined by the coupling constant,  $g$ , which is a dimensionless value. The coupling constant can be described as being either ‘weak’ or ‘strong’ depending on whether this value is less than or greater than one respectively.

We will be focusing on four main couplings:

1. Higgs Coupling to Fermions
2. Higgs Coupling to Photons
3. Higgs Coupling to Weak Bosons
4. Higgs Self-Coupling

### 2.5.1 Higgs Coupling to Fermions *written by Ryan Jones*

Higgs coupling to fermions is important to consider, particularly at low energies where such processes will be dominant due to the high branching ratio of Higgs decay into fermion antifermion pairs, the most significant being decay into  $b\bar{b}$  when looking at centre of mass energies of around  $300\text{GeV}$ . A collider environment provides the ideal place to observe Higgs coupling, because the decay of other particles produced as a result of the collision will produce all the fermion antifermion pairs that we want to observe, with  $b\bar{b}$  being of particular interest. This is in addition to the Higgs coupling to its own decay products, which can be seen in Figure 2.11. This particular

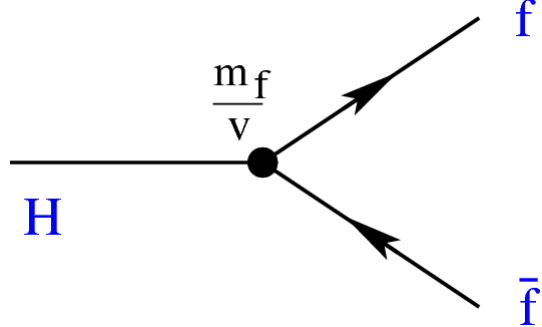


Figure 2.11: Feynman diagram depicting Higgs coupling to fermions, with the proportionality of such coupling displayed.

coupling is mediated primarily by the Yukawa interaction, which describes the interaction between a scalar field and a vector field. The Higgs field is scalar, fermion fields are vector, hence why it is utilised here, beyond its usual application in describing strong interactions between fermions [7]. The coupling of the Higgs particle to these fermions is proportional to the mass of the fermion in question, seen as follows:

$$g_{H \rightarrow f\bar{f}} = \frac{\sqrt{2}m_f}{v} \quad (2.20)$$

where  $g_{h \rightarrow f\bar{f}}$  is the coupling constant for that particular fermion,  $m_f$  is the mass of the fermion, and  $v$  is the vacuum expectation value, which as stated previously, is experimentally derived to be  $246\text{GeV}$ . As a result, the dominant decays of the Higgs boson to fermions are primarily to the third generation quarks and leptons where possible, although at lower energies  $t\bar{t}$  coupling to Higgs cannot be observed because the minimum energy required to produce 2 top quarks is around  $350\text{GeV}$ , or  $2m_t$ ; this is one of several reasons that higher centre of mass energies, on the TeV scale, are to be utilised for observation of the Higgs particle.

### 2.5.2 Higgs Coupling to Photons *written by Russell Turner*

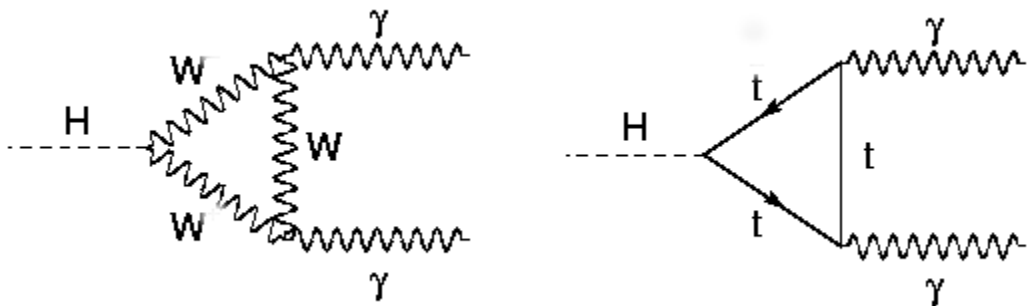


Figure 2.12: Feynman diagrams of the 2 basic mechanisms for Higgs to photon decay [11]

Another decay channel for the Higgs particle is  $H^0 \rightarrow \gamma\gamma$ . While this seems counter-intuitive, since the Higgs field couples to mass and the photon is massless, the fact that the Higgs decays to a particle and antiparticle means that

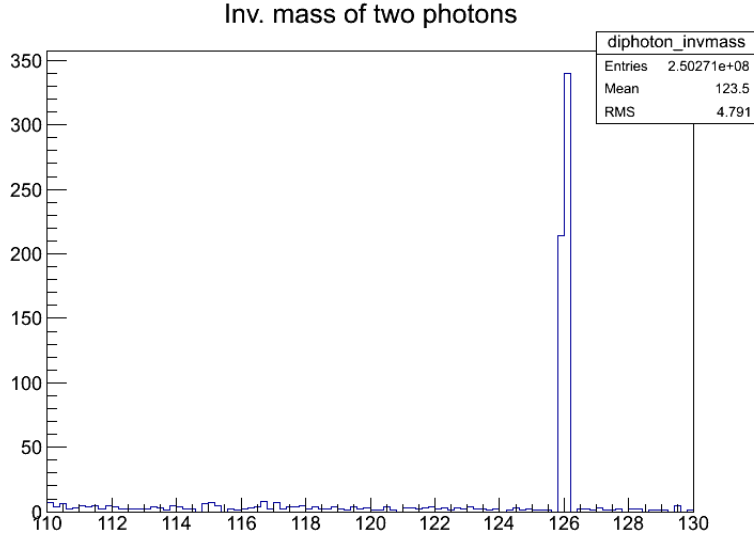


Figure 2.13: Histogram of the invariant mass of photon pairs. The peak seen can be attributed to the Higgs particle

it can also decay into two photons via a heavy particle loop. This is most likely to occur via the top quark or the W boson, as seen in Figure 2.12, since these are the most massive of the charged elementary particles.

The consequence of this is that the coupling of the Higgs to the photon decay channel is linked to its coupling to the  $t\bar{t}$  and  $WW$  decay channels. More explicitly, the coupling of this decay mode can be written as the sum of two loop coefficients:

$$\begin{aligned}
 c^{\gamma\gamma} &= c_\gamma^{(t)} + c_\gamma^{(W)} \\
 &= \frac{2}{9}A_t(\tau) - \frac{7}{8}A_W(\tau) \\
 A_t(\tau_t) &= \frac{3}{2\tau_t^2} \left[ (\tau_t - 1) \arcsin^2(\sqrt{\tau_t}) + \tau_t \right] \\
 A_W(\tau_W) &= \frac{1}{7\tau_W^2} \left[ 3(2\tau_W - 1) \arcsin^2(\sqrt{\tau_W}) + 3\tau_W + 2\tau_W^2 \right] \\
 \tau_x &= \frac{m_H}{4m_x^2}
 \end{aligned} \tag{2.21}$$

[4]. From this, the measurable branching ratio of the  $\gamma\gamma$  decay channel can be calculated, and the theoretical value of this is  $2.28 \times 10^{-3}$  with a relative error of  $+5.0\%$  and  $-4.9\%$ .[22] This value can be confirmed by using a pythia based simulation. By creating a histogram of the mass of  $\gamma\gamma$  pairs, and integrating over the  $126\text{GeV}$  peak, the number of  $\gamma\gamma$  decays is found. By dividing this by the total number of Higgs events (here  $N = 273498$ ), a branching ratio of  $(2.066 \pm 0.09) \times 10^{-3}$  which is within three standard deviations of the theoretical value. Despite the small discrepancy, the two values are close enough to serve as a soft confirmation of the theoretical value.

### 2.5.3 Higgs Coupling to Weak Bosons *written by Matthew Heath*

An important interaction to observe and quantify over the course of the collider's operation will be that of the Higgs particle's coupling with the  $W^\pm$  and  $Z^0$  bosons. The coupling of the Higgs to these weak gauge bosons is proportional to the squared mass of the W/Z boson, as opposed to just the mass in the case of fermion coupling, by the relation [22]

$$g_{h \rightarrow VV} = \frac{2M_V^2}{v} \tag{2.22}$$

where  $g$  is the coupling value,  $V$  is either  $W$  or  $Z$  and serves to distinguish the type of massive vector gauge boson,  $M$  is the mass of said boson, and  $v$  is the vacuum expectation value of the Higgs field described by [22]

$$v = \left( \sqrt{2} G_F \right)^{-\frac{1}{2}} \quad (2.23)$$

which is defined by the Fermi coupling constant  $G_F$  and gives a value of  $v \approx 246\text{GeV}$ . When the masses of the  $W$  ( $M_W = 80.385\text{GeV}$ ) and the  $Z$  ( $M_Z = 91.1876\text{GeV}$ ) bosons are used in conjunction with Eqn. 2.22, values of  $g_{H \rightarrow WW} = 52.53$  and  $g_{H \rightarrow ZZ} = 67.60$  are obtained, showing that the Higgs boson should couple to these bosons very strongly.

As can be seen in Table 2.3, the most likely decay mode is that to a bottom-antibottom quark pair, although coupling to mass means that the Higgs should decay to the heavier  $W$  and  $Z$  bosons preferably to the other lighter particles. This is due to particles always decaying in their rest frame, and the mass energy of the Higgs is not sufficient to produce two real  $W/Z$  bosons, instead requiring that it decay by emitting one real and one virtual boson. This leads the decay to weak gauge bosons to be suppressed by the decay channels where the Higgs can couple to two real particles [30].

A similar explanation is also applicable for why the  $H \rightarrow WW$  decay is more probable than  $H \rightarrow ZZ$ . The  $Z$  boson possesses a higher mass than that of the  $W$  boson and so the virtual  $Z$  that is produced in the latter interaction would be more virtual than the virtual  $W$  produced in the former interaction, leading to suppression of that rate. Furthermore, due to there being a positive and a negative state for the  $W$  boson due its complex wavefunction, while the  $Z$  is described by a real wavefunction, the probability of the Higgs decaying to  $WW$  includes a factor of 2 over that of decaying to  $Z$  bosons [30].

Measuring the coupling to  $W/Z$  bosons are of particular importance to understanding the properties of the  $125\text{GeV}$  Higgs particle. Only a Standard Model Higgs boson would have a greater probability of decaying to  $W$  or  $Z$  bosons over two photons or a  $Z$  plus a photon as the Higgs interacts with the massive weak bosons directly, while a non-Higgs particle would either interact indirectly with  $W/Z$  and very rarely decay to them or have directly interact with photons with a strength similar to that with which it interacts with  $W$  and  $Z$  particles, decaying to them all with similar rates. In addition to this, if the measured branching ratios of the  $WW$  or  $ZZ$  decay modes are smaller than the theorised values, the particle being studied may be more complicated than a Standard Model Higgs particle or that multiple different Higgs bosons exist in nature, requiring revision of the currently understood model [30].

#### 2.5.4 Higgs Self-Coupling *written by Raveena Deol*

Observing the self coupling of one Higgs boson to another in our  $e^+e^-$  collider can provide information on the Higgs potential. We can measure the self-coupling directly from Higgs pair production in the event of the  $e^+e^-$  collision. There are various ways that can produce two Higgs particles in one collision and each occur at different centre of mass energies of the colliding beams. The three main process are, double Higgs-Strahlung, double  $W$ -fusion and  $Z$ -fusion.

Double Higgs-Strahlung occurs most frequently between the energies of  $500\text{GeV}$  to  $1\text{TeV}$  via the process  $e^+e^- \rightarrow HHZ$  as shown in Figure 2.14. We can also observe the  $Z$  boson decaying into a quark-antiquark pair and therefore see the final products as:  $e^+e^- \rightarrow HHb\bar{b}$ .

Above the energies of  $1\text{TeV}$ , the dominating process for double Higgs production is the  $WW$  fusion process  $e^+e^- \rightarrow HH\nu_e\bar{\nu}_e$ . This is shown in Figure 2.15.

Double  $ZZ$ -fusion is not seen as frequently as the other two processes, as the electron- $Z$  coupling is small, so we will focus on double Higgs Strahlung and double  $WWW$  fusion. Since the first stage of the collider will run at a centre of mass energy of  $300\text{GeV}$  we do not expect to observe Higgs pair production. However at energies above  $500\text{GeV}$  we begin to observe the self-coupling. Figure 2.16 below shows how the cross-section for double Higgs production varies with the centre of mass energy.

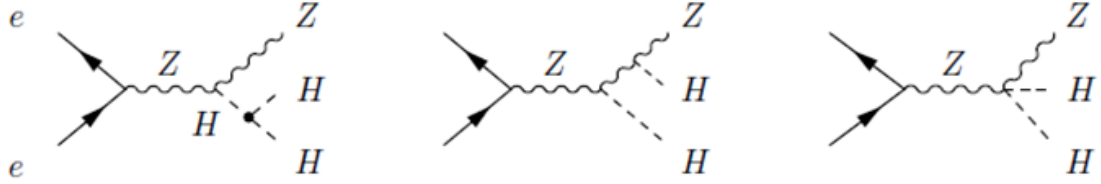


Figure 2.14: Feynman diagrams showing the production of two Higgs particles via Higgs-Strahlung [27].

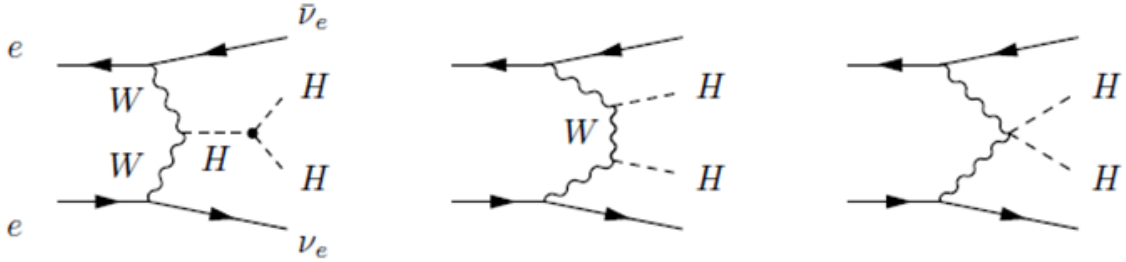


Figure 2.15: Feynman diagrams showing the production of two Higgs particles from the WW fusion process [27]

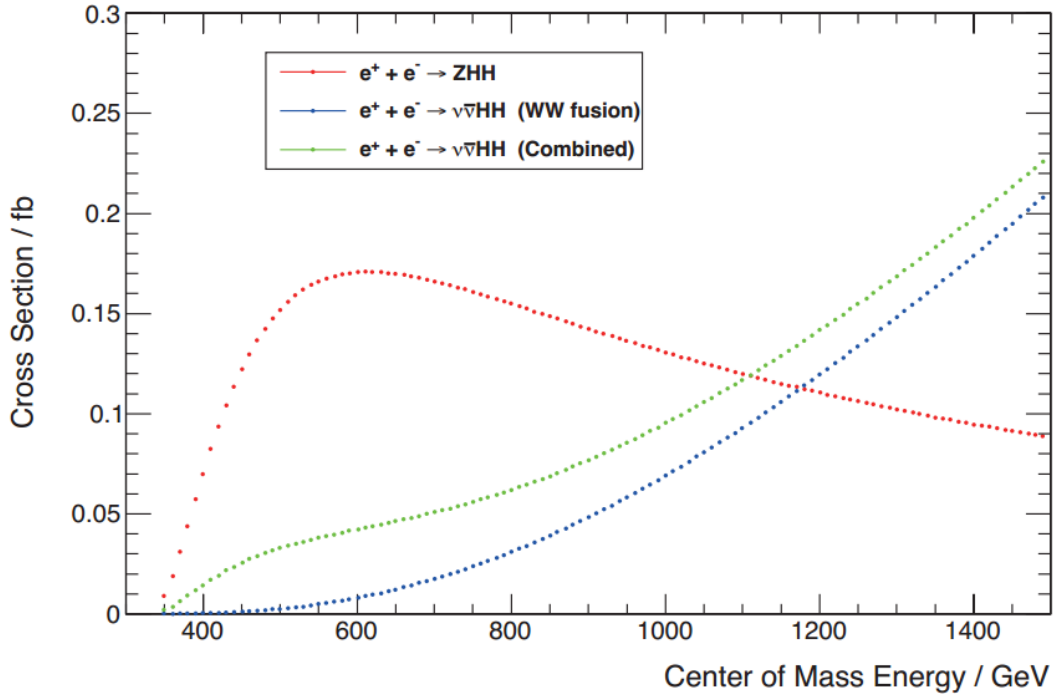


Figure 2.16: Graph to show how the cross section for Higgs pair production varies with the centre of mass energy via the processes double Higgs-Strahlung and double WW-fusion [28].

As seen in Figure 2.16 increasing the centre-of-mass energy of the collider will continue to increase the cross section of double WW Fusion. Therefore we will benefit from running the collider at energies much higher than 1TeV as well as at 1TeV.

We can use the coupling constant as a measure of the strength of this coupling, and in the Standard Model we obtain:

$$M_H = \sqrt{2\lambda}v \quad (2.24)$$

where  $v$  is the vacuum expectation value and is equal to  $246\text{GeV}$ ,  $M_H$  is the mass of the Higgs boson and  $\lambda$  is the coupling constant [29]. If we take the mass of the Higgs boson to be  $125\text{GeV}$ , we can rearrange equation 2.24 to give  $\lambda = 0.129$ .

Measurement of the tri-linear self coupling provides probability for exploration of the Higgs potential [29] and direct information on the Higgs potential responsible for electroweak symmetry breaking.

## 2.6 Other Higgs Properties

### 2.6.1 Mass written by Andrew Clarke

To determine the precision of the measurement of the mass of the Higgs boson we must consider both the theoretical predictions and current measurements. The mass of the Higgs boson is not predicted by the Standard Model, meaning that there is no precision that we can measure so that a theory can be tested. This means we will consider current experimental limits. The mass of the Higgs boson has been determined at the LHC and was found to be  $125.09 \pm 0.24\text{GeV}$  [20]. There are however, no measurements of the Higgs mass from electron positron colliders, which will be able to provide much more accurate results.

Due to the fact that there is no comparable experiment or any predictions of the mass of the Higgs boson, simulations were carried out. Events were generated in Pythia which also provides cross-sections at various energies.[21] These events were then fed into a second program called Delphes which simulate what happens when an event occurs within a detector, see section 5.11. [173]. The events are smeared and appear as they would do if they had happened within a detector. These simulations allow us to view what the peaks would look like inside our detector. Figure 2.17 shows the reconstruction of Higgs events at  $300\text{GeV}$  and  $1\text{TeV}$ . The production process that dominates at these energies is the Higgs-Strahlung process. The program takes two jets and finds the invariant mass of them if there is a final state that corresponds to a Higgs decay (into quarks) and a Z boson decay into a lepton and its corresponding anti-lepton. This is done by seeing if the final state contains two jets and either two muons, two electrons or more than  $91\text{GeV}$  of missing energy (corresponding to a Z boson decaying into two neutrinos). The decays of Z bosons into hadrons were not taken into account despite the fact that the Z decays into hadrons  $(69.91 \pm 0.06)\%$  [22]. This is because it is difficult to take into account the four jets as they are not well defined objects within the program.

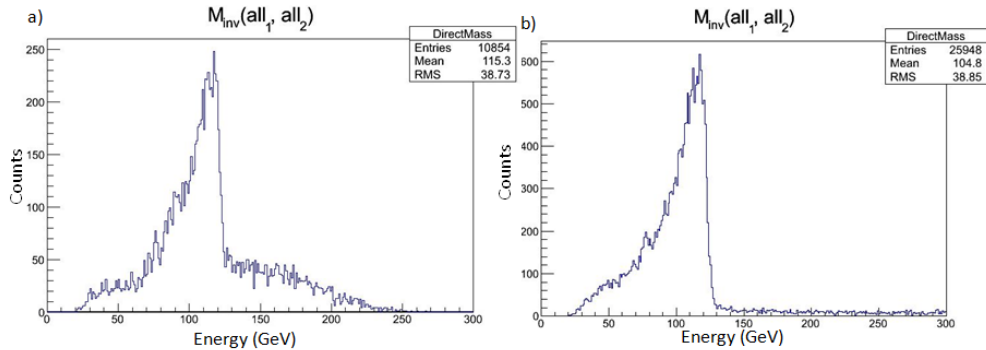


Figure 2.17: The mass of the Higgs reconstructed using jets at energies of a)  $300\text{ GeV}$  and b)  $1\text{TeV}$ .

Figure 2.17 shows that the peaks appear to be centred at a value around  $125\text{GeV}$ . This may be due to a calibration error within the simulation. To calibrate the simulation the Z boson would be investigated. The Z boson decays into quarks  $(69.91 \pm 0.06)\%$ , reconstructing the jets produced from these events will produce the mass of the Z

boson[22]. The mass of the Z boson is known accurately so any deviation from this within the simulation would be clear to see. This would then allow a calibration factor within Delphes to be changed so that the peak appears at the correct energy.

The peaks were then looked at closer and were fitted with Gaussian curves as shown in Figure 2.18. These plots show that the peaks cannot be fitted very well. This means that the simulations are limited in their application to determining an error on the Higgs boson mass. The error on the mean value is  $\pm 0.1$  which corresponds to the error on the Higgs mass. The fit of the data can be seen more clearly if a larger energy range is looked at as shown in Figure 2.19.

Since the final state is known it is possible to measure the mass of the Higgs boson indirectly. This is done

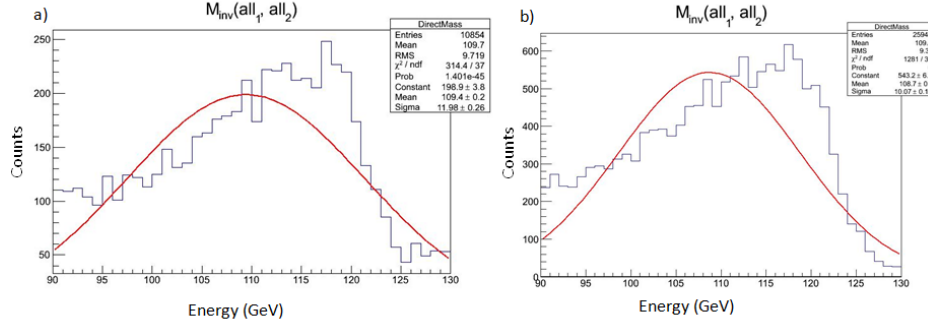


Figure 2.18: The Higgs mass peaks fitted at a)300GeV and b)1TeV.

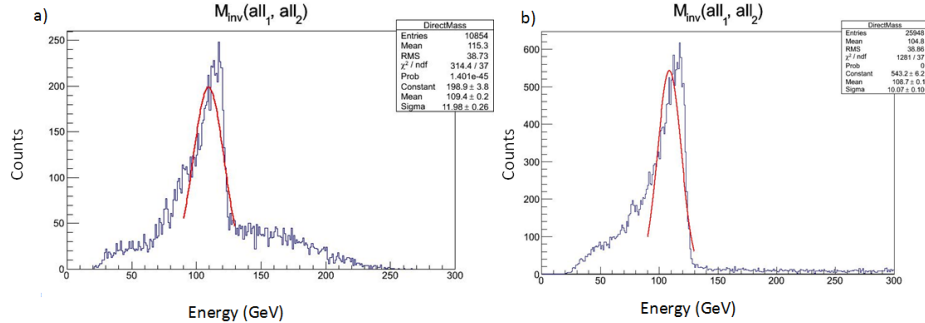


Figure 2.19: The Higgs mass peaks fitted at a)300GeV and b)1TeV.

by taking the final states with two muons and two jets in the final state. The invariant mass of the two muons can be found which gives the mass of the Z boson. The momentum of the Z boson can also be determined and so relativistic kinematics can be used to find the mass of the Higgs boson (see section 2.3). This indirect way of measuring the mass of the Higgs boson gives a much cleaner peak as the resolution of muons is much better than that of jets. However, there are fewer events so the result is statistically less accurate. This means the error on the indirect mass of the Higgs is large due to the low number of events. The direct mass measurements are more statistically accurate because there are more events and so the error on the peak is reduced.

Figure 2.20 shows the indirect mass simulation of the Higgs boson. The peak near 300GeV is created due to very small jets being produced in events so most of the energy and momentum is with the muons. Again the peak needs to be fitted to see what mass and error is produced. The data has been fitted with a Gaussian as shown in Figure 2.21. The error is much larger on this fit at  $\pm 0.7\text{GeV}$ , which is due to errors on the mass of the Z boson, the momentum and energy of the muons all being used in the method. The simulation run at 300GeV produces a root mean square (rms) value of 9.719 GeV with 10854 entries. This will give an error on the mass of the Higgs of 0.0933GeV. The simulation at 1TeV has 25948 events and a rms value of 9.31GeV, giving rise to an error of 0.0578GeV. Taking into account both simulation results and the error of the measurements at the LHC, we will attempt to measure the mass of the Higgs boson to an accuracy of 0.05GeV.

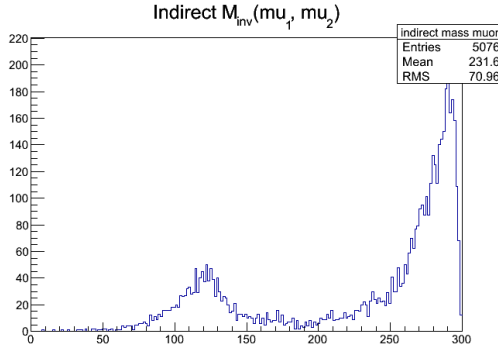


Figure 2.20: The mass of the Higgs found indirectly.

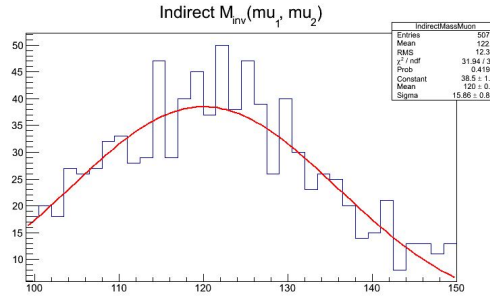


Figure 2.21: The indirect mass of the Higgs boson fitted with a Gaussian.

### 2.6.2 Spin and Parity *written by Aaron Byrne*

Properties of the Higgs boson were studied in depth using data from the ATLAS experiment at the LHC. The data gathered allowed the spin and parity of the Higgs produced at the LHC to be measured, with the results showing zero spin and a positive parity, i.e.  $J^P = 0^+$ , with confidence levels of over 97.8% [13]. The Standard Model also predicts that the Higgs would have these values for the spin and parity, allowing the Higgs produced at the LHC to be identified as the Standard Model Higgs. As LEPIC is initially looking at the Standard Model Higgs, it will have to be verified that the Standard Model Higgs, and not a non-Standard Model Higgs, is being produced in the collider.

To confirm that the Higgs produced in this accelerator is the same as that produced at LHC, and is hence the Standard Model Higgs, the values of parity and spin of the particle have to be calculated, as they cannot be directly measured. In order to do this, the decays of the Higgs produced will be studied. If the Higgs decay is observed to produce two photons, it rules out  $J^P = 1^\pm$ , as a spin-1 particle cannot decay into two identical spin-1 particles, as stated by the Landau-Yang Theorem [17].

The spin of the Higgs can be determined by studying energy dependence of the Higgs production cross section. For any spin-0 particle, the increase in the cross section should roughly be equivalent to the velocity of the boson in the centre of mass frame. By taking a series of measurements for the cross section just above the threshold energy of  $HZ \rightarrow q\bar{q}l^+l^-$ , and comparing the theoretical values to the measured values, we can confirm if the Higgs produced is spin-0 or not [18][19].

The parity of the Higgs can be determined by looking at the decay of the Higgs into a  $\tau^+\tau^-$  pair. The parities of the  $\tau^+$  and  $\tau^-$  can be determined in the detector by looking at the angular distributions of the  $\tau$  decays. In order to do this the  $\tau^+\tau^-$  pair needs to be reconstructed from their decay products. Once the parities of the  $\tau^+$  and  $\tau^-$  have been determined, they can be multiplied together, as parity is multiplicative, and hence the parity of the Higgs can be found [18][19].

## 2.7 Required Collider Parameters *written by Thomas Lane*

### 2.7.1 Luminosity

The luminosity of a particle collider is a very important factor into how successful the collider will be when taking measurements of collisions. It is directly proportional to the number of events that will occur when the two beams collide, with the equation for the rate being  $R=L \times \sigma$ , where  $\sigma$  is the cross-section for the desired production mechanism at the centre of mass energy of the collision. Therefore it is important to maximise the luminosity of the collider to ensure that we produce a high enough number of events to make precise measurements for the Higgs mass and coupling constants. The luminosity of a collider is given in its simplest form by equation 2.25.

$$L = \frac{N_1 N_2 f_{rep} n_b}{4\pi \sigma_x \sigma_y} \quad (2.25)$$

Equation 2.25: The Luminosity of a particle collider can be determined from the bunch populations per beam  $N_1$  and  $N_2$ , the beam repetition frequency  $f_{rep}$ , the number of bunches per beam  $n_b$  and the horizontal and vertical components of the beams  $\sigma_x$  and  $\sigma_y$ . The number of particles per beam are normally equal so  $N_1 = N_2$ .

However this equation does not take into account any losses or enhancements that occur when colliding oppositely charged particles into each other. For example, in order to avoid unwanted collisions between the produced particles and the incoming beams, we need to collide the two beams at a small crossing angle,  $\theta$ . This small angle causes a loss in the luminosity which is related to the crossing angle factor,  $S$ , where  $S$  is given by equation 2.26 below. The use of crab cavities can however remove this loss of luminosity.

$$S = \frac{1}{\sqrt{1 + (\frac{\sigma_s}{\sigma_x} \tan(\frac{\theta}{2}))^2}} \approx \frac{1}{\sqrt{1 + (\frac{\sigma_s \theta}{\sigma_x^2})^2}} \quad (2.26)$$

Equation 2.26: The crossing angle factor of a particle collision can be determined from the crossing angle  $\theta$ , and the scattering cross section  $\sigma_s$  which for a small crossing angle is much larger than  $\sigma_{x,y}$ .

Another effect that occurs when colliding two oppositely charged beams together is the hour glass effect, this arises because of a variation of the transverse beam size along the length of each bunch when the bunch lengths are comparable to or larger than the values of the betatron functions  $\beta_x$  and  $\beta_y$ . This variation occurs due to an increase in the betatron functions away from the interaction point, the betatron function for the quadrupole layout we shall be using in our collider is symmetric in the two planes, reaching its maximum and minimum values in the centre of the quadrupoles. This hour glass effect is more significant for long bunches and so to reduce this effect we shall use a small bunch length so that there is only a small variation of beam size along the bunch.

There are also some effects which only occur in a linear collider, which we will be using, for example the pinch effect from beamstrahlung radiation. The pinch effect refers to the fact that because the two beams are oppositely charged they then impose an attractive electric field on the opposing beam disrupting it, this disruptive field causes the two beams to become more focused and reduced in size, as shown in Figure 2.22, therefore enhancing the luminosity due to the smaller collision cross section. This enhancement factor,  $H_D$ , has a relation to the disruption factor,  $D_{x,y}$ , for flat beams shown in equation 2.27.

$$H_D = 1 + D_{x,y}^{\frac{1}{4}} \left( \frac{D_{x,y}^3}{1 + D_{x,y}^3} \right) [\ln(\sqrt{D_{x,y}} + 1) + (2 \ln(\frac{0.8\beta_{x,y}}{\sigma_z}))] \quad (2.27)$$

Equation 2.27: The Pinch Effect of two colliding beams can be calculated using this equation[31], where the final added term is the hour-glass term and  $D_{x,y}$  is the disruption factor which is equal to  $\frac{2N_r e}{\gamma} \frac{\sigma_z}{\sigma_{x,y}(\sigma_x + \sigma_y)}$ . This equation has been found through simulation by K. Yokoya, D. Shulte and M. Pivi.

As this enhancement factor takes into account the luminosity losses due to the hour glass effect this then leaves the equation for the instantaneous luminosity of our linear collider as equation 2.28 below.

$$L = \frac{N^2 f_{rep} n_b}{4\pi \sigma_x \sigma_y} \cdot H_D \cdot S \quad (2.28)$$

Equation 2.28: The total instantaneous luminosity for our collider can be calculated using this equation.

From the instantaneous luminosity calculated using equation 2.28 we can then calculate the integrated luminosity that our collider will produce over its running period. This integrated luminosity is calculated using equation 2.29 and from this integrated luminosity we can calculate the number of events that will be produced by the collider during its run time by multiplying the integrated luminosity by the cross section for the Higgs production at the centre of mass energy of the collider.

$$L_{int} = \int_0^T L(t)dt \quad (2.29)$$

Equation 2.29: The integrated luminosity for our collider can be calculated by integrating the instantaneous luminosity with respect to time, with the upper limit of the integral being the time for which the collider will run.

Therefore to produce a large number of events in our collider we need to maximise the beam repetition frequency and the number of bunches per beam, while minimising the product of the horizontal and vertical components of the beam, also we need to ensure that the length of the beam is short so that we do not encounter a large change from the hour glass effect. However due to the fact that bremsstrahlung losses are inversely proportional to the sum of the horizontal and vertical components of the beam we need to keep this relatively large, and so we shall be using a wide flat beam.

To calculate the instantaneous luminosity that we need to produce in our collider we used our desired precision for the branching fractions of the Higgs decay schemes to calculate the number of events we would need to produce for these precisions, these are shown in table 2.4. We then decided that as the Higgs decaying to two muons, two photons and a Z boson with a photon had such a small branching ratio the instantaneous luminosity required to measure the theoretical precision was much higher than our collider could produce, therefore we will not try to measure the branching fractions for these decay modes but instead will monitor them and try to give a limit for the branching fractions. After we had decided this we then calculated the integral luminosity that would be needed to measure our desired precision of 4 percent on the ZZ decay mode, and from this we found that our collider would have to produce an instantaneous luminosity of at least  $1.85 \times 10^{35} cm^{-2}s^{-1}$  for one year's operating time.

Table 2.4: The Higgs decay modes and our desired precision measurements of their branching fractions.

Decay Mode	Branching Fraction	Desired Precision (%)	Required Number of Decays	Total Events Required	Required Integral Luminosity ( $fb^{-1}$ )
b b-bar	0.577	3	815	1412	7.059
c c-bar	0.0291	11	2757	94756	473.776
$\tau\tau - bar$	0.0632	5	5929	93816	469.079
$\mu\mu - bar$	$2.19 \times 10^{-4}$	5	1826084	8338283189	41691415.942
$\gamma\gamma$	$2.28 \times 10^{-3}$	4	273498	119955179	599775.893
Z Z	0.0264	4	23049	873078	4365.387
W W	0.215	4	2282	10614	53.069
Z $\gamma$	$1.54 \times 10^{-3}$	8	101305	65782331	328911.652
g g	0.0857	9	1317	15369	76.844

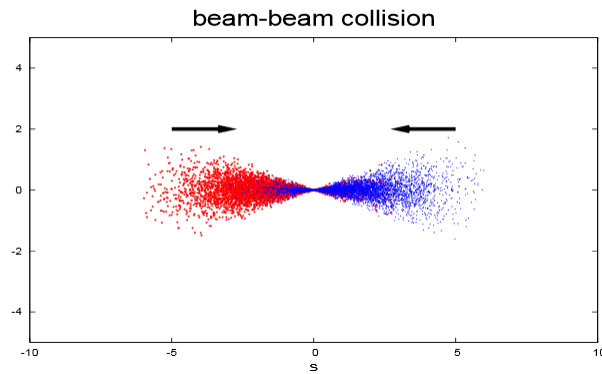


Figure 2.22: A simulation of the pinch effect for two colliding beams[32].

## 2.7.2 Energy

The energies that we shall be running our collider at in order to investigate the properties of the Higgs boson are 300GeV and 1TeV. We have decided to run the collider at 300GeV to investigate the mass, spin and parity of the Higgs because, as can be seen in Figure 2.9, the cross section for the production of the Higgs through the Higgstrahlung process peaks at around 250GeV and at 300GeV the production of the Higgs through the WW fusion and ZZ fusion processes is relatively low, leading to a small background of unwanted particle production. We have also decided to investigate the coupling of the Higgs at 1TeV because at this energy the process of double Higgs production is possible and so this allows us to investigate the Higgs self-coupling constant along with other decay schemes of the Higgs.

## 3 Beyond the Standard Model

### 3.1 Introduction *written by Christopher Francis*

Whilst the main aim of the brief is to measure Higgs properties with high accuracy and determine if it is a standard model Higgs, the high energy nature of the collider gives us the ability to probe energies that have not been thoroughly investigated in the  $e^+e^-$  environment before. These energy regimes could well be home to several undiscovered particles that may be useful in explaining physics beyond the standard model.

Several areas of interest were designated for initial research including compositeness, extra dimensions, supersymmetry, Z' physics and technicolour. However it was decided against pursuing all of these further as there would not be sufficient time given the resources available. Two main areas were decided upon to take forward, Supersymmetric particles and neutral heavy gauge bosons, both of which have particle classes that have never been directly observed before, and both provide an explanation to some of the problems plaguing the standard model. Simulation programs such as Whizard and DELPHES are used to generate events and smear them through a detector card respectively.

### 3.2 Unexplored Considerations

#### 3.2.1 Compositeness *written by Dwayne Spiteri*

Compositeness is the study of the possible substructure of particles which are thought to be fundamental. It is hypothesised that if electrons and gluons are composite particles, then new interactions among quarks and leptons will appear at the energy scales of the binding energies of the constituents[79]. The problem with focusing on compositeness is that it is not as justified theoretically as Z' or SUSY is. This means that there is less support for simulation software to include compositeness processes that allow it to be simulated, and in turn makes the theory less able to contribute to the function of the collider and/or the detector.

#### 3.2.2 Extra Dimensions *written by Christopher Francis*

Currently the standard model has four dimensions, 3 spatial and 1 time, however it may possible that these are not in fact the only dimensions. It is possible that there are dimensions that exist at too small a scale for us to see, however if we could find a way to look at their scale, which would be smaller than a subatomic particle, these hidden dimensions may become visible again. This is a possible theory to explain why gravity appears to be much weaker than the other fundamental forces as it may be spread across several of these dimensions, it is also a possibility for unifying gravity with these other forces. Some theories predict the existence of a gravitational exchange particle called the graviton which should be able to be produced at the LHC however as there is currently no experimental evidence for their existence it is possible that they are escaping almost immediately into the extra dimensions that we cannot see. Ultimately this theory was discounted for further investigation as its properties mean that it is not easily falsified.

#### 3.2.3 Technicolour *written by Lewis Simmons and John Cotterill*

Technicolour is a theory which was initially introduced to replace the Higgs mechanism in the process of Electro-Weak Symmetry Breaking (EWSB). This theory was able to replicate observations, and the properties of Higgs theory, for EWSB but without certain problems encountered by Higgs models. Instead of the conventional, elementary Higgs particle, it was theorised that this boson was actually a composite particle of techni-particles. These techni-particles interact with conventional SM particles via a new technicolour force. This force was originally based on QCD like dynamics and was exchanged by massive carrier bosons which generated their own mass. The exact mechanisms behind these theoretical interactions have been severely constrained through modern experimentation and the theory has been massively confined as a result [66][67][68].

The remaining plausible model which can account for a 125 GeV Higgs particle is known as Walking Techni-Colour (WTC). In this model the coupling of this new technicolour force deviates wildly from that of the QCD force the theory is based on. This requires vast amounts of fine tuning to acquire the correct coupling with energy relationship. It is due to this that technicolour theories have fallen out of favour in current times and have essentially been abandoned. A severe lack of phenomena predicted by these models being observed (e.g. flavour changing neutral currents) also hint that these theories are perhaps incorrect. It is due to this that technicolour has not been pursued directly within this project [67][68].

### 3.3 Exotic Heavy Neutral Gauge Bosons

#### 3.3.1 Introduction to $Z'$ *written by Lewis Simmons*

The  $Z'$  boson is a theorised particle which occurs in certain extensions to the conventional standard model. In brief, this boson is a much heavier variant of the conventional  $Z$  boson and should accompany  $W'$  bosons, which are similarly heavier  $W$  bosons. Like their lower mass counterparts, these particles act as weak force carriers and are a result of electroweak symmetry breaking via the Higgs mechanism.

These new bosons are expected to be detectable in future high energy collider environments, via both direct and indirect methods. For the collider being addressed throughout this project, particle beams will consist of electrons and positrons with energies up to 3 TeV. The net lack of charge in these electron-positron annihilation interactions makes producing the charged  $W'$  boson problematic. Because of this, the theorised  $Z'$  will be focused on. This particle can be produced in these  $e^+e^-$  interactions in an approach similar to that used for the standard model (SM)  $Z$  boson at LEP.

The maximum 6 TeV centre of mass energy this experiment can achieve is comparable to energies at the LHC. Despite this, an electron-positron system provides a much cleaner background when compared to similar energy hadron systems. It is due to this that a TeV scale electron-positron collider is ideal for investigating this new particle without sizeable problems eliminating background effects [62].

#### 3.3.2 Motivations *written by Lewis Simmons*

Like many other theorised phenomena within particle physics,  $Z'$  bosons arise from extensions to the conventional standard model. A multitude of theories have been proposed for the inclusion of  $Z'$  bosons. Each of these gives rise to a  $Z'$  with slightly different properties. In particular,  $Z'$  models tend to differ by producing a  $Z'$  boson with altered couplings to SM fermions. In this heavily model dependent field, any observed particle can have implications for far reaching areas such as Grand Unified Theories (GUT's) and may even help disprove certain hypotheses [59].

All  $Z'$  theories are based on the addition of extra U(1) gauge group(s) to the conventional SM. U(1) groups are phase transformation Lie groups and are already present within the standard model formulation. The U(1) group within the classical SM is associated with the electromagnetic force and gives rise to the associated neutral exchange boson, the photon. Adding more of these gauge groups to the standard model invokes additional neutral gauge boson(s). The particle resulting from this SM extension is known as a  $Z'$  boson. These will be distinct from the photon and  $Z$  which are currently present in the SM.

These new,  $U(1)'$  groups will be inferred via symmetry breaking and have not yet been observed. Despite this, most models predict the associated symmetry breaking at TeV scale energies, making this field relevant to next generation, high energy colliders. The breaking of symmetry in these gauge groups enables  $Z'$  phenomena to be observed. Unfortunately this additional  $U(1)'$  group will not impact any SM processes until symmetry is broken in these high energy scenarios. This is because we cannot measure absolute phases imparted by these groups, we instead measure quantum mechanical amplitudes. It is due to this that we cannot discount a  $Z'$  particle's existence from current observations/ data.

In most models, the  $Z'$  will act as a heavier Z boson and couple to fermions in the same or a similar way. In this discipline, which contains a variety of distinct models, there are 3 main schemes by which a  $Z'$  boson should exist [61]:

1. The first motivation for the inclusion of  $Z'$  bosons is based on the E6 grand unified theory (GUT) model for SM physics. In this regime, unification of forces is achieved in an E6 Lie group at incredibly high energies [59]. This E6 group can then decompose as a result of various symmetries being broken, giving 2 additional U(1) groups to the SM. This is achieved as follows:

$$E6 \rightarrow SO(10) \times U(1)_\psi \rightarrow SU(5) \times U(1)_\chi \times U(1)_\psi \quad (3.1)$$

The mixing of the  $U(1)_\chi \times U(1)_\psi$  groups determines the nature of  $Z'$  couplings to SM fermions within this model [63]:

$$Z'(\theta) = Z'_\psi \cos(\theta) + Z'_\chi \sin(\theta) \quad (3.2)$$

The SU(5) gauge group remaining accounts for the conventional SM. This theory is attractive as it supports notions such as SUSY, string theories and other beyond standard model phenomena [59]. These can be directly confirmed or ruled out by using observations of  $Z'$  particles and comparing their characteristics with those this model predicts. For example, this theory predicts a  $Z'$  particle with noticeably different couplings to SM fermions than the conventional Z boson [59] [60]. This acts as a signature “smoking gun” for new physics and will aid in determining which (if any) model describes any  $Z'$  particles produced.

2. Another popular model is simply adding a  $U(1)'$  group to the conventional standard model. This forms what is known as the Sequential Standard Model (SSM) and implies that the new  $Z'$  boson acts exactly the same as conventional Z bosons, just with a greater mass [63]. This scheme has the potential of easier detection and study as the normal Z boson characteristics have been carefully examined over the past decades. If, for instance, the couplings of the Z and  $Z'$  bosons were found to be the same, this model would be valid and the higher complexity models would be seriously constrained if not ruled out completely. This model is favoured due to its simplicity and requires no modification or inclusion of any new phenomena to the current standard model.

$$\text{Sequential Standard Model (SSM)} : SU(3)_C \times SU(2)_L \times U(1)_Y \times U(1)' \quad (3.3)$$

3. The third prominent theory behind possible  $Z'$  phenomena is known as the “Left Right Symmetry Model” or LRM. This theory draws parallels to that outlined above with the E6 proposal. In the case of LRM the SO(10) gauge group breaks into a different set of groups than displayed above. In particular a  $SU(2)_R$  group is formed along with a  $U(1)_{B-L}$  group [60] [63]. This restores parity for high energies in electroweak SM mechanisms balancing the asymmetry in W bosons preferably coupling of to LH fermions / RH anti-fermions. This is done by introducing the new  $W'$  boson which will couple in an opposite fashion to the W. The combination of these 2 particles restores coupling symmetry.

$$SO(10) \rightarrow SU(3) \times SU(2)_R \times SU(2)_L \times U(1)_{B-L} \quad (3.4)$$

In the SM gauge structure used currently, the components:  $SU(2)_L \times U(1)_Y$  give rise to the  $W^\pm$  and  $Z^0$  bosons. In this new structure,  $SU(2)_R \times U(1)_{B-L}$  give rise to the additional new  $W^\pm$  and  $Z'$  [63]. This theory is attractive for the same reasons as the E6 model above and implies a unification of forces at very high energies, around which a  $SO(10)$  gauge group can form.

In summary,  $Z'$  bosons may be simple additions to the conventional SM or relics of much more complex unification mechanisms at high energies. If  $Z'$  bosons of the SSM variety are found, this would further add to the multitude of observations which support the current SM formulation. If the  $Z'$  for example, exhibits different couplings to SM

fermions than anticipated, new physics has been found. This then supports a more complex formulation of the SM consistent with SUSY, string theory and/or other models depending on the exact  $Z'$  characteristics observed [62]

### 3.3.3 Search Strategy and Current Limits *written by Lewis Simmons*

In a method akin to that deployed at  $Z$  factories in past decades (LEP), a direct search for  $Z'$  bosons is an attractive concept at a high energy electron-positron collider. The neutral charge and high mass of a  $Z'$  boson make a high energy,  $e^+e^-$  environment suitable for production. This method nullifies the large hadronic backgrounds present for similar energy hadron colliders. For comparison, the Drell-Yan process for  $Z'$  production in hadronic collisions causes a sizeable background through non-interacting partons. In electron-positron collisions, there are no ‘fragment’ particles which do not interact and subsequently cause background [62]. The Feynman diagrams for  $Z'$  production shown in Figure 3.1 display where such backgrounds arise from:

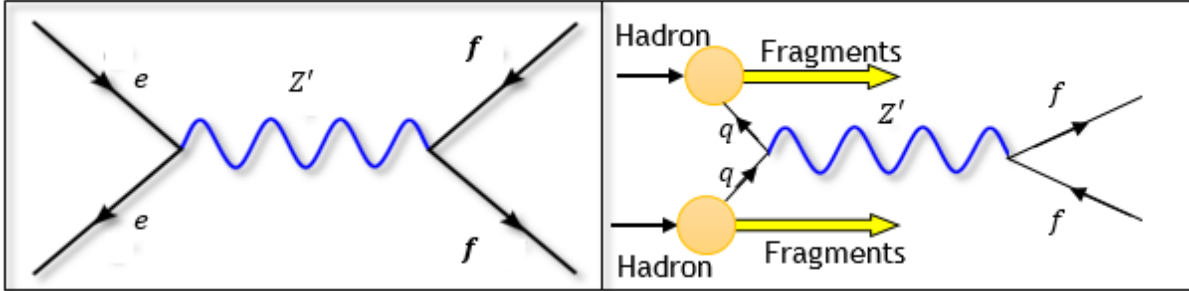


Figure 3.1: The conflicting production mechanisms for  $Z'$  boson production in lepton and hadron collisions. The Drell-Yan process (right) used in hadronic collisions has a greater background as a result of the non-interacting hadron fragments.

Using these processes at installations such as LEP and the LHC, limits have been established for the mass of the  $Z'$ . Unfortunately, much like the Higgs particle, a mass cannot be predicted via purely theoretically means for the  $Z'$  boson. It is due to this that  $Z'$  masses have been predicted to range from  $\sim 5\text{TeV}$  to more than  $\sim 50\text{TeV}$ . The only way to isolate the  $Z'$  mass or even prove the existence of such a particle is to perform further experimentation. Experiments can aim for either direct  $Z'$  production or confirmation of  $Z'$  existence via indirect means. Table 3.1 shows the current limits on the  $Z'$  mass from various models and experiments:

Table 3.1: The current (2015) limits on  $Z'$  boson mass from LHC experiments [64] [65]

Model	Observation	Mass Limit	Experiment
$Z'$ (SSM)	Dilepton ( $e\&\mu$ ) final states	2.69 TeV	CMS
$Z'$ (SSM)	Dilepton ( $e\&\mu$ ) final states	2.90 TeV	ATLAS
$Z'$ (E6)	Dilepton ( $e\&\mu$ ) final states	2.62 TeV	ATLAS/CMS

### 3.3.4 Detector Mechanisms *written by John Cotterill*

As the  $Z'$  boson is expected to behave in a similar way to the  $Z$  boson then the potential decay modes are to a lepton-antilepton pair and a quark-antiquark pair. Feynman diagrams for these processes are shown in Figure 3.2.

The decay mode to a di-muon final state in the lepton case will be considered more specifically. This is because the effects from Beamsstrahlung render additional photons within the detector. If these photons have sufficient energy to decay to an  $e^+e^-$  pair then this contributes to a background signal within the ECAL. Beamsstrahlung photons with sufficient energy to decay to a  $\mu^+\mu^-$  pair are rarer and so have less of a contribution to a background signal. The reduced background provides a cleaner signal such that a reduced integrated luminosity is required to obtain a significant result above background.

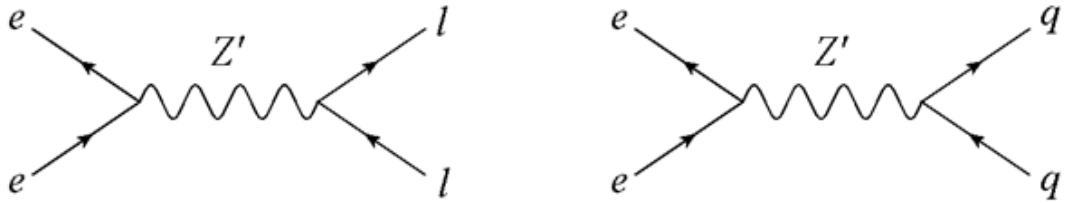


Figure 3.2: Feynman diagrams of the potential decay modes of the  $Z'$  boson.

The decay mode to quark-antiquark may also be investigated. However, the resultant quarks may radiate gluons giving rise to additional jets requiring detection. Consequently the signals produced are less clear for analysis compared to the di-muon decay mode. Difficulty in distinguishing between the quark types is an additional issue. It is therefore suggested that the di-muon decay mode is investigated primarily.

### 3.3.4.1 Direct Searches [34][35]

Real  $Z'$  production is possible providing the mass of the  $Z'$  boson is below the proposed maximum centre-of-mass energy of 6TeV. This direct observation of the  $Z'$  will be apparent as a resonance in the cross section of the associated decay mechanism at a centre-of-mass energy equal to the  $Z'$  mass. Should the  $Z'$  boson be identified in this manner, the mass can be determined by scanning across the  $Z'$  resonance peak.

A resonance will still be obtained if the centre-of-mass energy is higher than the  $Z'$  mass due to the Beamstrahlung effects. This mechanism involves the radiation of a photon by one or both of the colliding particles in the beams when they enter the Coulomb field of the opposing beam. This radiative effect results in a lower energy associated with the collision. Should the energy of the radiated photon be equal to the difference in the centre-of-mass energy and the  $Z'$  mass then a resonance will still be obtained assuming a high enough luminosity.

Simulations have been conducted using the Whizard [36] program to model  $Z'$  boson detection with varying centre-of-mass energy. Figure 3.3 shows the expected SM cross section and the cross section associated with the additional interference of the  $Z'$  boson. The centre-of-mass has been varied over the achievable range of LEPIC and a resonance peak obtained for a  $Z'$  boson mass of 3TeV.

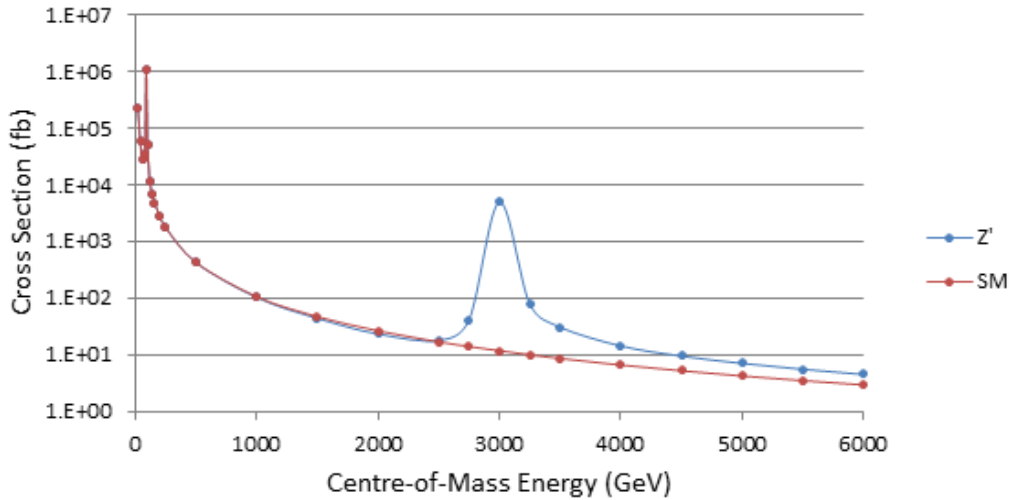


Figure 3.3: Cross section for di-muon production with varying centre-of-mass energy given  $M(Z')=3\text{TeV}$ . Values have been calculated using the Whizard [36] program.

Should the  $Z'$  be identified directly it would be possible to investigate any forward-backward asymmetry associated

with it. From this, determination of a mixing angle could be made. Due to the unlikelihood of producing  $Z'$  bosons directly, this investigation has not been considered in detail.

### 3.3.4.2 Indirect Searches [34] [35]

The  $Z'$  mass being ruled out below 2.7TeV to the 95% confidence level [37] by the LHC leaves a limited energy range for LEPIC to investigate the existence of the  $Z'$  through direct production. Indirect searches for effects from a  $Z'$  with  $M_{Z'} > \sqrt{s}$  are therefore important to consider. Should detection of a real  $Z'$  be unsuccessful, an extension of the lower limit of the mass can be made. The extent of this limit past the maximum centre-of-mass energy of 6TeV depends on the magnitude on an observed deviation from the expected SM cross section.

Indirect searches rely on a virtual  $Z'$  acting as an additional mediator of the weak force. Typically, the SM cross section for the weak neutral current interactions is dominated by effects from  $\gamma/Z$  interference. Assuming existence of the  $Z'$ , mixing occurs between the  $Z$  and  $Z'$ . Consequently, the measured cross section will be due to  $\gamma/Z/Z'$  interference and differ from that expected from SM  $\gamma/Z$  interference. This deviation in the observed cross section corresponds to the Beamsstrahlung tail of the  $Z'$  mass resonance above the maximum centre-of-mass energy. It is therefore possible to infer the existence of a  $Z'$  through a precise measurement of such a deviation. The precision of this measurement determines the limit on the  $Z'$  mass above the maximum centre-of-mass energy.

Simulations have been conducted using Whizard [36] to investigate the difference in cross section between SM interference and  $\gamma/Z/Z'$  interference. As before, the di-muon final state has been considered specifically due to this being easier to identify within the detector. A graphical representation of the SM interference with superimposed  $\gamma/Z/Z'$  interference curves of different  $Z'$  masses is not suitable. This is due to the deviations being so small that it is unobservable from such a graph. The most suitable method of representation is by comparing the SM and the  $\gamma/Z/Z'$  interference cross section obtained at 6TeV (where the deviation is maximum) as a function of the  $Z'$  mass.

The Beamsstrahlung tail present before the resonance peak in Figure 3.3 demonstrates the phenomena expected to be observed. An expanded representation of this tail is shown in Figure 3.4.

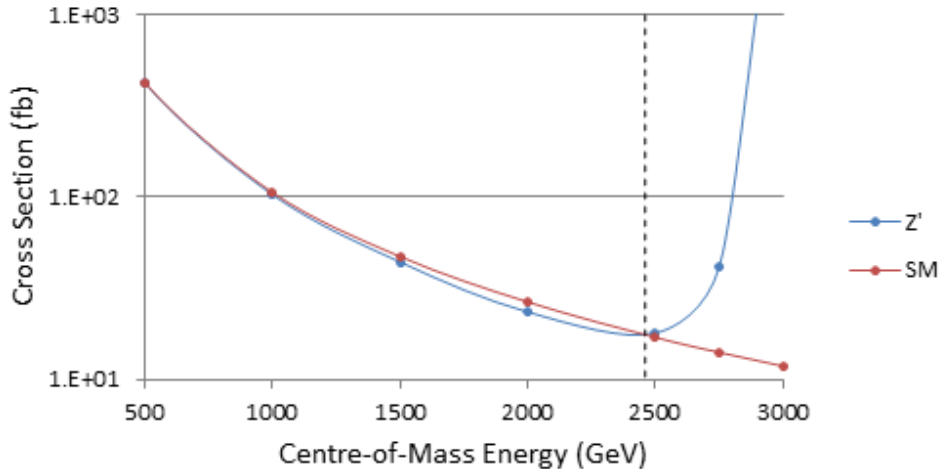


Figure 3.4: Expanded Beamsstrahlung tail for  $M(Z')=3\text{TeV}$ . The dashed line represents the point that the SM and the additional  $Z'$  interference cross sections are equal.

This tail is below the SM cross section curve before it reaches the resonance peak. It should also be noted that the deviation between the tail and the SM cross section reduces with a reduction in the centre-of-mass-energy (before the deviation is maximum). Therefore, for a fixed centre-of-mass energy of 6TeV, the  $\gamma/Z/Z'$  interference cross section should converge to the SM cross section from below with an increase of the  $Z'$  mass.

Figure 3.5 shows this expected behaviour. A peak is observed at the lower  $Z'$  mass region of the graph as the cross section is approaching the resonance at 6TeV. The point at which the two lines cross is equivalently labelled on Figure 3.4 by the dashed line.

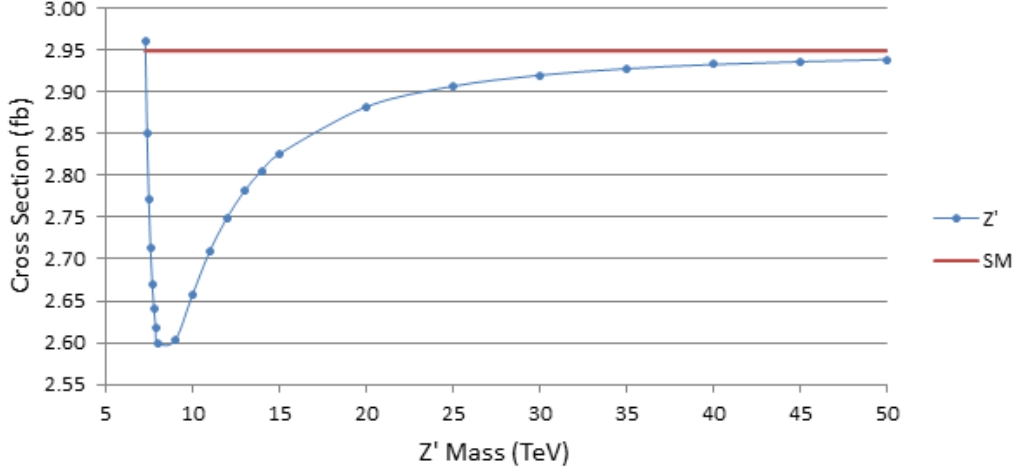


Figure 3.5:  $Z'$  effects on di-muon cross section at a 6TeV centre-of-mass energy with varying  $Z'$  mass.

### 3.3.4.3 Expected $Z'$ Mass Limit

The loss of energy corresponding to Beamsstrahlung effects results in a reduced number of particles interacting at 6TeV. Consequently, the maximum  $Z'$  mass inferring the existence of the  $Z'$  from the data collected by LEPIC is affected. Simulations have been performed over the centre-of-mass energy range of LEPIC to determine the expected percentage of particles remaining at that energy after Beamsstrahlung effects. At the 6TeV centre-of-mass energy proposed for the indirect searches for the  $Z'$  only 10% of the particles per bunch remain at 3TeV for the collision. Consequently, for 6TeV collisions the collider is  $\approx 1\%$  efficient. For further information on such simulations see section 4.6.3.

The maximum  $Z'$  mass for which the existence of the  $Z'$  is inferred is that at which the error on the  $\gamma/Z/Z'$  interference cross section,  $E(\sigma_{Z'})$ , is smaller than the difference between the SM and the  $\gamma/Z/Z'$  interference cross sections,  $\Delta\sigma$ , in Figure 3.5. The number of events produced from a collider is given by the equation

$$N = Lt\epsilon\sigma \quad (3.5)$$

where  $L$  is the instantaneous luminosity,  $t$  is the run time,  $\epsilon$  is the efficiency and  $\sigma$  is the cross section [38]. For the 6TeV investigations at LEPIC, the instantaneous luminosity is  $1.98 \times 10^{35} \text{ cm}^{-2} \text{ s}^{-1}$  which operates for a total of 9 months. Taking into account the efficiencies of 1% for the beam,  $\epsilon_b$ , and 90% for the muon detector,  $\epsilon_\mu$ , the number of events has been determined for each  $\gamma/Z/Z'$  interference cross section using equation 3.5. Assuming that the standard deviation in the number of events is given by  $\sqrt{N}$  according to Poisson statistics, the error on the  $\gamma/Z/Z'$  interference cross section is given by the equation

$$E(\sigma_{Z'}) = \frac{\sqrt{N}}{Lt\epsilon} \quad (3.6)$$

which has been derived from the general error formula [39]. The maximum  $Z'$  mass limit has been determined from the point at which the quantity  $\Delta\sigma - E(\sigma_{Z'})$  switches from being positive to negative. The values determined from this analysis of the simulation data obtained are shown in Table 3.2.

Table 3.2:  $Z'$  mass limit analysis for the LEPIC collider investigations at 6TeV

$Z'$ Mass (TeV)	$\sigma(Z')$ (fb)	$\sigma(SM)$ (fb)	$\Delta\sigma$ (fb)	$N(\Delta\sigma)$	$N$	Err(N)	Err( $\sigma(Z')$ ) (fb)	$\Delta\sigma - \text{Err}(\sigma(Z'))$ (fb)
7.3	2.960	2.949	-0.011	-0.470	124.773	11.170	0.265	-0.276
7.4	2.851	2.949	0.098	4.133	120.170	10.962	0.260	-0.162
7.5	2.772	2.949	0.178	7.485	116.817	10.808	0.256	-0.079
7.6	2.713	2.949	0.236	9.941	114.361	10.694	0.254	-0.018
7.7	2.671	2.949	0.278	11.733	112.569	10.610	0.252	0.027
7.8	2.640	2.949	0.309	13.042	111.261	10.548	0.250	0.059
7.9	2.618	2.949	0.332	13.973	110.329	10.504	0.249	0.082
8.0	2.599	2.949	0.350	14.758	109.545	10.466	0.248	0.102
9.0	2.602	2.949	0.347	14.622	109.680	10.473	0.248	0.098
10.0	2.656	2.949	0.293	12.345	111.957	10.581	0.251	0.042
11.0	2.709	2.949	0.240	10.131	114.172	10.685	0.254	-0.013
12.0	2.749	2.949	0.200	8.432	115.870	10.764	0.255	-0.055
13.0	2.781	2.949	0.168	7.081	117.222	10.827	0.257	-0.089
14.0	2.806	2.949	0.143	6.042	118.261	10.875	0.258	-0.115
15.0	2.826	2.949	0.123	5.205	119.097	10.913	0.259	-0.135
20.0	2.882	2.949	0.067	2.829	121.474	11.022	0.261	-0.194
25.0	2.907	2.949	0.042	1.782	122.521	11.069	0.263	-0.220
30.0	2.920	2.949	0.029	1.224	123.079	11.094	0.263	-0.234
35.0	2.928	2.949	0.021	0.892	123.410	11.109	0.264	-0.242
40.0	2.933	2.949	0.016	0.678	123.624	11.119	0.264	-0.248
45.0	2.936	2.949	0.013	0.537	123.766	11.125	0.264	-0.251
50.0	2.939	2.949	0.010	0.427	123.875	11.130	0.264	-0.254

From the cross sections shown in Figure 3.5, the maximum  $Z'$  mass limit at which LEPIC can infer the existence of the  $Z'$  has been determined to be 10TeV. Beyond this limit, the error on the cross section becomes larger than the difference between the SM and  $\gamma/Z/Z'$  interference cross sections so existence cannot be inferred. This limit is additionally labelled in yellow in Table 3.2.

### 3.3.5 Ramifications for the Detector *written by John Cotterill*

The investigations into direct and indirect searches provide a few ramifications for the detector systems.

- 1) The potential for the production of a real  $Z'$  up to a mass of 6TeV permits a decay to two 3TeV particles of the form of muons or quarks. This therefore requires the muon detector and HCAL to be able to detect 3TeV muons and jets respectively. Reconstruction of the invariant mass of the  $Z'$  may then be possible.
- 2) For the indirect  $Z'$  investigations it is favourable for the luminosity and the run time to be maximised. This reduces the percentage error on  $N$  and consequently the error on the cross section. With these smaller errors, the higher mass region on Figure 3.5 can be probed. Alternatively, the efficiency of the beams operating at 6TeV could be improved which would have a similar effect. For example, improving the beam efficiency to 50% whilst maintaining the same instantaneous luminosity and run time would increase the potential  $Z'$  mass limit to 25TeV.

## 3.4 Supersymmetric Extensions of the Standard Model

### 3.4.1 Model Summary *written by Christopher Francis and Adrian Cross*

Supersymmetry predicts a partner to every known SM particle which differs by 1/2 in spin, i.e. a bosonic partner for every fermion and vice versa, and is widely considered to be the most attractive extension the standard model. There are several models which all fall under the broad term of supersymmetry, for this report we will be focusing on just two, the Minimally Supersymmetric Standard Model (MSSM) and the Next to Minimally Supersymmetric Standard Model (NMSSM). The particle content of the MSSM is shown in Figure 3.6. Additionally the NMSSM predicts two more Higgs particles and an extra neutralino that the MSSM does not contain. It is also important to note that the MSSM assumes R-parity conserving where all standard model particles are assigned an R-parity value of +1 and any supersymmetric particle is considered to have an R-parity value of -1. Whilst this R-parity is being conserved the lightest supersymmetric particle (LSP) cannot decay, as this particle is a neutralino it is also electrically neutral, somewhat massive and only weakly interacting all properties which make it an attractive candidate for dark matter.

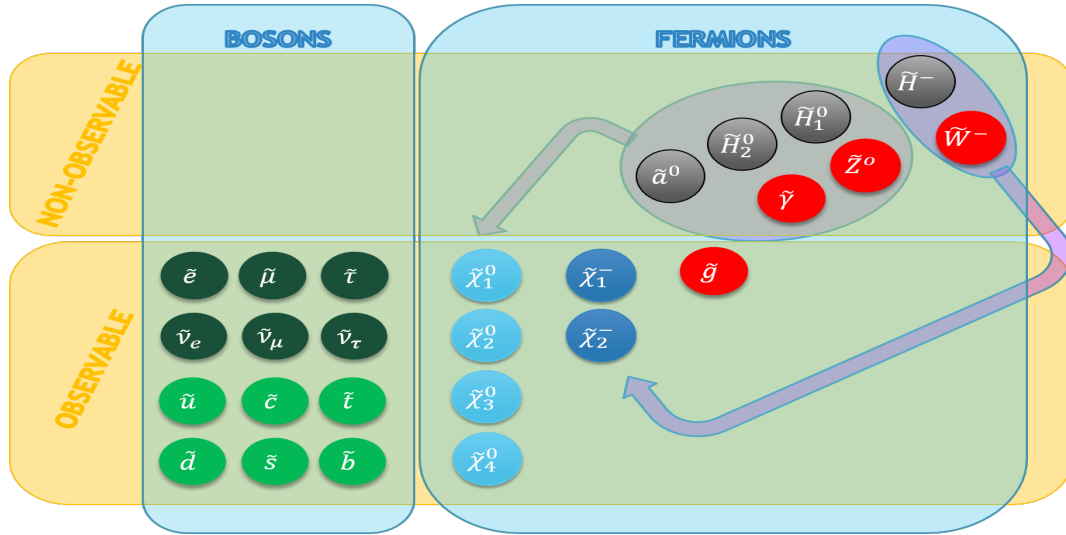


Figure 3.6: Diagram to illustrate the particle content of Supersymmetry *designed by Dwayne Spiteri*

The MSSM is the lowest energy supersymmetric model and is constrained to have only five free parameters which affect the predicted mass of the particles produced with the most common supersymmetrical breaking mechanism being gravity mediated, or mSUGRA for short. Other mechanisms include minimal gauge mediated susy breaking (mGSMB), anomaly mediated susy breaking (AMSB) and phenomenological MSSM. Each of these mechanisms affect which free parameters are altered as well as the number of free parameters. The model which has been concentrated is mSUGRA, the free parameters for the model are shown below [69].

Each of these parameters can be altered to change the particle masses to agree with experimental results. These parameters need to be altered so that the higgs mass predicted agrees with the mass as found by the LHC, which is  $\approx 125\text{GeV}$ .

### 3.4.2 Motivations *written by Daniel Hatton*

Supersymmetry was not initially introduced to solve problems with the theoretical basis of the standard model, which is often cited as its primary motivation. It arose in heavily mathematical studies of quantum field theory and its possible symmetries and in early versions of string theory, where it remains important [40]. The main motivations for the introduction of SUSY from a more modern viewpoint are, however, based on solutions to problems with extending the Standard Model.

One of these problems is intimately linked to the concept of symmetries. This is the hierarchy problem. The

statement of this problem most relevant to SUSY is that in order to achieve a Higgs mass considerably lower than the Planck mass (as is observed) very precise cancellations between certain parameters need to occur [41]. The light Higgs mass is unnatural in a specific sense; the small mass of a particle is natural if there is an approximate symmetry of the theory that is enhanced as the mass goes to zero [41, 42, 43]. For example, if the electron mass is zero then the electron field becomes invariant under a certain phase transformation [41]. No such approximate symmetry in the Standard Model can serve this purpose for scalar particles such as the Higgs [40]. However, the introduction of a boson for every fermion in the theory and vice versa leads to a consequence that would lower the Higgs mass. Quantum corrections from fermion or gauge boson loop diagrams to the Higgs mass can be calculated. The resulting integrals are divergent and must be renormalised so that the measured Higgs mass at a given energy scale is as observed. This involves adjusting parameters to achieve a cancellation of terms leaving the observed Higgs mass as required. If the corrections are too large then the cancellation involves more fine-tuning [41].

The Standard Model fermions alone do not cause a large fine-tuning problem. The problem is worsened considerably by the proposed particle content of Standard Model extensions such as Grand Unified Theories (GUTs) which include heavy particles. Supersymmetry, in an unbroken form, effectively eliminates the problem as the contributions from boson and fermion loops carry opposite signs. Therefore, exact supersymmetry (where the masses of each particle and its SUSY partner are equal) provides a natural cancellation [41]. Supersymmetry is not observed in an exact form so it must be broken. However, it will still elevate the hierarchy problem in this scenario. Another motivation for supersymmetry also relates to GUTs. In the Standard Model the renormalisation group equations, that determine the running of coupling constants, do not lead to a unification of these couplings at a single energy. Supersymmetry would provide corrections to the renormalisation group equations that could cause such a unification [44].

The above arguments indicate that if the parameters of a supersymmetric theory have to be finely-tuned to avoid disagreement with experiment then that theory would significantly lose impetus as one fine-tuning problem would have been replaced with another. Hence, in the light of recent LHC results [45, 46], the need to consider the NMSSM in the analysis for this project.

### 3.4.3 Benchmarking

#### 3.4.3.1 MSSM written by Adrian Cross

MSSM is the lowest energy supersymmetric model and which has been proposed in order to solve several problems with the standard model, such as antimatter-matter asymmetry. The most common supersymmetrical breaking mechanism is gravity mediated, or mSUGRA for short. Other mechanisms include minimal gauge mediated susy breaking (mGSMB), anomaly mediated susy breaking (AMSB) and phenomenological MSSM. Each of these mechanisms affect which parameters are fixed or free as well as the number of free parameters which need to be inputted. The model which has been concentrated is mSUGRA, the free parameters for the model are shown in table 3.3 [69].

Table 3.3: Constrained MSSM parameters [69]

Parameter	Definition
$m_0$	The mass of sleptons, squarks and Higgs bosons at the unification scale
$m_{1/2}$	The mass of the gauginos and higgsinos at the unification scale
$A_0$	Common trilinear coupling
$\tan(\beta)$	The ratio of Higgs vacuum expectation values
$\text{sign}(\mu)$	The sign of the Higgs mixing parameter

Each of these parameters can be altered to change the particle masses to agree with experimental results. These parameters need to be altered so that the higgs mass predicted agrees with the mass as found by the LHC, which is  $\approx 125\text{GeV}$ . The program SOFTSUSY [73] has been used to calculate the masses of MSSM particles with a variety of inputs depending on the model used. The program inputs a SUSY Les Houches Accord (SLHA) file type which contains the inputs required to predict MSSM particle properties.

```

lesHouchesInput x
# Example input in SLHA format, and suitable for input to
# SOFTSUSY (v1.8 or higher): CMSSM10.1.1 input - see arXiv:1109.3859
Block MODSEL          # Select model
  1 1                 # sugra
Block SMINPUTS         # Standard Model inputs
  1 1.279340000e+02  # alpha^(-1) SM MSbar(MZ)
  2 1.166370000e-05  # G_Fermi
  3 1.172000000e-01  # alpha_s(MZ) SM MSbar
  4 9.118760000e+01  # MZ(pole)
  5 4.250000000e+00  # mb(nb) SM MSbar
  6 1.743000000e+02  # mtop(pole)
  7 1.777000000e+00  # mtau(pole)
Block MINPAR           # Input parameters
  1 1.250000000e+02  # m0
  2 5.000000000e+02  # m12
  3 1.000000000e+01  # tan beta at MZ, in DRbar scheme, Feynman gauge
  4 1.000000000e+00  # sign(mu)
  5 0.000000000e+00  # A0
Block SOFTSUSY          # Optional SOFTSUSY-specific parameters
  1 1.000000000e-03  # Numerical precision: suggested range 10^(-3...-6)
  2 0.000000000e+00  # Quark mixing parameter: see manual
  5 1.000000000e+00  # Include 2-loop scalar mass squared/trilinear RGEs

```

Figure 3.7: example SLHA input file

Figure 3.7 shows an example input file. The MODSEL section contains the options for the model used in the program. These include options such as MSSM or NMSSM, R-parity violation, CP violation, flavour violation and the SUSY breaking model used for the program, which is set to mSUGRA in Figure 3.7. The model options can be altered to see how the resulting masses are affected. The SMINPUTS section contains the standard model parameters which have remained unchanged, the MINPAR section contains the input parameters and the SOFTSUSY section contains other model options which can be varied. Figure 3.8 shows how the mass of the Higgs boson varies with  $\tan \beta$  while keeping the other parameters fixed.

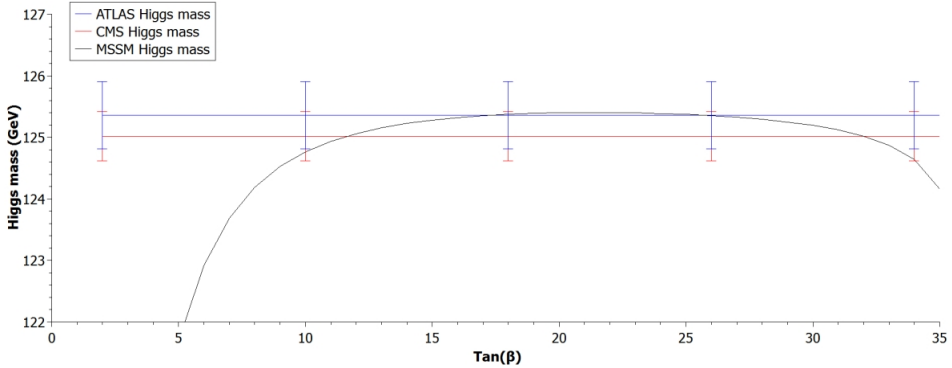


Figure 3.8: Predicted mass of the higgs particle with R-parity conservation,  $m_0 = 300\text{GeV}$ ,  $m_{1/2} = 2000\text{GeV}$ ,  $A_0 = -2000\text{GeV}$  and varying  $\tan \beta$ .[70] [71]

Figure 3.8 contains the mass of the Higgs as measured by the ATLAS and CMS detector[70] [71]. The Higgs mass outputted must lie close to the measured mass value. This puts constraints on the five input parameters. Other constraints can be put on the model from lower limits put on the third generation squark mass,  $\approx 1150\text{GeV}$ [72], and gluino mass,  $\approx 1450\text{GeV}$ [72], by the LHC. The  $A_0$  parameter has been varied in Figure 3.9.

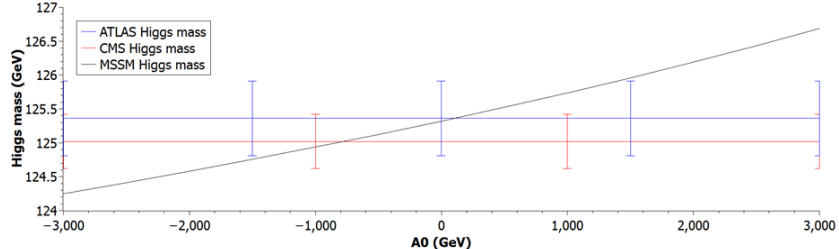


Figure 3.9: Predicted mass of the higgs particle with R-parity conservation,  $m_0 = 300\text{GeV}$ ,  $m_{1/2} = 2000\text{GeV}$ ,  $\tan \beta = 20$  and varying  $A_0$ [70] [71]

Figure 3.9 shows that each parameter varies the mass of the Higgs differently. The  $A_0$  parameter increases the Higgs mass as it increases in an approximately linear fashion.

The majority of the predicted benchmarks of the MSSM calculate a Higgs mass of around  $110\text{GeV}$ . This means that the values for the free parameters vary greatly in order to get a  $125\text{GeV}$  Higgs mass. In turn this causes the other particle masses to also greatly increase, making them more difficult to detect. Also, due to high energy measurements made at the LHC, the MSSM has been ruled out for lower mass squarks and gluinos, further constraining the model.

### 3.4.3.2 NMSSM *written by Daniel Hatton*

The calculation of the particle spectra of a theory given a minimum set of parameters, within the NMSSM, was performed using NMSSMTools [47, 48, 49, 50, 51]. All cases investigated here were within the unconstrained NMSSM and required 16 input parameters. NMSSMTools allowed grid scans of parameter space, varying several parameters between set limits with a given number of points, with points being eliminated on the basis of theoretical inconsistency (for example the appearance of tachyons) or the violation of in-built phenomenological constraints. The grid scan parameters used are shown in Table 3.4 ( $\lambda$ ,  $\kappa$  and  $\tan(\beta)$  were the parameters varied). Once a section of parameter space had been selected in this manner the varied parameters were chosen to give desirable benchmarks. A common requirement was that the lightest scalar Higgs of the theory should have a mass consistent with current experimental measurements. A further benefit of the use of NMSSMTools was that, through NMSDECAY [50, 51] the branching ratios of each particle's possible two body and three body decays was calculated and included in the output slha file. These decays could be read into Whizard [52, 53], greatly simplifying event simulation.

Table 3.4: NMSSMTools grid scan parameters

	Minimum value	Maximum value	Number of values
$\lambda$	0.01	0.9	50
$\kappa$	0.001	0.9	50
$\tan(\beta)$	2	20	20

Within the unconstrained NMSSM the squark and slepton masses can be adjusted at will by making changes to the relevant parameters (in this case the left and right stau masses  $m_{\tilde{\tau}_{L,R}}$  and the left and right stop masses  $m_{\tilde{t}_{L,R}}$  [54]). The neutralino and chargino masses could be adjusted by changing the up type and down type Higgs mass squared parameters but there was no parameter that determined an overall scale giving less flexibility. It was therefore difficult to obtain lightest neutralino masses above  $\sim 200\text{ GeV}$  and lightest chargino masses above  $\sim 300\text{ GeV}$  while producing the measured Higgs mass, within the NMSSM.

Ultimately three NMSSM benchmarks were produced. The benchmarks were determined primarily based on the requirements of slepton searches. Benchmarks were chosen to have selectron masses of approximately  $500\text{ GeV}$ ,  $1\text{ TeV}$  and  $1.5\text{ TeV}$  so selectron pair production could be achieved for all benchmarks at  $\sqrt{s} = 3\text{ TeV}$ . These benchmarks will be referred to as NMSSM01, NMSSM02 and NMSSM03 respectively. See Appendix A for more details.

### 3.4.4 Simulation Methodology *written by Dwayne Spiteri*

When the benchmark outputs from either SOFTSUSY or NMSSMTools, and the processes that contribute to the background are inputted into Whizard, it generates events. These events are run through detector simulation software called DELPHES. DELPHES uses the LEPIC detector to convert events into a root file that can be edited with a macro written in C++. It is this macro that can discriminate against events that do not fit a certain criteria in the final state and output histograms. Histograms for background with and without SUSY events are generated. If the resulting figure(s) have discernible differences then the simulated events should be able to be detected at LEPIC. It is important to note that all the simulations done in this section were conducted at an integrated luminosity of  $100\text{fb}^{-1}$  and were conducted with un-polarised beams. The polarisation of the initial  $e^+e^-$  beams leads to suppression of certain processes[174] but it's not guaranteed that this suppression only affects background processes.

### 3.4.5 Sparticles Phenomenology and Search Strategy

#### 3.4.5.1 Chargino and Neutralino Phenomenology *written by Thomas Dack*

The charginos are a pair of electrically charged fermions typically labelled as  $\tilde{\chi}_1^\pm$  and  $\tilde{\chi}_2^\pm$  with the second being the heaviest[77]. Both charginos can decay into a w boson and a neutralino whilst the heavier chargino can decay into a Z boson and the lighter chargino, such that:

$$\tilde{\chi}_1^\pm \Rightarrow \tilde{\chi}_1^0 + W^\pm \quad (3.7a)$$

$$\tilde{\chi}_2^\pm \Rightarrow \tilde{\chi}_2^0 + W^\pm \quad (3.7b)$$

$$\tilde{\chi}_2^\pm \Rightarrow \tilde{\chi}_2^\pm + Z^0 [75] \quad (3.7c)$$

Neutralinos are electrically neutral fermionic particles denoted by  $\tilde{\chi}_1^0, \dots, \tilde{\chi}_4^0$  [74]. The neutralinos are four eigenstates of the mass operator, due to the super-partners for the Z boson, photon and higgs (zino, photino and higgsino) having the same quantum numbers. The heavier neutralinos will typically decay via a Z boson into a lighter neutralino or via W boson into a chargino respectively. The lightest is stable in most supersymmetric models, which often takes the role of the lightest supersymmetric particle (LSP) though other particles may take this role.

In an  $e^+e^-$  collider neutralino-only final states can be produced directly through pair production or through the decay of heavier supersymmetric particles. A pair production processes to produce the lightest and next-to lightest (NLN) neutralinos can happen such that

$$e^+e^- = \tilde{\chi}_1^0\tilde{\chi}_2^0. \quad (3.8)$$

This decay process produces a particular associated signature, where the  $\tilde{\chi}_1^0$  leaves the detector undetected, whilst products from the decaying  $\tilde{\chi}_2^0$  will show the unbalanced momentum for the missing particle [76]. Similar processes can happen with  $\tilde{\chi}_3^0$  or  $\tilde{\chi}_4^0$  instead of the  $\tilde{\chi}_2^0$  particle. The decay into a pair of  $\tilde{\chi}_1^0$  neutralinos is often not investigated, as this appears solely as missing momentum in the detector and therefore is indistinguishable from the  $e^+e^- = \bar{\nu}_e\nu_e$  background. In R-parity conserving decay systems, all supersymmetric particles will eventually decay down into the LSP neutralino through their own decay mechanisms, giving a neutralino final state.

#### 3.4.5.2 Potential for Chargino Searches *written by Daniel Hatton*

Charginos can be directly produced in the process  $e^+e^- \rightarrow \tilde{\chi}_m^+\tilde{\chi}_\ell^-$  where  $m$  and  $\ell$  can be either 1 or 2. The allowed decays then depend on the mass hierarchy of the particles in the theory. In the NMSSM benchmarks used the only available decay for the lightest charginos was  $\tilde{\chi}_1^\pm \rightarrow \tilde{\chi}_1^0W^\pm$ . Direct  $W^\pm$  production obviously provides a large background for this process and production of two neutrinos and a  $W^+W^-$  pair also provides a background in some important situations, to be discussed later. In an ideal detector the missing energy present in the chargino decays would differentiate the two events but there are several sources of missing transverse energy in a realistic detector. For example, high energy jets close to the beam line may escape the detector leading to a missing energy signal. To eliminate the majority of this background the detectors will need high  $\eta$  coverage, although this should not be particularly difficult to achieve.

The main background remains  $W^+W^-$  production. The key difference between the chargino decay and  $W^+W^-$  production is the energy of the final products. In the case of direct  $W^+W^-$  production, if the Ws are assumed to be produced symmetrically, then each W will carry  $\sim 500\text{ GeV}$  (for  $\sqrt{s} = 1\text{ TeV}$ ), and once the W decays to two jets, the most energetic jet should carry a minimum of  $\sim 250\text{ GeV}$ . Ws resulting from chargino decay should have less energy as the  $\sim 200\text{ GeV}$  mass neutralinos will carry a significant amount of energy. Chargino decays should therefore appear as an excess of events with missing transverse energy and highest energy jets with momenta  $\lesssim 225\text{ GeV}$ . There is, however, another background that is more significant when the jet energy is restricted in this way. This is the process  $e^+e^- \rightarrow \nu\bar{\nu}W^+W^-$ , and possibly also  $\nu\bar{\nu}ZZ$  production. In all simulations the neutrinos were taken to be electron neutrinos as the cross section is higher than for other flavours. The neutrinos produced can carry significant amounts of energy, as the neutralinos do, which therefore lowers the W and Z energies. These neutrinos would then appear as missing energy further obscuring the neutralino signal. At 1 TeV the neutrinos do not carry as large a fraction of the energy as neutralinos and the jet momentum cut-off is sufficient for the observation of a signal; see Figure 3.10. Even if this were not the case, at this energy using the NMSSM01 benchmark, the

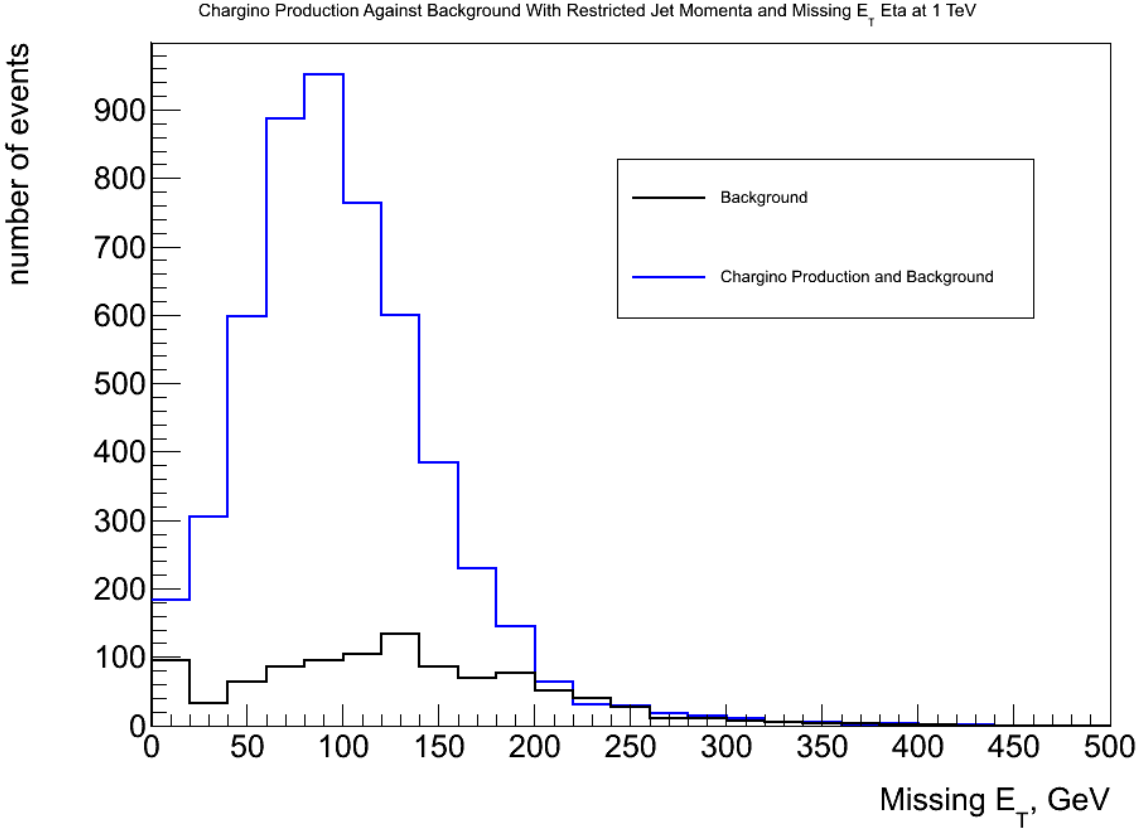


Figure 3.10: Plot of event number against missing  $E_T$  with higher energy jets of momentum  $< 225 \text{ GeV}$  using the NMSSM01 benchmark with  $\sqrt{s} = 1 \text{ TeV}$  and integrated luminosity  $100 \text{ fb}^{-1}$ . The result for  $e^+e^- \rightarrow W^+W^-$  and  $e^+e^- \rightarrow \nu_e\bar{\nu}_e W^+W^-$  background (black) is shown with the result for the background and  $e^+e^- \rightarrow \chi_1^+\chi_1^-$  (blue).

chargino production cross section is  $109 \text{ fb}$  and the double neutrino and W pair background cross section is only  $20 \text{ fb}$ . However, the chargino production cross section decreases substantially to  $13 \text{ fb}$  at  $3 \text{ TeV}$  while the neutrino background increases to  $123 \text{ fb}$ . At this energy the neutrinos also carry a higher fraction of the energy and the jet momentum cut-off fails to produce a signal.

The situation worsens when considering heavier charginos. The chargino masses in the NMSSM benchmarks used throughout this project were approximately a relatively low  $296 \text{ GeV}$ . This still comfortably complies with the current lower limit of  $94 \text{ GeV}$  [55], but higher energy LHC runs may extend this limit significantly. It is therefore advisable to conduct the above analysis for heavier charginos. This also has the benefit of examining the validity of the above analysis beyond a specific region of the NMSSM parameter space. The MSSM01 benchmark has considerably heavier charginos and was therefore used for this purpose. The mass of the charginos in this benchmark required a  $\sqrt{s}$  greater than  $3 \text{ TeV}$ . A  $6 \text{ TeV}$  collision was used in the simulations as this is the highest planned centre of mass energy of the collider. Due to the higher centre of mass energy the jet energy cut-off needed to be changed accordingly to  $\lesssim 1.4 \text{ TeV}$ . The higher mass neutralinos lead to a higher missing transverse energy than in the NMSSM01 case. This high missing energy signal can be seen against a pure  $W^+W^-$  production background. However, the signal is completely dominated if the  $\nu\bar{\nu}W^+W^-$  background is included. At this high energy the neutrino process has both high missing transverse energy from the neutrinos and an overwhelming cross section of  $276 \text{ fb}$  compared to  $3.2 \text{ fb}$  for chargino production. This shows that the analysis performed at  $1 \text{ TeV}$  is not sufficient at higher energies which significantly restricts the mass range of charginos that can be studied in this way to below  $500 \text{ GeV}$  if the only available decay mode is  $\tilde{\chi}_1^\pm \rightarrow W^\pm \tilde{\chi}_1^0$ .

However, at  $3 \text{ TeV}$  the possibility of polarisation of the beams could allow sufficient suppression of the background for signals to be observed. If the electrons are taken to be 80% right polarised and the positrons 60% left polarised

then the  $\nu\bar{\nu}W^+W^-$  cross section is reduced to 9.8 fb. The chargino production cross section is also reduced to 7.4 fb but this is now comparable to the background and so could be seen with high enough luminosity. While, in this benchmark, 100  $fb^{-1}$  should be sufficient for a  $5\sigma$  signal, Whizard simulations indicate that the cross section for production decreases with increasing chargino mass. If this trend continues to higher masses then higher integrated luminosity may be required. If the same polarisation is used for the 6 TeV MSSM case then the cross sections are 0.26 fb and 21 fb for the chargino production and  $\nu\bar{\nu}W^+W^-$  processes respectively. It therefore seems that charginos heavier than 1.5 TeV would still evade detection.

The above analysis requires the detectors to distinguish between 225 GeV and 300 GeV jets. This provides a requirement for the energy resolution of the hadronic calorimeter. This energy resolution would need to be realised in the end caps, as well as the barrel, because many high energy jets will be produced which will have high values of pseudorapidity  $\eta$ .

#### 3.4.5.3 Slepton Phenomenology *written by Dwayne Spiteri*

Conjugate slepton pairs will be produced at the interaction point. S leptons, because they only interact electroweakly, are expected to be more easily seen at  $e^+e^-$  colliders than proton colliders. The gluon strong interactions reduce the production cross section of sleptons and hence an  $e^+e^-$  collider is better suited to their detection[80]. This section will only focus on the detection of the lightest slepton, the selectron.

The two most dominant R-parity conserving slepton decays are:

$$\tilde{e}^\pm \rightarrow e^\pm + \tilde{\chi}_l^0 \text{ and } \tilde{e}^\pm \rightarrow \nu_e (\bar{\nu}_e) + \tilde{\chi}_k^\pm [80]$$

where l and k, represented as (l - k), are: (1,2,3,4 - 1,2) for MSSM, and (1,2,3,4,5 - 1,2) for NMSSM, assuming that the benchmarks used kinematically allow these decays.

By considering the successive decays of the neutralino and the chargino, it can be shown that a large proportion of selectron events ( $\gtrsim 50\%$ ) will have a lepton and some missing energy in their final state. This would serve as the selectron signature in the detector in the absence of background processes. The background of events are standard model events that give the same signature. These were taken to be  $e^+e^- \rightarrow W^+W^-$ ,  $Z_0Z_0$ ,  $HZ_0$ ,  $e^+e^-H$ ,  $\nu\bar{\nu}W^+W^-$ , and  $\nu\bar{\nu}Z_0Z_0$ . In the standard model, if a lepton is produced in the final state, it tends to be of a higher energy because it gets produced alongside a particle of similar or much smaller mass. Contrastingly, in the SUSY models, they get produced alongside much heavier particles and thus have lower energies. To allow for further distinction between sleptonic events and the background, a restriction on the energy of the final state electrons is imposed.

#### 3.4.5.4 Potential for Slepton Searches

The three benchmarks NMSSMTools produced (NMSSM01, NMSSM02, NMSSM03) respectively outputted three different selectron masses: 501GeV, 1TeV and 1.47TeV as quoted in section 3.4.3. SOFTSUSY's benchmark produces 1.35TeV selectrons. To reduce the background it is important to operate at energies close to double the selectron mass, hence all of these selectrons will be simulated through a  $\sqrt{S}$  of 3TeV rather than the maximum energy of the collider, 6TeV.

When Whizard was run using the MSSM benchmark, events could not be simulated because the partial width of the selectron was too small. This is possibly due to the reduction in the number of possible decays. The only chargino or neutralino that the selectron was heavier than in this benchmark was the LSP;  $\tilde{\chi}_1^0$ . Since the partial width of a particle is inversely proportional to its lifetime, it can be assumed that under this benchmark, the selectron would not decay in the detector.

The particles subsequent behaviour in the detector is determined by its gamma factor, which extends its lab-frame lifetime, and its beta. The product of the two is a factor in the Bethe-Bloch formula for ionisation energy loss[81].

In the MSSM benchmark, the selectrons produced will have a maximum  $\gamma$  of 1.10  $\left(\frac{E_{\tilde{e}}}{m_{\tilde{e}}}\right)$  and a  $\beta$  of 0.416

$\left(\sqrt{1 - \gamma^{-2}}\right)$ . Since the product of these values is less than 1, then the selectrons are in the region of high ionisation losses proportional to  $\frac{1}{\beta^2}$ [81]. The estimated ionisation energy loss (IEL) per unit length for these selectrons is therefore roughly  $5.77 \text{ MeVg}^{-1} \text{ cm}^2$ . To get the minimum total energy loss in the collider, the IEL is multiplied by the density of detector segment and it's the radial length summed over all the main detector constituents. The presence of a magnetic field curves the path of the particle and increases the distance at which it travels through the detector. For simplicity this can be ignored. For sleptons of this benchmark in the LEPIC detector, the total minimum IEL is equal to 20.62GeV (see Appendix B). Since the IEL for the entire detector is less than  $E_{\tilde{e}}$ , the most probable outcome for MSSM sleptons of this benchmark is to deposit some energy in all the main detectors and not be fully absorbed, similar to the trace left behind by a muon. The way to tell the difference in this case is to measure the radius of curvature of the particles once they have travelled through the detector. Since muons are about  $13000\times$  lighter than these selectrons and are travelling about twice as fast, the radius of curvature for selectrons are going to be much larger than those for the muon.

For the three NMSSM benchmarks, events are able to be simulated in Whizard. The C++ macro used to discriminate the output discards all events that have do not have at least one lepton, some missing energy and have leptons with momenta larger than 400GeV in the final state. The momentum discrimination was determined by running the NMSSM01 benchmark several times editing only the required lepton momentum. If it was too low, then all the events were cut and process and background were of the same order, and if it was too high, then the high energy leptonic background became more prevalent. A 400GeV momentum cut-off gave the best event separation from the background for the NMSSM01 benchmark and was used as the discrimination level for all benchmarks. The histograms plot the number of events that have missing transverse energy,  $E_T$  against the  $E_T$ . The missing  $E_T$  in the events comes from the lack of detection of any neutralino produced. The peak at around 25GeV represents missing transverse energy from neutrinos. Figures 3.11, 3.12 and 3.13 show these plots.

Figure 3.11: Data of number of events with missing  $E_T$  against the energy of that missing  $E_T$  and a 400GeV electron momentum cut-off for 501GeV selectron benchmark.

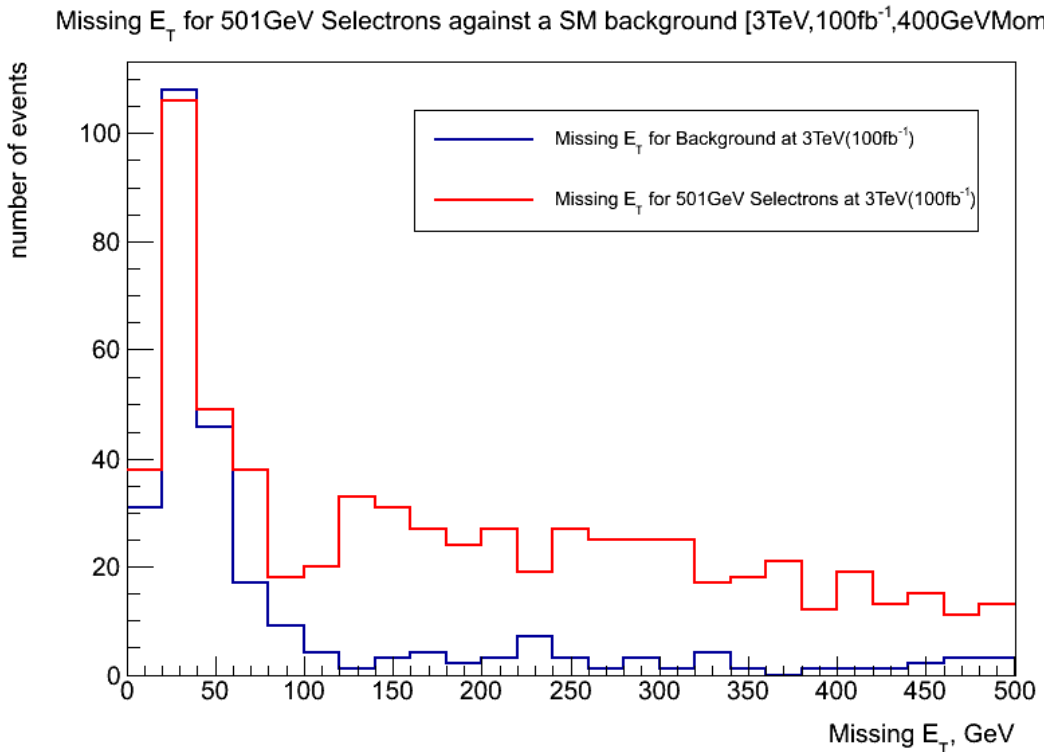


Figure 3.12: Data of number of events with missing  $E_T$  against the energy of that missing  $E_T$  and a 400GeV electron momentum cut-off for 1TeV selectron benchmark.

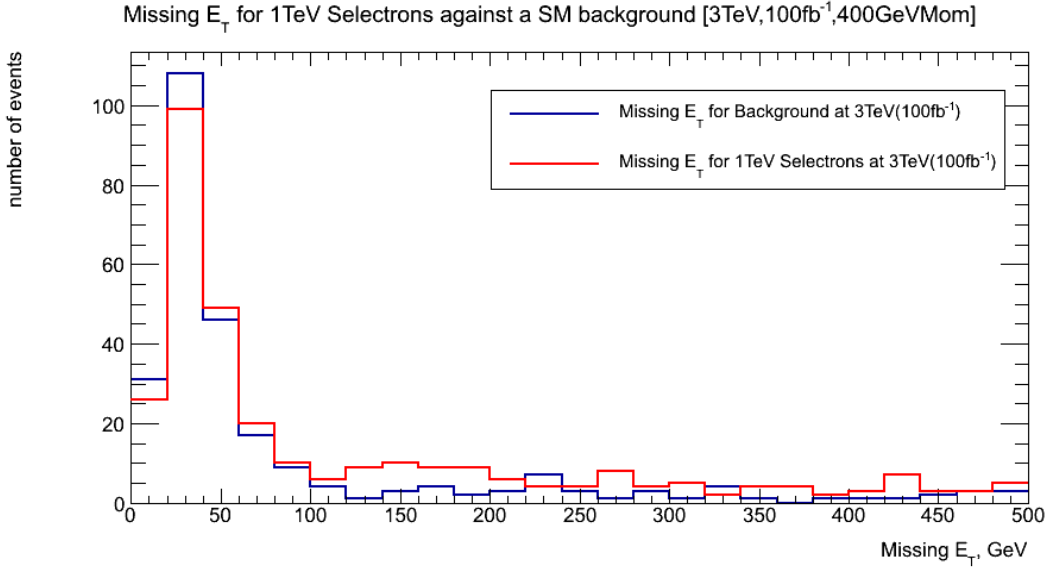
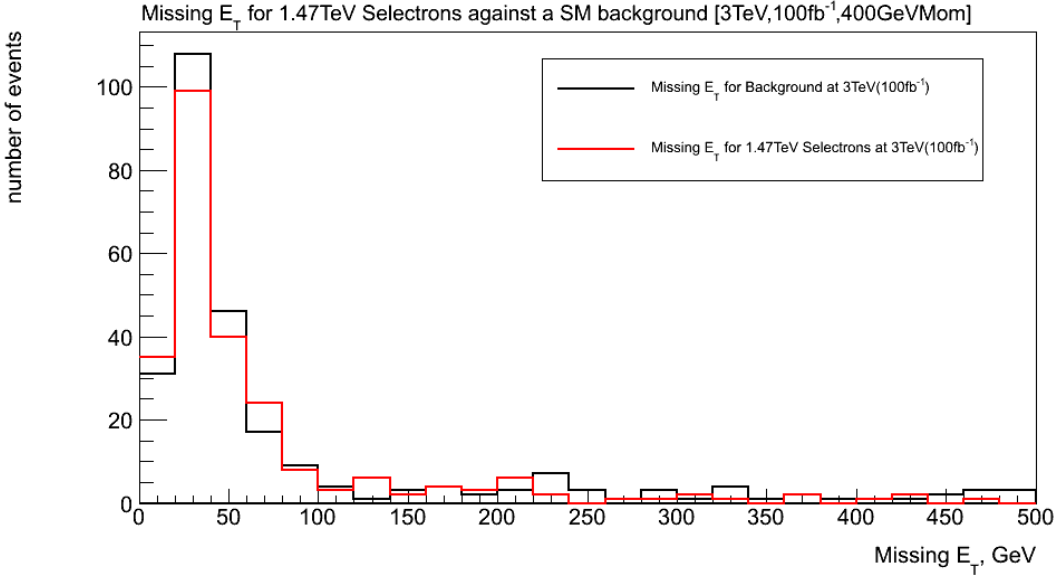


Figure 3.13: Data of number of events with missing  $E_T$  against the energy of that missing  $E_T$  and a 400GeV electron momentum cut-off for 1.47TeV selectron benchmark.



Figures 3.11, 3.12 and 3.13 show that the integrated area between the events and the background decreases with larger selectron mass. This is expected as the cross section of production for the events decreases with increasing mass of the selectron in this benchmark. This has been run with  $100\text{fb}^{-1}$  of data so given the proposed luminosity and remaining run time after the Higgs run of the collider has been complete, it would be expected that there would be an increase in the amount of counts in both processes, and higher statistical significance in their difference for all three benchmarks.

It can be concluded that the LEPIC detector is most sensitive to the lighter sleptons in NMSSM. The larger the luminosity of the collider, the more significant the height above the background is. For our detector to be able to pick up 500GeV and 1TeV selectrons nothing extra is really required off of the detector. A high integrated luminosity would be beneficial for the detection of 1TeV selectrons. It seems that it may nor be possible to resolve

a 1.47TeV selectron event in this detector.

### 3.4.5.5 Higgs Phenomenology written by Lucy Bignell

With the exception of the standard model-like Higgs,  $H_1^0$ , and the lightest pseudoscalar Higgs,  $a_1^0$ , the production cross sections for most NMSSM Higgs particles are intolerably low, according to the NMSSM02 benchmark used. For this reason, particle simulations for the NMSSM Higgs sector were limited to a thorough investigation of the production and decay of  $a_1^0$ . The most promising process for production of this Higgs particle is via neutralino decay as shown in Figure 3.14 below. In particular, the NMSSM02 benchmark predicts a branching fraction of 0.468 for  $\tilde{\chi}_3^0 \rightarrow \tilde{\chi}_1^0 a_1^0$ . The slightly more dominant decay mode, with a branching fraction of 0.523, is  $\tilde{\chi}_3^0 \rightarrow \tilde{\chi}_1^0 Z^0$ .

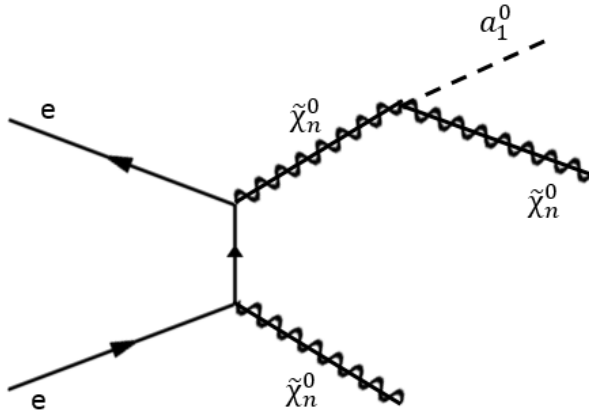


Figure 3.14: In a lepton collider neutralinos are produced which can subsequently decay into the lightest pseudoscalar Higgs and another neutralino of lower mass.

As a neutral particle,  $a_1^0$  decays into quark-antiquark or lepton-antilepton pairs. Namely  $s\bar{s}$ ,  $c\bar{c}$ ,  $b\bar{b}$ ,  $\mu\bar{\mu}$  and  $\tau\bar{\tau}$  pairs may be produced. This Higgs particle can also decay into neutral bosons such as gluons, photons and the Z boson. Of these decays, the highest branching fractions are predicted for  $a_1^0 \rightarrow \gamma\gamma$  and  $a_1^0 \rightarrow b\bar{b}$  using the NMSSM02 benchmark. These are 0.546 and 0.405 respectively. In addition to being the most probable decay, the  $\gamma\gamma$  final state decay also has much lower standard model background than for a di-jet final state. Thus it was initially used as the main search channel for the pseudoscalar Higgs. The background processes are Higgstrahlung,  $e^+e^- \rightarrow Z^0 H_1^0 \rightarrow Z^0 \gamma\gamma$ , and direct production of photons via electron-positron annihilation,  $e^+e^- \rightarrow \gamma\gamma$ . Unfortunately it was found that the simulation software, Whizard, does not support the  $a_1^0 \rightarrow \gamma\gamma$  decay as only background events were found in the output files.

An alternative option is to search for  $a_1^0 \rightarrow jets$  as, despite the larger background incurred, this process still has a relatively high branching ratio. This is due to the fact that the Higgs couples to mass and thus the bottom quark is more likely to be produced than the other, lighter final state particles. Despite  $a_1^0 \rightarrow b\bar{b}$  being one of the most probable decays, it will simply be observed as jets in the detector. Hence the standard model background processes include direct production of any quark-antiquark pair via electron-positron annihilation,  $e^+e^- \rightarrow q\bar{q}$ , and also the production of W and Z bosons with subsequent decay to quarks,  $e^+e^- \rightarrow W^+W^- \rightarrow q\bar{q}q\bar{q}$  and  $e^+e^- \rightarrow Z^0Z^0 \rightarrow q\bar{q}q\bar{q}$ . Moreover, the cross sections for such background events are relatively high which has an adverse effect on the observed signal-to-background ratio. These processes are shown explicitly in Figure 3.15 below, alongside the Feynman diagram for the Higgs decay to jets.

In order to simulate the Higgs decay to jets, the process and its corresponding background were written to a Whizard input file. The NMSSM02 benchmark file was also linked to this input file to provide information about particle masses and the branching ratios for various decay modes. The output from Whizard was then passed through Delphes in order to mimic smearing of the LEPIC detector, as detailed in section 3.4.4. Following this, a C++ macro was used to manipulate the data generated by Delphes to determine the invariant mass of all jets appearing within the detector. The macro builds a histogram of the number of jet events versus invariant mass of each event. In order to identify the background contributions, the process was simulated a second time with the  $e^+e^- \rightarrow \tilde{\chi}_n^0 \tilde{\chi}_m^0$  events, and thus the Higgs signal, removed from the Whizard input file.

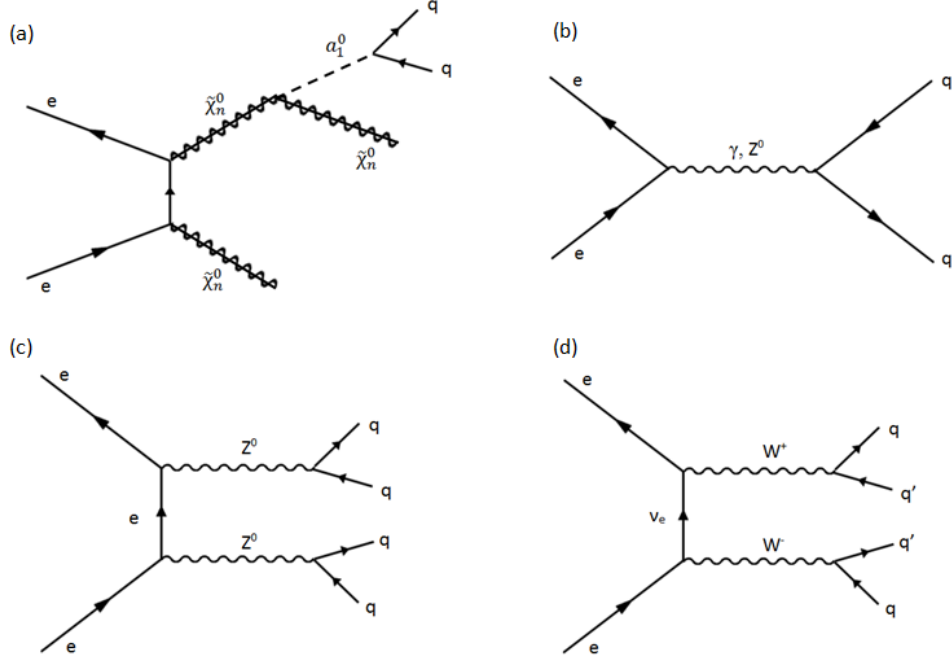


Figure 3.15: Feynman diagrams for the pseudoscalar Higgs decay to jets (a) and the corresponding standard model background processes. The background events are direct electron-positron annihilation to quark-antiquark pair (b),  $Z$  boson production (c) and charged  $W$  boson production (d).

### 3.4.5.6 Potential for Higgs Searches *written by Lucy Bignell*

The results of the particle simulations at a centre of mass energy of 3TeV and an integrated luminosity of  $100\text{fb}^{-1}$  are shown in Figures 3.16 and 3.17 below.

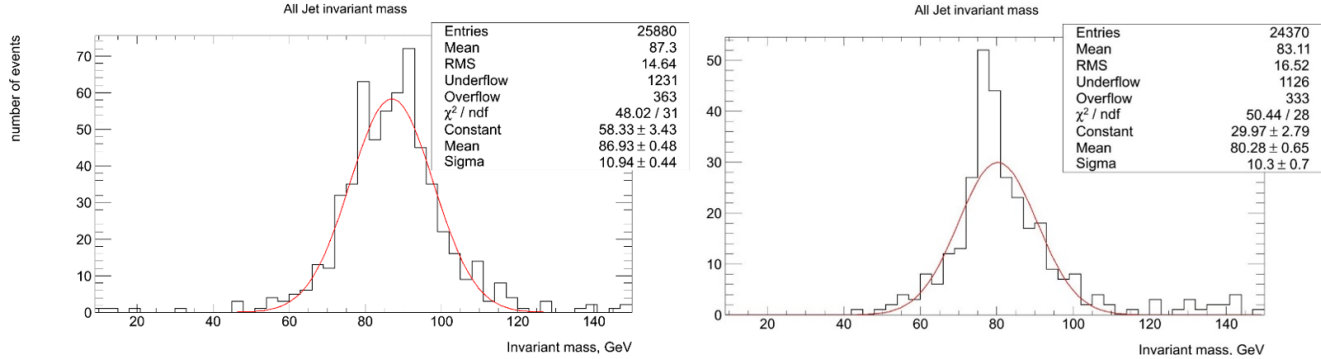


Figure 3.16: Fitted peaks of the number of jet events versus invariant mass of jet events in the detector (left). Showing only background contributions (right). Data acquired using the NMSSM02 benchmark with a centre of mass energy of 3TeV and an integrated luminosity of  $100\text{fb}^{-1}$ .

The mass of the lightest pseudoscalar Higgs is 99.86GeV according the NMSSM model in question. In comparison to the background, it appears that there is an enhancement in the number of events at this invariant mass. Using the NMSSM02 benchmark, the largest measured cross section for neutralino production, and therefore potential  $a_1^0$  production, was  $4.196 \pm 0.015\text{fb}$ . This is small in comparison to the cross sections for  $W$  and  $Z$  boson production. Such background events had measured cross sections of  $452.1 \pm 2.4\text{fb}$  and  $24.94 \pm 0.10\text{fb}$  respectively. In addition  $Z$  bosons are also produced with  $\approx 50\%$  probability via  $\tilde{\chi}_3^0 \rightarrow \tilde{\chi}_1^0 Z^0$ , as detailed in section 3.4.5.5. This justifies the shape of the histograms in terms of the drowning out of the 99.86GeV Higgs signal.

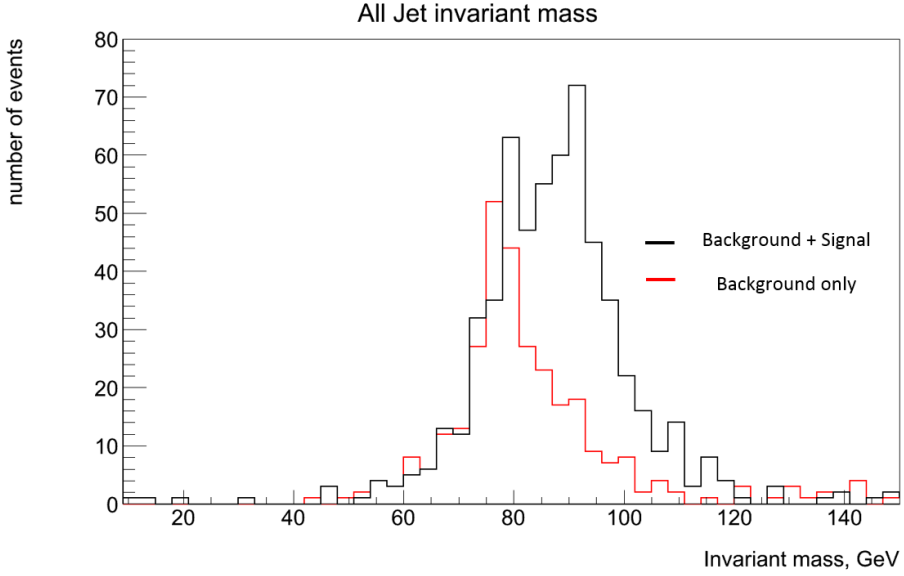


Figure 3.17: Showing the background contributions (red) overlaid on top of the total jet events (black) from Figure 3.16.

The fact that the pseudoscalar Higgs is more likely to decay to  $b\bar{b}$  than other quark-antiquark pairs also has an impact on what is observed in the detector compared with theoretical predictions. As a third generation quark, the bottom (or antibottom) quark has a short lifetime and is thus likely to decay before detection. Probable decay modes, such as  $b \rightarrow ce^-\bar{\nu}_e$ , have leptonic final states. These events are therefore not included in the jet reconstruction and will influence the recorded number of events at the expected invariant mass of  $a_1^0$ .

In terms of further research, the pseudoscalar Higgs signal may be enhanced further by searching for a different signature in the detector. As shown in Figure 3.14,  $a_1^0$  is produced in association with a neutralino and thus missing energy will be observed in the detector. In contrast to this, the standard model background events primarily consist of hadronic final states. Neutrinos may be produced in some cases, such as that shown for bottom quark decay above, but the majority of final state particles will interact in at least one component of the detector. As a result, analysis of the missing energy and momentum in the detector may provide additional, useful information about detection of the pseudoscalar Higgs particle.

In conclusion, based upon the jet reconstruction analysis, an important consequence for the hadronic calorimeter is that it must have a much greater resolution than 8.8GeV in order to distinguish the Higgs signal from background. Specifically this is the mass difference between the 99.86GeV pseudoscalar Higgs and the standard model Z boson which has a mass of  $91.1876 \pm 0.0021$ GeV [57].

#### 3.4.5.7 Squarks Phenomenology *written by Christopher Francis*

As Supersymmetry predicts a partner for every standard model fermion the squark sector is expected to made up of 12 particles, 6 sparticles and 6 anti-sparticles, it is not expected to be viable to search for each one within the time frame proposed and so the main focus will be detection of the stop squark for which a lower limit on the mass has already been found by CMS searches at the LHC with the stop squark being excluded up to 0.75TeV[82] thus a good place to start seems to be a centre of mass energy of 1TeV. Initially the stop squark was believed to have only one decay in the MSSM, induced by a loop flavour changing decay into the LSP and a charm quark,

$$\tilde{t}_1 \rightarrow c\chi_1^0 \quad (3.9)$$

Obviously as this was believed to be the only decay mode it had a 100% branching ratio which is only a valid assumption if the stop squark is the next lightest supersymmetric particle (NLSP). This is a difficult decay to detect however a charginos are not easily distinguished from other charged particles and a charm quark is not a

unique enough signature to suggest a stop squark. A more reliable decay mode seems to appear in the NMSSM, whilst there are several possible decay modes for the stop squark the most common would appear to be the decay into a bottom type quark and a heavy chargino, this chargino can then decay to the lightest neutralino through the emission of a W boson which can itself decay into either a pair of quarks or a lepton and neutrino pair, as shown in Figure 3.18.

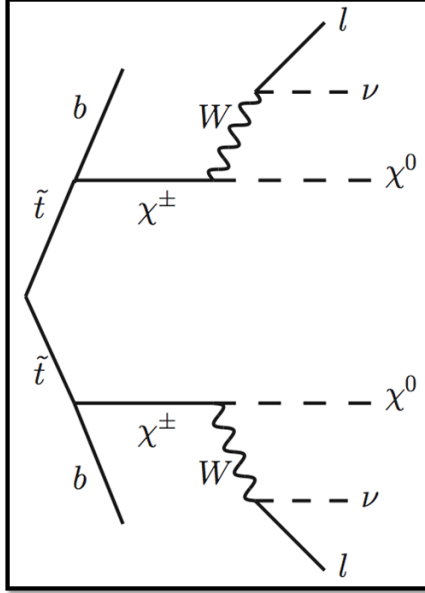


Figure 3.18: Feynman diagram describing stop squark decay

This leads to the background processes for a stop quark decay being any process that produces at least two jets and some portion of missing energy, which is many decays. There are some qualifying factors to this however mainly the fact that we would expect to see jets of a lower energy than those produced by a standard W boson, this is because the LSP is still considerably heavier than a neutrino and therefore would be expected to carry away a larger proportion of the energy in the decay. Branching ratios for each of the possible decays are shown in the slha file produced by NMSSMTools, for the particular decay we are looking for the branching ratio is shown to be 0.32616545, this is still not particularly high and so in order to find the stop signal a considerable amount of events will be required. There is also some theoretical basis that this decay could be mediated by a Higgs[83] which could lead to the process being further suppressed as the mass of the Higgs is greater than a W boson and the Higgs Yukawa coupling to fermions is suppressed by the respective fermion masses.

It is also possible for the stop to decay straight into a heavy neutralino and a top quark however the lifetime of the top quark is so low,  $5 \times 10^{-25}$  s, that it would almost immediately decay into a down type quark, 99% of the time this is a bottom quark, and a W boson so the end result which is being detected is the same. As the main aim here is simply to confirm the existence of the stop this is not too problematic however more detailed measurements, for example its mass, would require more detailed evaluation of its decay path.

Simulating this decay was done through use of whizard program where the input contained both the decay and its corresponding background, this also required use of the NMSSM01 benchmarks discussed earlier which provides details of the particles masses and branching ratios. The output file was then passed through Delphes using the detector card that had been created which would mimic detector smearing. Finally a C++ program was used to gather the data into a graphical representation, in this case a histogram was used. This process was repeated for the background processes only which can then be plotted on the same histogram and used for comparison to try and see a squark event.

### 3.4.5.8 Potential for Squark Searches

Unfortunately simulations of squark production have shown little in the way of viable results which is not unexpected due to the low cross section discussed earlier, however it is possible to say that the detector would require an fine

energy resolution in order to distinguish between the different energy jets. Figure 3.19 shows the histogram produced by one of the simulations run at 3TeV and  $100\text{fb}^{-1}$ . This shows that there is little in the way of statistical significance to be able to distinguish squark events from the inherent background as some peaks can be influenced by the smearing done by Delphes, which may give the impression that a squark event had occurred when that is most likely not the case.

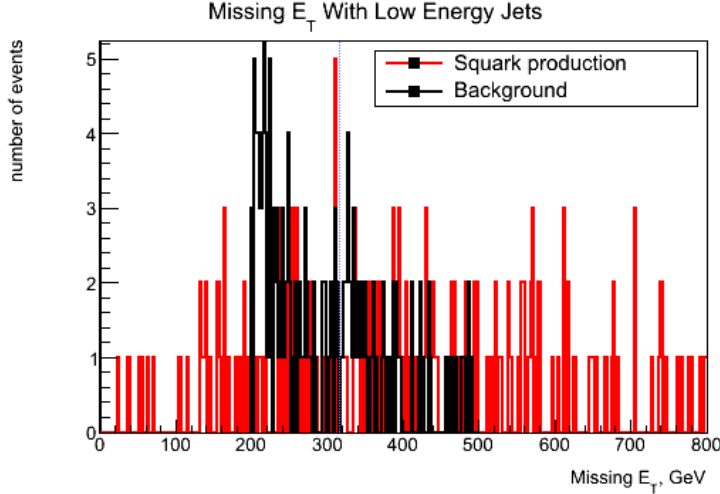


Figure 3.19: Results of a Delphes smearing simulation of Stop squark decay at 3TeV

Overall this result was not unexpected considering the cross section is so low and so finding the specific combination of decay products that could infer the stops existence is very unlikely. This is further compounded by the fact that the search was done purely for jets and it is possible to have leptonic final states from the W boson decay that would not be included in the event capture. Further research into squark production would be better suited to a collider such as the LHC which is specifically designed for a hadronic environment and more easily scan a variety of different energies.

### 3.5 Conclusion *written by Christopher Francis*

Searching for new physics beyond what is predicted by the standard model is not an easy endeavour and can indeed often be a case of trial and error experimentation as theory can only predict a general range in which new particles may be found. During this report we have covered a few of the problems with the standard model as well as brief descriptions of some possible solutions. A more in depth study of Supersymmetry and heavy neutral gauge bosons has been undertaken as these were deemed to be the most promising areas for a leptonic collider whilst also covering a wide range of physics.

Using Whizard and Delphes simulations were run to find these particles at a variety of different energies that the collider is capable of achieving, the various background processes were also investigated using this method in order to try and separate the two and confirm a more specific energy range to focus on. It has been shown that, within the benchmarks used, there is a possibility for both slepton and chargino production in the leptonic environment however Higgs and squark production seems much less promising. It is possible however that other hadronic colliders, LHC in particular, could still find evidence of these particles. It also seems likely that our collider will not reach sufficient energies to find conclusive evidence of Z primes as these could have masses up 50TeV or even more however a plan for detecting these particles has been developed along with the required detector specifications which could prove useful in the future as the technology to probe these massive energy scales is developed.

## 4 The Collider Design

### 4.1 Introduction *written by Lucy Bignell*

The collider has been designed according to the specifications outlined by the Higgs and New Particles sub-groups in sections 2.7, 3.3 and 3.4 above. In order to meet these requirements, an investigation into previous and proposed lepton colliders was conducted. This research was intended to explore the successes of other colliders and simultaneously unearth design flaws that could be avoided. The main conclusion drawn from this work was the substantial difference in machine parameters used by the SLAC Linear Collider (SLC) in the 1980-1990s and that set out by modern designs such as CLIC and ILC. Important design improvements include the bunch structure, beam dimensions and crossing angle at the interaction point. Future colliders propose to use pulses consisting of hundreds or thousands of bunches and cause them to collide at a small (mrad) crossing angle [92][93]. In comparison, single bunches were used at SLC and fired into a head on collision at the interaction point [94]. The horizontal and vertical beam sizes were also much larger at SLC than for that proposed by CLIC and ILC [94][95][96].

Of course, such advances in the collider design allow much higher collision energies to be reached without compromise elsewhere. For this reason, inspiration has been taken from this research in order to build a successful lepton collider. When finalising LEPIC machine parameters, this information on previous and proposed colliders has served as valuable reference material.

It was also found that, despite having seemingly similar design specifications, the technologies proposed by CLIC and ILC are very different. For example, whilst ILC intends to use 'traditional' RF accelerating cavities in order to achieve a 500GeV centre of mass energy, the CLIC design puts forward a novel two-beam acceleration scheme [92]. It is suggested that this method of acceleration will enable access to TeV scale collision energies whilst also maintaining a sufficient luminosity [92].

The remainder of this section details the collider design proposal for LEPIC with consideration of the aforementioned research and input from the Higgs and New Particles sub-groups. The layout of the collider along with analysis of energy losses and achievable luminosity shall be outlined. In addition, the most important machine components will be discussed in detail. These are the particle production mechanisms, the damping and storage rings, main linac focusing and acceleration, beam collimation, the machine-detector interface and beam dumps.

### 4.2 Circular vs. Linear Colliders *written by Lewis Simmons*

When considering any potential collider, one is faced with a decision to opt for a linear or circular design. In the field of electron-positron collisions the forerunner, LEP2, deployed a circular layout and was able to collide these particles at a interaction energy of  $\approx 209\text{GeV}$  in the final stages of operation. This system was conceived primarily as a "Z factory" and aimed to probe the properties of the newly discovered Z boson with higher precision than previous systems [102].

In current times we are faced with a similar dilemma, but at a higher energy scale. We have observed a new "Higgs-like" boson at the LHC, but still require significant experimentation to determine its properties. Here electron-positron collisions provide a much cleaner investigative tool than similar energy hadronic experiments. It is due to this that electron-positron systems are under consideration for new "Higgs factory" establishments. The lack of background hadronic processes with electron-positron collisions has inspired plans for several new colliders ranging in energy, size and layout [103].

The significant challenge when developing a circular electron-positron system is overcoming synchrotron radiation, SR, energy losses whilst beams are circulating. The relation for energy loss from this mechanism is shown below in equation 4.1. It is due to this process that a linear design is favoured for some potential future colliders with energies large enough to probe the couplings of the new Higgs particle as well as other, unexplored high energy physics.

$$\Delta E_{turn} = \frac{4\pi}{3} \frac{r_e}{m_e^3} \frac{E^4}{\rho} \quad (4.1)$$

$\Delta E_{turn}$	Energy radiated per turn in GeV
$r_e = 2.8179403267 \times 10^{-15} m$	Classical electron radius in metres [104]
$m_e = 0.00051099891 GeV$	Electron mass in GeV [104]
$E$	Energy of electrons in GeV
$\rho$	Effective bending radius in metres

The equation above is used to determine the energy loss per electron, per turn, in a circular collider. From this equation we can note that losses increase with the 4th power of energy, making higher energies significantly harder to maintain. We can also note that the loss decreases with particle mass to the inverse 4th power ( $r_e \propto m_e^{-1}$ ). As a result of this hadronic colliders radiate significantly less energy compared with electron-positron systems of similar design. To display this, we can find the ratio of proton mass to electron mass and then raise this value to the 4th power to see the difference in radiated energy if all other parameters are consistent between an  $e^+e^-$  and proton collider:

$$\frac{m_\rho}{m_e} = \frac{0.938272046 GeV}{0.00051099891 GeV} = 1836.153 \rightarrow (1836.153)^4 = 1.137 \times 10^{13} \quad (4.2)$$

This massive increase in synchrotron radiation losses between hadronic (e.g. LHC) and electron-positron systems means that it is impractical to use similar size rings and energies for both regimes. Instead lower beam energies and greater radii are chosen for circular  $e^+e^-$  colliders in an attempt to offset this huge factor. This presents several problems for any potential circular “Higgs factories”:

- A high enough energy must be achievable to probe Higgs properties, especially self-coupling. Theorised collider designs expect these parameters to be testable from approximately 300GeV (Higgs-strahlung) to 1TeV (WW fusion Higgs self-coupling) with electron-positron collisions [105].
- Increasing the radius decreases the synchrotron radiation losses linearly, this makes it near-impossible to offset the large 4th power increase in SR losses due to high energy. Since a significant cost of building any collider is the creation of the beam tunnel, large radii lead to vastly increasing costs, these soon become unrealistic.
- Once properties of the Higgs particle have been studied to greater depth, the collider should ideally be able to test other new physics such as exotic particles. This will require TeV scale energies which cause yet greater energy losses.

The easiest way to appreciate the challenges that synchrotron radiation causes is to compare a proposed system with those that have already been used. Table 4.1 below shows data for some other circular colliders and their corresponding energy losses per turn. Hypothetical systems with energies of interest are given in blue.

The hypothetical values in Table 4.1 demonstrate that lower energy circular Higgs factories are viable with comparable energy losses to older systems such as LEP2. This means that, in theory, the Higgs boson can be produced and experimented upon at facilities such as those proposed above. However having lower centre of mass energies limits the mechanisms by which the Higgs particles can interact. In particular the WW fusion process would be out of reach due to the maximised cross section at a few TeV. If a collider is expected to probe a multitude of Higgs couplings and production processes, the centre of mass energy must be increased to the order of TeV. By doing this the synchrotron losses escalate greatly and the feasibility of offsetting such losses comes into consideration.

In contrast to this drawback, circular systems do offer some significant advantages compared to their linear counterparts. For instance, beams can be recirculated in circular colliders so less refinement is required in positron production mechanisms. Circular colliders also offer the possibility of multiple, simultaneous interaction points. This significantly increases the amount of experimentation which can be achieved per unit of run time. Another advantage of circular layouts is a wealth of expertise and experience from the multitude of previous high energy physics experiments such as LEP, Tevatron and the LHC. This means that many subsystems and infrastructure can be quickly produced and integrated at a new facility. Looking beyond the lifetime of the collider, circular lepton

Table 4.1: A variety of circular colliders with their beam energy, radii and corresponding energy losses per turn

Facility	Particles Accelerated	Beam Energy	Radius (m)	$\Delta E_{turn}$
LEP	$e^+e^-$	45 GeV	3096	117 MeV
LEP 2	$e^+e^-$	104.5 GeV	3096	3.40 GeV
LHC	pp	4.0 TeV	2804	710 eV
LHC (Upgraded)	pp	7.0 TeV	2804	6.66 keV
LHC size 300 GeV collider	$e^+e^-$	150 GeV	2804	15.972 GeV
LHC size 3 TeV collider	$e^+e^-$	1.5 TeV	2804	$1.59720 \times 10^5$ GeV
100km circumference 300 GeV collider	$e^+e^-$	150 GeV	15915	2.814 GeV
100km circumference 3 TeV collider	$e^+e^-$	1.5 TeV	15915	$2.814 \times 10^4$ GeV
100km circumference 6 TeV collider	$e^+e^-$	3 TeV	15915	$4.502 \times 10^5$ GeV
CEPC	$e^+e^-$	120 GeV	6094	3.01 GeV
TLEP ( $t\bar{t}$ threshold)	ee	175 GeV	9000	9.219 GeV

colliders can be redesigned as hadron collider systems. This significantly cuts costs on tunnelling and infrastructure and these hadron machines can access massively higher energies [108].

Despite these advantages, synchrotron losses for such a high energy electron-positron collider are too large to warrant a circular design. It is due to this complication that the group have pursued a linear design. This will not be limited by synchrotron radiation losses as severely, and can theoretically operate more efficiently at TeV scale energies. This enables the Higgs particles produced to be analysed at a variety of different centre of mass energies corresponding to various production mechanisms. It also enables new, exotic physics to be searched for at energies higher than those achievable at current systems such as the LHC. [108].

### 4.3 The Collider Layout *written by Lucy Bignell*

According to the considerations of collider geometry outlined above, the layout of LEPIC shall be as shown in Figure 4.1. The total length of the collider shall be 150km, with each of the main linacs having a length of 72.9km as detailed in Section 4.10.

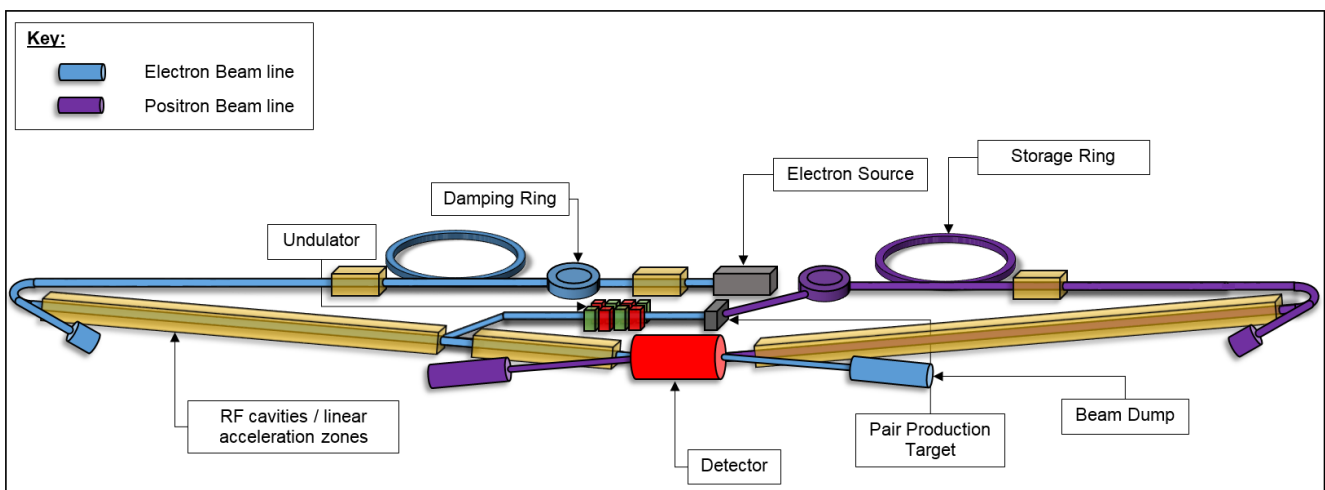


Figure 4.1: A schematic of LEPIC *designed by Lewis Simmons*

The collider shall operate at centre of mass energies of 300GeV, 1TeV, 3TeV and 6TeV. Several methods for achieving a variable collision energy were investigated, of which one of these was to build the collider in stages. This would involve building just enough of the collider to allow particle acceleration up to 300GeV. After one year of data taking, construction would resume to build the main linacs up to the required length for 1TeV collision energies. This process would be repeated until the entirety of the 72.9km linacs are built. However, due to the time constraints imposed upon the building and running of LEPIC, this method is not feasible.

Another explored possibility was taking data whilst the construction of the collider was still in progress. However it is predicted that tunnelling and other construction vibrations will have a serious impact on beam misalignment at the interaction point. Due to the fact that luminosity is dependent upon the overlap area of the two Gaussian beam profiles, it is essential to minimise any misalignment inside the detector.

It was decided that the most appropriate method for this project would be to build the entire accelerator for the maximum 6TeV collision energy and then deactivate a number of accelerating cavities along the main beam line according to the energy required. In other words, for the first year of run time only a small portion of the accelerating cavities will be activated. This will limit the energy of the beam to 300GeV at the interaction point, after it has traversed the entire 72.9km linac.

## 4.4 Energy Losses *written by Matthew Heath*

### 4.4.1 Acceleration Radiation Losses

As a charged particle is accelerated, it radiates energy in relation to its acceleration. These radiation losses must be accounted for in order to produce the centre of mass energies and luminosities required for the purposes of the collider's experiments. The power radiated by a relativistic point-like charged particle (such as the electrons and positrons in our collider) as it is accelerated is given by the relativistic generalisation of the Larmor formula [121] [122]

$$P = \frac{q^2}{6\pi\epsilon_0 c^3} a_0^2 \quad (4.3)$$

$$= \frac{q^2}{6\pi\epsilon_0 c^3} \gamma^6 \left( a^2 - \frac{(\vec{u} \times \vec{a})^2}{c^2} \right) \quad (4.4)$$

$$= \frac{q^2}{6\pi\epsilon_0 c^3} \gamma^4 a^2 + \gamma^6 \frac{(\vec{u} \cdot \vec{a})^2}{c^2} \quad (4.5)$$

where  $P$  is the power radiated by the particle,  $q$  is the charge of the particle ( $q = e$  in the case of electrons and positrons),  $a_0$  is the proper acceleration of the particle,  $\vec{u}$  is the velocity of the particle,  $\vec{a}$  is the Newtonian acceleration, and  $\gamma$  is the Lorentz factor of the particle,

$$\gamma = \frac{1}{\sqrt{1 - \frac{u^2}{c^2}}} \quad (4.6)$$

### 4.4.2 Linearly Accelerated Particles

When the electrons and positrons are accelerated down a linear path, as is the case for the main portion of our collider, the direction of acceleration is parallel with the direction of the velocity of the particles, thus leading the  $\vec{u} \times \vec{a}$  term in Equation 4.4 to be zero. Then considering the time derivative of relativistic momentum, equivalent to the change in energy of the particle as it travels in the acceleration direction,  $x$ , [123]

$$\frac{dp}{dt} = \frac{dE}{dx} = m_0 \gamma^3 a, \quad (4.7)$$

where  $m_0$  is the mass of the particle, this can be substituted for the  $a^2$  term of Equation 4.4 to give

$$P = \frac{e^2}{6\pi\epsilon_0 m_e^2 c^3} \left( \frac{dp}{dt} \right)^2 = \frac{e^2}{6\pi\epsilon_0 m_e^2 c^3} \left( \frac{dE}{dx} \right)^2 \quad (4.8)$$

for an electron or positron, where  $m_e$  is the mass of an electron and  $\frac{dE}{dx}$  can be thought of as the acceleration gradient that the accelerator is providing the particle. This shows that the power radiated by the particle is not dependent on its current energy or momentum, but rather on the external force acting on it.

The ratio of the radiated power to that supplied to the electron or positron by the accelerator is then represented by

$$\frac{P}{(dE/dt)} \approx \frac{e^2}{6\pi\epsilon_0 m_e^2 c^3} \frac{1}{u} \frac{dE}{dx}. \quad (4.9)$$

However, as the particles will be moving at highly relativistic speeds from the very start of the collider, the velocity of the particles can be approximated as that of the speed of light ( $u \approx c$ ) this ratio can be expressed as

$$\frac{P}{(dE/dt)} \approx \frac{e^2}{6\pi\epsilon_0 m_e c^2} \frac{1}{(m_e c^2)} \frac{dE}{dx}. \quad (4.10)$$

This shows that unless the electron or positron is gaining energy of  $m_e c^2 = 0.511 MeV$  in a distance of  $\frac{e^2}{6\pi\epsilon_0 m_e c^2} = 1.28 fm$ , then the energy lost by the particle in comparison to that being supplied to it is negligible. This energy gain, however, would be of the order of  $3 \times 10^{14} MeV/m$  and as this exceeds the acceleration gradients considered in our collider by many orders of magnitude, this allows energy loss caused by the acceleration of the particles in linear sections of our collider to be considered negligible [123].

#### 4.4.3 Circularly Accelerated Particles

For circularly accelerated charged particles, as in the case of the damping and storage rings as well as in bends in the particle beam-lines, the acceleration of the particle acts perpendicularly to the direction of tangential velocity. This reduces the  $\vec{u} \cdot \vec{a}$  term in Equation 4.5 to zero. This gives the power radiated by an electron or positron in a circular accelerator as

$$P = \frac{e^2}{6\pi\epsilon_0 c^3} \gamma^4 a^2, \quad (4.11)$$

which can be written as

$$P = \frac{e^2}{6\pi\epsilon_0 c^3} \frac{\gamma^4 u^4}{R^2} \quad (4.12)$$

as  $a = \frac{u^2}{R}$  for circular motion. The energy lost per revolution of a circular accelerator can then be calculated from

$$E_{loss} = Pt = P \frac{2\pi R}{u} = \frac{e^2}{3\epsilon_0 c^3} \frac{\gamma^4 u^3}{R}, \quad (4.13)$$

when the electrons and positrons are moving at relativistic speeds  $u \approx c$ , making use of the relation  $E = \gamma m_0 c^2$ . This energy loss per turn can then be converted to units that are practical for calculations [123]

$$E_{loss}(MeV) = 8.85^{-2} \frac{[E(GeV)]^4}{R(m)}. \quad (4.14)$$

Equation 4.14 can then be equated to the maximum energy required by a circular accelerator in order to obtain values for the required specifications of such accelerators.

## 4.5 Beam-Beam Interactions *written by Thomas Dack*

Beamstrahlung (from the combination of beam and bremsstrahlung[124]) is a specific case of synchrotron radiation, prominent within linear colliders. Beamstrahlung is described by the beamstrahlung parameter  $\Upsilon = \frac{2}{3} \frac{\langle E_c \rangle}{E_0}$ , where  $E_0$  is the nominal beam energy, instead of the critical energy,  $E_c$ , normally used in synchrotron radiation calculations.

The single-pass configuration within linacs requires the use of highly dense particle bunches, which results in these bunches having strong collective electromagnetic fields [125]. The electrons/positrons within a beam can then interact with the electromagnetic field produced by the other, radiating photons. These photons take energy away from the beam and pass through the detector at angles of less than a mrad away from the main beam.

The energy radiated by beamstrahlung processes is equivalent to Synchrotron radiation and removes energy from the final centre of mass energy of the collision system. This can result in a lower luminosity for the collider, as the particles within a bunch can have a reduced energy. Beamstrahlung photons can also be a cause of undesired detector background [126], as a fraction of the photons produced can have the energy required to decay via pair production. These  $e^+e^-$  pairs will be deflected by both the electromagnetic field during the collision and that of the detector itself. A number of these particles may deflect into the inner vertex detector, causing background readings within the calorimeters. As such the magnetic field and inner radius within the vertex detector must be carefully decided in order to minimise this background.

## 4.6 Guinea Pig Simulations *written by Thomas Dack*

GuineaPig (Generator of Unwanted Interactions for Numerical Experiment Analysis - Program Interfaced to GEANT) is a beam-beam simulation package designed by D. Schulte [127]. GuineaPig simulates interactions between the two beams inside a linear collider and so is useful for simulating the beamstrahlung effects discussed in section 4.5.

For this project a C version of GuineaPig was used. In the simulation progress GuineaPig converts the beam particles into a specified number of macro-particles; for the simulations of the LEPIC beamline each bunch was split into groups of 11250 macro-particles. The interactions between these macroparticles are then simulated and the resulting data must be re-normalised if a per-particle weighting is required. The input values for GuineaPig are entered into a file called acc.dat, which details the energies and bunch structure for a number of different accelerators as well as options to enable tracking for different processes. The program then writes a number of outputs to file, each containing the values produced as a result of the different processes. For this design project, the beam and pair output files were used. These relate to the beam energies and the  $e^+e^-$  pairs respectively. The energies and specific bunch structure for LEPIC were added as four new accelerators in the acc.dat file. These accelerators covered the four desired centre of mass energies, 300GeV, 1TeV, 3TeV and 6TeV, and all had a bunch structure of  $\sigma_x = 200\text{nm}$ ,  $\sigma_y = 2.0\text{nm}$  and  $\sigma_z = 300\mu\text{m}$  and  $2.00 \times 10^{10}$  particles per bunch.

### 4.6.1 GuineaPig Output

The two GuineaPig output files analysed for this project were used to investigate different interaction features. Both files were analysed using custom MATLAB scripts which read in the data files in order to produce plots of

the relevant relationships.

#### 4.6.2 Beam Energy Output

The output files beam1.dat and beam2.dat contain post-interaction data for the first and second beams respectively, with the number of particles in each file corresponding to the initial number of macro-particles. In the C version of GuineaPig used for this project each line in the beam output file contains 6 numbers:

1. The energy of the macro-particle in GeV
2. x position in the intersection plane, in  $\mu m$
3. y position in the intersection plane, in  $\mu m$
4. z position within the bunch, in  $\mu m$
5. the angle in the x plane,  $x'$ , in mrad
6. the angle in the y plane,  $y'$ , in mrad.

For the analysis of the particles energy after beamstrahlung emissions the energy of the macro-particles needs to be investigated. The MATLAB script takes the energy of each macro-particle and creates twenty bin histograms for the energies of each beam and cumulative density functions showing the spread of the energies. Twenty bins were used for these histograms so that the width of each bin was equal to 5% of the total bunch energy. This was used so as to give a good tolerance for the value of the beam efficiency, calculated by multiplying the two probabilities together. For the Z' group, 100 bins were used as a higher accuracy was required. This gave them bins showing a 1% change in particle energy, resulting in a total efficiency of 1.86%. For calculations a 1% efficiency was used, as it was decided to overestimate rather than underestimate running times. Histograms and CDFs for a centre of mass energy of 3 TeV are shown in Figure 4.2 and the plots for the other energies can be found in Appendix C.

Looking at the histograms for the four energies it can be seen that approximately 20% of the particles remain at the original energy. Specific percentages of these particles are shown in table 4.2.

Table 4.2: Table Showing the percentage of particles remaining at the original beam energy after beamstrahlung effects

Beam Energy	Beam Number	Percentage of beam within bin containing original energy
300 GeV	Beam 1	34.07%
	Beam 2	35.55%
1 TeV	Beam 1	18.93%
	Beam 2	19.61%
3 TeV	Beam 1	17.75%
	Beam 2	18.27%
6 TeV	Beam 1	22.71%
	Beam 2	22.17%
6 TeV	Beam 1	13.67%
Refined	Beam 2	13.62%

These percentages can be used to refine the higgs cross-sections, so as to account for the reduced population of the beam at the required centre of mass energy.

#### 4.6.3 Pair Data Output

The pairs.dat file outputs the information about secondary particles produced via pair production mechanisms. The version of GuineaPig used in this project includes 4 numbers in its pairs output file, with these being:

1. The energy of the particle in GeV. Here, a positive energy dictates an electron whilst negative shows a positron.
2. The normalized velocity in the x direction ( $v_x/c = p_x/E$ )

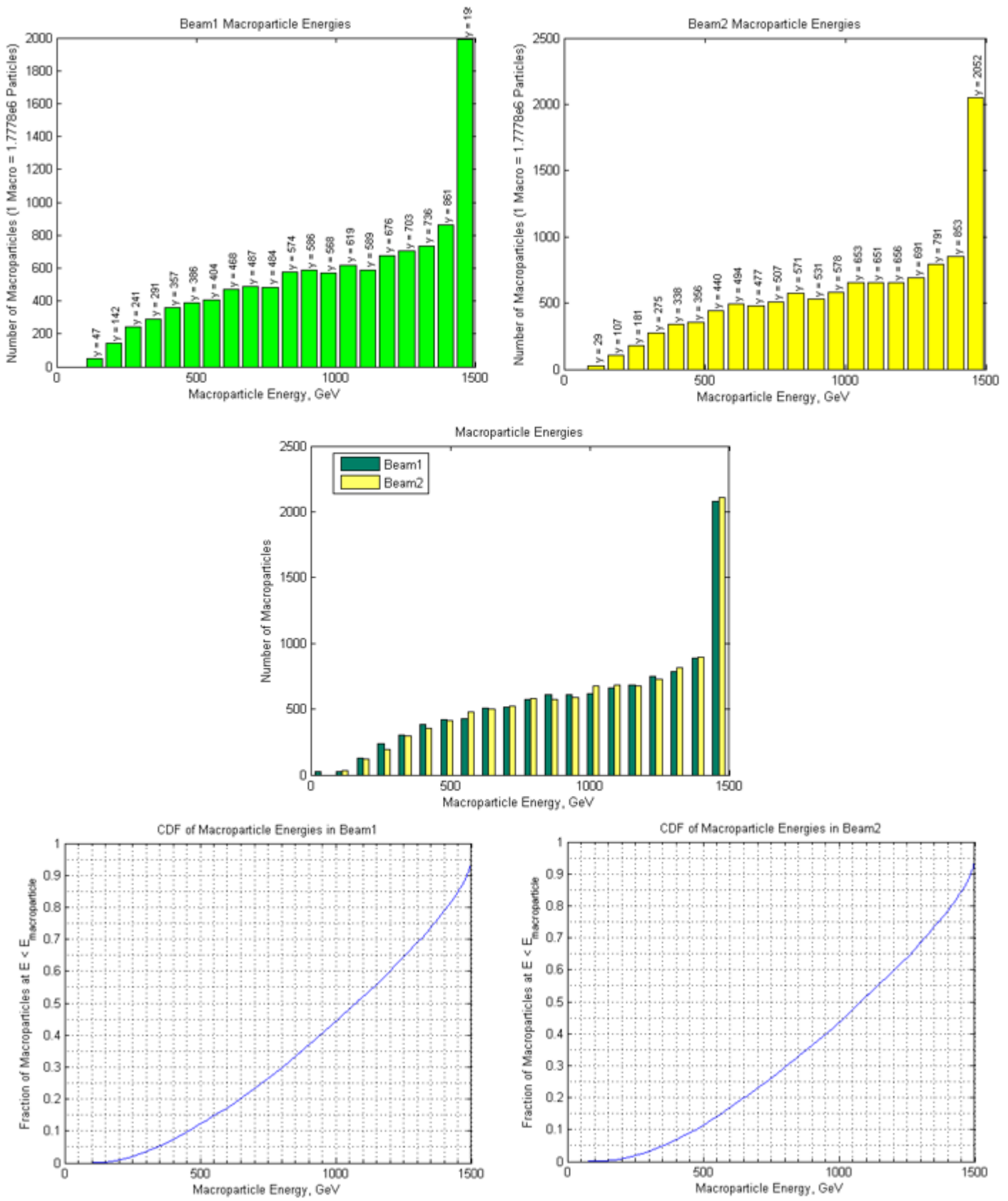


Figure 4.2: Histograms and CDFs produced from GuineaPig outputs for a centre of mass for 3 TeV

3. The normalized velocity in the y direction ( $v_y/c = p_y/E$ )
4. The normalized velocity in the z direction ( $v_z/c = p_z/E$ )

where the z component of velocity is equal to the transverse momentum,  $P_\perp$ , for each emitted particle. The transverse momentum of the electron is defined by the relationship

$$P_\perp = 0.3Bqr \quad (4.15)$$

where  $B$  is the magnetic field the electron is travelling through,  $q$  is it's coulomb charge and  $r$  is the radius of its path. Using this equation, calculations to find either the magnetic field required to keep the electrons/positrons produced within the inner radius of the vertex detector or the radius required to encapsulate all electrons/positrons at a given magnetic field. This were plotted as in equation 4.15 for the magnetic field strength of 5T and inner radius of 0.014m, as specified by the detector research group. Plots for a centre of mass of 3TeV are shown in Figures 4.3 and 4.4, with the rest of the energies shown in Appendix C.

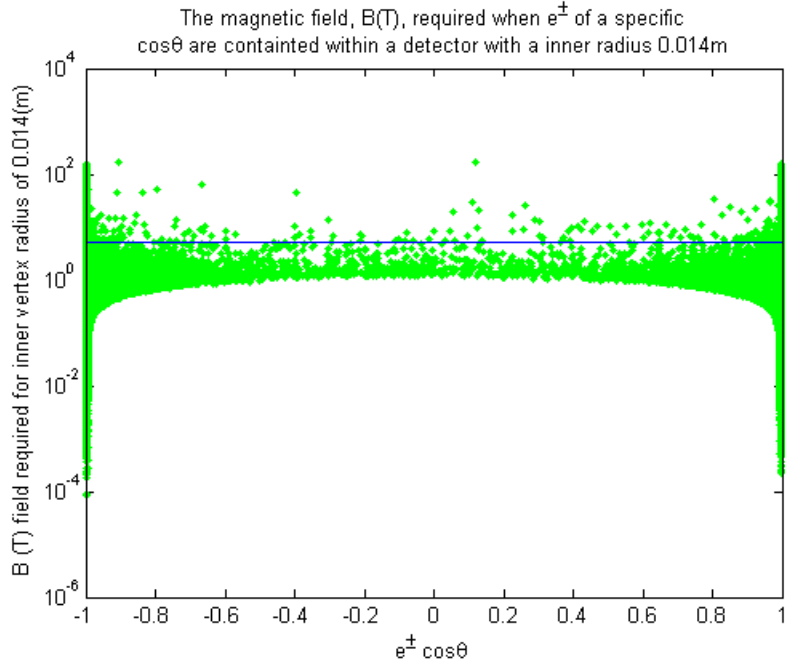


Figure 4.3: Plot showing the Magnetic field required to keep electrons with  $\cos(\theta)$  inside a vertex detector with radius of 0.014m. The blue line shows the proposed magnetic field of 5T.

These plots were passed back to the detector research group, who could adjust their parameters in order to best reduce to background from beamstrahlung  $e^+e^-$  pairs.

## 4.7 Beam Dimensions and Bunch Structure *written by Thomas Lane*

As was shown in section 2.7 our collider would have to produce an instantaneous luminosity of at least  $1.85 \times 10^{35} \text{ cm}^{-2} \text{ s}^{-1}$  for one years operating time. We therefore decided to use the beam structure shown in table 4.3 for our collider. The repetition rate is limited to 10Hz by the damping ring store time, with the bunch spacing limited to 20ns by the minimum time that the kicker magnets in the damping ring can extract individual bunches. The bunch population and the number of bunches per train are then constrained by the rate at which we can produce positrons in our collider. Taking these limitations into account we then calculated the beam dimensions that would produce at least the minimum instantaneous luminosity required.

Therefore our collider shall be running at an instantaneous luminosity of  $1.98 \times 10^{35} \text{ cm}^{-2} \text{ s}^{-1}$  this means that we shall be able to measure the branching fractions of the Higgs decay modes to the precisions shown in table 4.4 when running the collider for one year at a centre of mass energy of 1TeV.

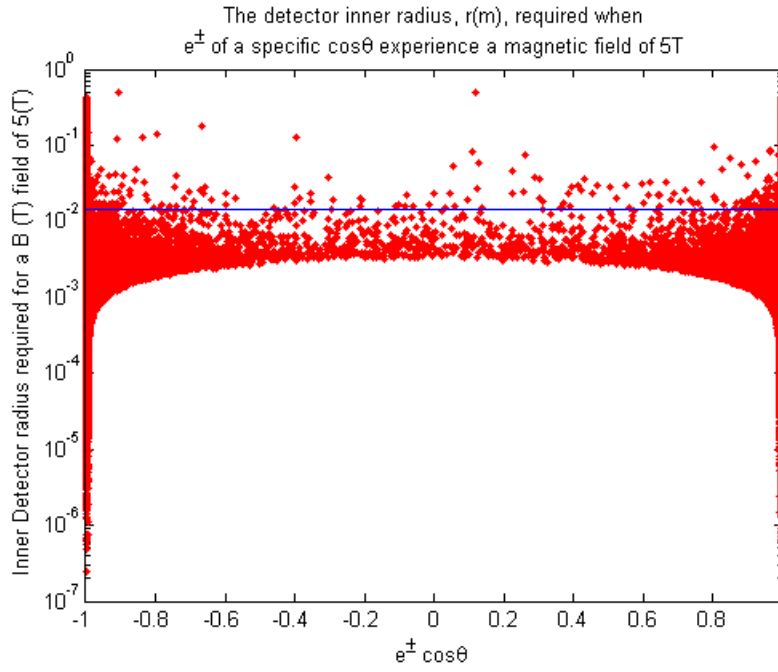


Figure 4.4: Plot showing the inner vertex radius required to encapsulate electrons with  $\cos(\theta)$  experiencing a  $B$  field of 5T. The blue line shows the proposed inner radius of 0.014m.

Table 4.3: The beam structure that we shall be using for our collider.

Collision rate, $f_{rep}$ (Hertz)	10
Number of Bunches, $n_b$	2500
Bunch population, $N$	$2 \times 10^{10}$
Bunch separation, $\Delta t_b$	20
Bunch length, $\sigma_z$ ( $\mu m$ )	300
IP horizontal beam size, $\sigma_x$ (nm)	200
IP vertical beam size, $\sigma_y$ (nm)	2
Collision crossing angle, $\theta_c$ (mrad)	20
Instantaneous luminosity, $L$ ( $cm^{-2} s^{-1}$ )	$1.98 \times 10^{35}$

Table 4.4: The Higgs decay modes and the predicted precision of our measurements of their branching fractions.

Decay Mode	Branching Fraction	Precision of Measurement (%)
b b-bar	0.577	0.12
c c-bar	0.0291	3.62
$\tau\tau - bar$	0.0632	1.64
$\mu\mu - bar$	$2.19 \times 10^{-4}$	488.63
$\gamma\gamma$	$2.28 \times 10^{-3}$	46.89
Z Z	0.0264	4
W W	0.215	0.44
Z $\gamma$	$1.54 \times 10^{-3}$	69.44
g g	0.0857	1.19

#### 4.8 Particle Production *written by Christopher Francis*

As this is a high luminosity electron positron collider we need to produce a very high amount of particles per second, for electrons this is a fairly trivial process as laser light on a photocathode can generate a large amount of

electrons through the photoelectric effect. However this process is more complex for positrons as they do not often occur naturally. In this case we have decided to make use of the main electron beam line in order to help generate positrons through the use of synchrotron radiation.

The electron source for the LEPIC collider must be able to deliver  $1 \times 10^{10}$  particles per bunch at a 10Hz repetition frequency and 2000 bunches per train to the interaction point with polarisation of around 60%. As some of these electrons will be used for positron production and not all will survive to the detector we require much more than this from initial production for transport to the Damping rings where they will compressed to the desired beam dimensions. In order to achieve this 2ns pulses of circularly polarised laser light are shone onto a Gallium Arsenic (GaAs) photocathode lattice chosen in order to maximise the electron polarisation[132]. Once the electrons have been produced they will be accelerated up to 5GeV by standard superconducting magnet modules for insertion into the damping ring.

For the positron source electrons will be extracted from the main beam line at 250GeV making use of a kicker magnet (this will incur some energy loss from bremsstrahlung). The first step in positron production is to pass the electron beam line through an insertion device known as a helical undulator, this piece of equipment consists of an alternating series of dipole magnets which create a static magnetic field along its length. The magnetic field causes the electrons travelling through the undulator to oscillate, as illustrated in Figure 4.5, with a specific wavelength and these deflections in turn cause photons to be emitted similarly to synchrotron radiation, in this case we are aiming for a photons of 20-25MeV which will be achieved using the following parameters:

Parameter	Specification
Magnetic Field Strength	0.9T
Wavelength	1.2cm
Length	150m

These parameters were chosen in order to keep the undulator strength parameter, shown in equation 4.16, as close to 1 as possible which is required in order to keep the photon energies within a narrow range.

$$K = \frac{eB\lambda}{2\pi m_e c} \quad (4.16)$$

This is important as we want the produced positrons to have a small energy spread as when it comes to accelerate them in the boosters any differences in energy will be exacerbated and this will leave us with a long bunch of many different energies which is very undesirable.

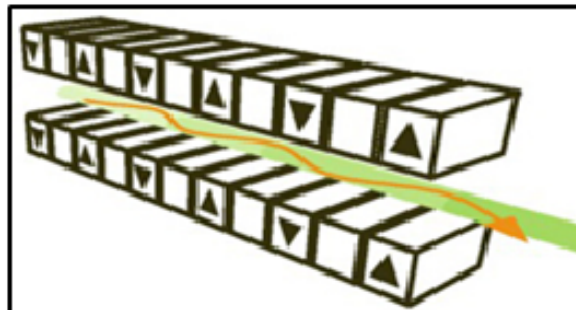


Figure 4.5: Diagram illustrating electron oscillations in helical undulators [133]

As stated above the photons generated by this process are expected to have an energy of around 20-25MeV, this is in order to maximise the probability of pair production taking place in the target. In addition the cross-section for pair production only increases with energy up to 20MeV and is then inversely proportional to radiation length of the material. Thus the most suitable target should be one with a high Z number and low radiation length with that in mind a titanium alloy was selected as the preferred option. This target will be set on a rotating axis in order to reduce the thermal effects from the photon strikes and allow some rudimentary control over the pulses. An example of this can be seen in Figure 4.6.

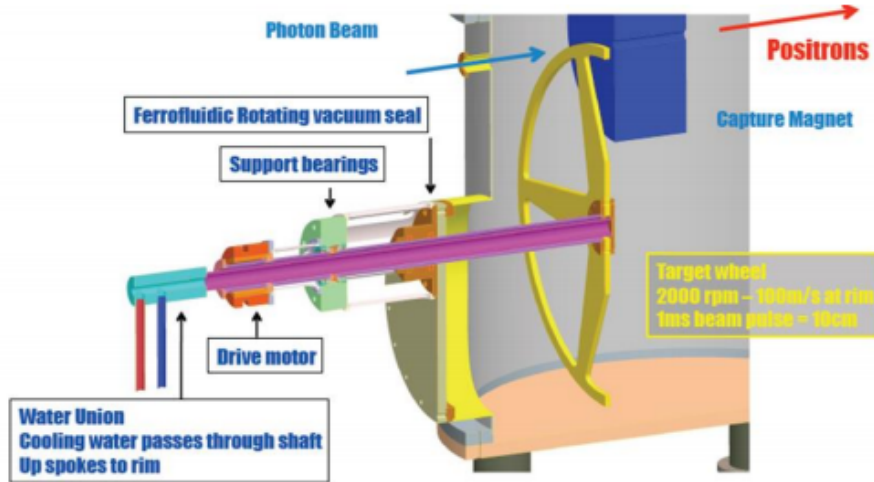


Figure 4.6: CAD example of pair production target on a rotating axis [134]

As we also wish to generate positrons with as higher polarisation percentage as possible a photon collimator can be used as an optional upgrade to maximise this. This is because the polarisation of the positrons produced is dependent on the angle of the incident photons and by eliminating any outliers we can increase positron polarisation significantly. The advantage of having a high polarisation beam for colliding, particularly in the search for SUSY particles, is that it can be used to suppress standard model processes which may interfere although this is not necessary for the Higgs hunt and so could be installed later during the downtime.

Immediately after the electron positron pairs have been produced we must have a way to separate them as well as dump the electrons and any excess photons that travelled through the target unaffected 4.15. The first step in doing this is an optical matching device which generates a solenoidal magnetic field strongest close to the target and falling away towards the beginning of the capture section, this magnetic field causes the positrons to bend away from the electrons to be inserted into the transfer pipes which will accelerate them individually up to 5GeV for insertion into the appropriate damping ring.

## 4.9 Damping Rings and Boosters

### 4.9.1 Particle Injector *written by Aaron Byrne*

Once the electrons or positrons have been produced, they need to be entered into the main body of the particle accelerator. To do this, a particle injector is used. This particle injector is used to focus the particle bunches that are entering the accelerator into a small beam, with the separation between the bunches still being the same that they were produced with. The focussing uses a quadrupole magnet, as described later in section 4.10.1. The particle injector then uses RF cavities and FODO lattices, as described in section 4.10.2. The RF cavities used are the same as those used in the main linac. As each RF unit gives the particles 1.56GeV of energy, the total number of units required to accelerate the particles if they have a 2 GeV production energy to the 5GeV wanted is two RF units. The power requirement for each RF unit is 249.6MW so, assuming that the power required by the focussing magnets is minimal compared to that required by the RF units, the total power requirement is 499.2MW.

### 4.9.2 Damping Rings *written by Aaron Byrne*

After exiting the injector, the bunch train moves into a damping ring. To enter the damping ring, an insertion kicker magnet is used to divert the beam from its straight line path into the ring by bending the magnetic field. It has a frequency of 50MHz, as this is the frequency at which the particle bunches are produced (20ns spacing). The damping ring uses synchrotron radiation to compress the bunch length to the desired size specified in section 4.7. Synchrotron radiation is produced by charged particles accelerating in circular paths. The amount of synchrotron

radiation emitted is inversely proportional to the radius of curvature (see equation 4.18). Therefore small damping rings are normally chosen because more radiation is released and the more radiation that is emitted, the faster the compressing, or damping, of the bunches is. This equation also applies to the individual particles. The particles at the front of the bunch have slightly more energy than those at the back, and hence release more radiation. This means that they are losing slightly more energy than the ones at the back and so the bunch compresses, as the energy of the particles within the bunches tend towards the same value.

Within the damping rings there are straight wiggler magnets, which are similar to the undulator used in the production of the particles, but uses much stronger magnets to generate larger oscillations, leading to more synchrotron radiation being released. This extra release of radiation improves the damping time of the bunches substantially, as very little energy is being lost via synchrotron radiation in the circular part of the damping ring.

In order to know how much energy the wigglers have to radiate, the total energy loss required for an adequate damping time, i.e. the time taken for the bunches to be compressed enough for extraction, needs to be calculated. Using equation 4.17 the total amount of energy required for any damping time can be calculated. ILC has a proposed damping time of 25ms, so an equal damping time would most likely be sufficient for our damping rings. When this calculation is applied to these damping rings the energy loss required to get a good damping time of 25ms is 4.19MeV, assuming the particles are moving with velocity very close to the speed of light,  $3 \times 10^8 \text{ ms}^{-1}$ .

$$U_0 = 2E_0 \frac{T_0}{\tau} \quad (4.17)$$

Equation 4.17: The equation for the total energy loss needed to achieve damping time  $\tau$  of 25ms.  $U_0$  is energy loss per turn(GeV),  $E_0$  is the average energy of the beam (GeV) and  $T_0$  is the time taken for one complete turn of the damping rings (s). [98]

Equation 4.18 shows the energy loss in the damping rings not including the wigglers.

$$U_0(\text{keV}) = 88.46 \frac{E(\text{GeV})^4}{r(\text{m})} \quad (4.18)$$

Equation 4.18: The equation for the total energy loss in the damping ring excluding the wiggler magnets [97].

Inserting the parameters for the damping rings (radius of 500m, which is calculated later) into equation 4.18 gives an energy loss of 110.6 keV, meaning that the energy needed to be radiated by the wiggler magnets is 4.08MeV per turn. Assuming that the peak magnetic field in the wigglers is 1.6T, the same as the ILC wigglers, a total length for the wiggler magnets of about 100m is achieved [97].

After energy loss, whether it is in the wigglers or the curved sections, the particles have to be accelerated back up to 5GeV energy, as this is the beam energy wanted. In order to do this, RF cavities can be used in conjunction with dipole magnets to keep the beam central in the pipe whilst bending. Low power RF cavities are going to be used, as the total energy lost is not much compared to the overall energy of the beam.

In order to keep the damping ring symmetrical two wiggler magnets will be used and they will be situated on opposite sides of the damping rings, in a straight section of pipe, as shown on Figure 4.7, with each wiggler measuring about 50m long and radiating 2.04MeV of energy. RF cavities can be inserted after the wigglers to accelerate the particles back up to 5GeV before the beam starts to bend again. An acceleration gradient of 0.2MeV/m is plausible and would mean that the RF cavity is 10m long, but may need to be a bit longer to allow for focussing.

On the circular sections of the damping ring, the energy losses are far less and so an acceleration gradient of 35.2eV/m is used by using low power RF cavities, as calculated in section 4.9.2.1.

Once the bunches are ready for extraction, an extraction kicker magnet is used to divert the bunches out of the damping ring on towards a storage ring. This kicker magnet has to have a frequency the same as the insertion kicker of about 50MHz, in order to produce the bunch separation wanted of 20ns for a train of 2500 bunches. However, the kicker magnet also has another property, the rise and fall time, or the time taken to reach full power once powered and to reach zero power when turned off. This has to be less than the bunch separation within the ring (Equation 4.19). The bunch separation in the ring does not need to be 20ns, which is the value for the bunch

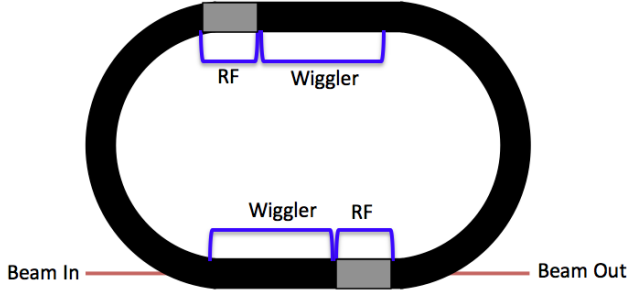


Figure 4.7: The layout of the wiggler magnets and the RF cavities inserted to compensate for the energy loss due to the wigglers. (*Not to Scale*)

separation outside the ring. As long as there are bunches 20ns apart so that two bunches with separation 20ns can be removed, other bunches may be inserted inbetween these bunches to allow for a smaller ring and hence a faster damping time. Equation 4.19 shows the bunch separation within the damping ring if an entire bunch train is to be inserted for damping.

$$d = \frac{2\pi r}{Nc} \quad (4.19)$$

Equation 4.19: The equation for the bunch separation.  $d$  is the bunch separation (s),  $r$  is the radius (m),  $N$  is the number of bunches in the train and  $c$  is the speed of light ( $\text{ms}^{-1}$ ).

A rise or fall time of about 4ns may be possible, following research into kicker magnets for the ILC [99]. This is the minimum separation within the damping ring. The reason that the rise and fall time needs to be less than the bunch separation is so that the kicker does not interfere with the bunch following the bunch that is to be extracted. Calculating the radius of the damping ring using equation 4.19 and a separation of 4ns gives a minimum radius of about 500m for the damping rings. With this bunch separation inside the damping rings, every fifth bunch will be extracted, giving a separation of about 20ns, as wanted. Once the bunch is extracted, they go towards a storage ring.

#### 4.9.2.1 Damping Rings Acceleration Gradient *written by Matthew Heath*

Due to the power radiated by the electrons and positrons as they are accelerated around the damping rings, as detailed in Section 4.9.2, they must be supplied with energy each turn to replace that which is lost in order to accelerate up to and remain the required maximum energy of 5GeV. For the 500m radius damping rings that are being considered for the LEPIC collider, the energy loss per turn of an electron or positron with an energy of 5GeV is (Equation 4.14)

$$\frac{E_{loss}}{turn} = 110625 \text{ eV}, \quad (4.20)$$

This requires the damping rings to supply the particles with this energy each turn. To calculate the energy that must be supplied to the particle for every meter that it travels, this required energy is divided by the circumference of the path of the particle,

$$\frac{110625eV}{2\pi(500m)} = 35.2 \text{ eV/M}, \quad (4.21)$$

corresponding to a required acceleration gradient of  $G = 35.2V/m$ , the potential difference the particles pass through every meter of their path.

### 4.9.3 Storage Rings *written by Aaron Byrne*

Storage rings act much the same as damping rings, but do not have wiggler magnets in them, as they do not require extra radiation to be produced. They are used to store the particles, most commonly the positrons as they have to be created from the electron beam line, and hence will have to be stored for a short time until the electron beam has been created and prepared for collision. The bunch trains are stored until they are required to be used for collision, but they do deteriorate over time, so they cannot be stored for too long. The kicker magnets would be the same specification as the kicker used in the damping rings for extracting the bunches, as the beam still has the same properties as it did when leaving the damping rings.

The magnets within the ring also have the same schematic as the damping ring magnets, being RF cavities and FODO lattices to keep the beam focussed, as well as dipole magnets to bend the path of the beam and keep it central whilst moving in a curved path. The storage ring will have a 1000m radius. This is to keep the energy losses down to a minimum, as synchrotron radiation is inversely proportional to radius and so a large radius will keep the synchrotron radiation losses to a minimum, which will keep the bunch structure as good as possible. The acceleration gradient required to keep the particles within the ring at a constant energy is 8.8 eV/m. See section 4.9.3.1 To get this gradient, we can use very simple superconducting RF cavities to accelerate the particles [100]. The design would be similar to the ones used in the main linac, but require much less energy to be transferred to the particles as they travel through. The power required to run the storage rings is negligible if compared to the main linac, as the acceleration gradient is so small so less power is needed to power the RF cavities. Therefore, we can neglect the power that these would require to run. Once the bunches are kicked out of the storage rings they enter a booster.

#### 4.9.3.1 Storage Rings Acceleration Gradient *written by Matthew Heath*

For the 1000m radius storage rings being considered for this collider, storing electrons or positrons at 5GeV, the energy lost per turn of the ring is (Equation 4.14)

$$\frac{E_{loss}}{turn} = 55313eV. \quad (4.22)$$

This energy loss requires an acceleration gradient of

$$G = \frac{55313V}{2\pi(1000m)} = 8.8V/m \quad (4.23)$$

in order to maintain the energy and bunch structure of the particles.

### 4.9.4 Pre Linac Booster *written by Aaron Byrne*

Before the particle trains enter the main linear accelerator which accelerates them to much higher energies, a small linear accelerator, or booster, will accelerate the particles from 5GeV to 10GeV. This uses the same RF cavities used in the particle injector and in the main linac. Therefore, as each unit gives the particles 1.56GeV of energy, three can be used to get the particles up to 9.68GeV, which is the closest that the energy can get to 10GeV using the RF units. This booster is used to give the particles enough energy to reach the main accelerator and also reduces the length of the main linear accelerator slightly. A large energy boost is not wanted as the transfer pipe, where the beam curves 180 degrees and is inserted into the main linac, would lose a lot of energy via synchrotron radiation, thus rendering a lot of the acceleration useless, as the particles would have to be accelerated back up to the energy again due to the large synchrotron losses. This boosters power consumption is 748.8MW. Once the bunches have been accelerated and have travelled through the transfer pipes, the energy dispersion across the bunch may be uneven and so the bunch may have been stretched to more than 300 $\mu$ m, the value that it was compressed to in the damping rings, so they need to be compressed back to size before entering the main linac.

#### 4.9.5 Energy Losses at the Bends *written by Matthew Heath*

At the two extremes of the proposed LEPIC collider are two 180 degree bends with a radius of curvature of 500m. These bends will introduce radiation losses as if the particles travelling through half a turn of a circular path, leading to the 10GeV beams that travel through them to lose a maximum of (Equation 4.14)

$$E_{loss} = \frac{1}{2}(8.85 \times 10^{-2} \frac{10^4}{500}) = 3.54\text{MeV.} \quad (4.24)$$

Consequently, the energy of the beams leaving these bends would have a minimum energy of

$$E_{beam} = 9.99646\text{GeV.} \quad (4.25)$$

#### 4.9.6 Bunch Compressors *written by Aaron Byrne*

After the particle bunches have passed through the transfer pipes, they enter a bunch compressor. A bunch compressor is used to compress bunches back to the size wanted for insertion into the main accelerator, as they may have gained length in the booster or transfer pipes. The compressor to be used is a magnetic chicane bunch compressor, which is a series of four dipoles. Within the bunch, the particles at the front of the bunch are moving slower than those at the back of the bunch if the bunch is properly chirped. So as they move through the compressor the slower particles follow a longer path as they have more time to be affected by the dipoles (See Figure 4.8)

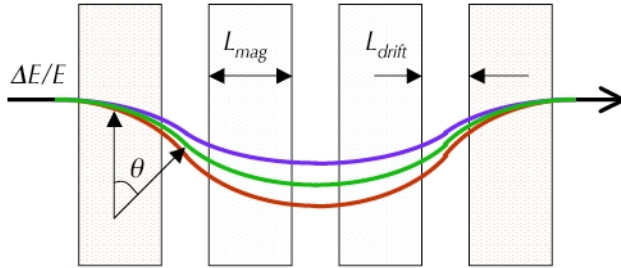


Figure 4.8: The setup of the bunch compressor. The purple line represents the path followed by the high energy particles at the back of the bunch the red is the lower energy particles at the front of the bunch. The green line represents the path the average energy particles would follow [101].

By changing the values of  $L_{mag}$  and  $L_{drift}$  [101], the bunch can be compressed to the correct size wanted for the final collisions.

#### 4.10 Main Linac *written by Thomas Lane*

In a collider a particle beam is generally accelerated using radio frequency (RF) cavities, a RF cavity is a metallic chamber which contains an electromagnetic field that is used to accelerate the charged particles in the beam [116]. Superconducting RF cavities provide an efficient high-gradient acceleration and come in many forms depending on the desired characteristics of the acceleration. The RF cavity is effectively a high-frequency version of an Inductor-Capacitor-Resistor (LCR) resonant circuit in which the RF power at the point of resonance builds up a high electric field that can be used to accelerate charged particles, the basic components of a RF cavity are shown below in Figure 4.9.

RF cavities usually have a length that is given by  $d = \frac{\beta\lambda}{2}$ , where  $\beta \approx 1$  is the particle velocity as a ratio of the speed of light and  $\lambda$  is the wavelength of the RF used. The cavities used in particle acceleration are ‘elliptical cavities’, this means that the cavity consists of two elliptic arcs with a straight line between them, as shown in Figure 4.9.

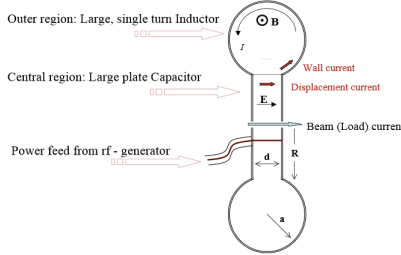


Figure 4.9: The basic components of an RF cavity[117].

This setup is used for two main reasons, firstly because the elliptic arcs eliminate multipacting, where secondary electron emission occurs in resonance with the RF field, which was a large limiting factor on the performance of pillbox cavities, and secondly because the shape of the elliptic arc can be optimised to increase the distribution of the magnetic field along the surface, making the magnetic field more uniform across the cavity, which then increases the accelerating gradient while reducing losses.

Superconducting RF cavities are the accelerators usually used in modern linacs with the attraction of producing a higher acceleration field while also retaining a high quality factor, which is the ratio between the energy stored in the cavity and the energy lost in one RF period. For the superconducting RF cavities, the electron pairs in the cavity are paired in a coherent quantum state and so there is no resistance to direct current (DC) below the critical magnetic field line, which is given by equation 4.26 below, this field line leads to a critical temperature below which the cavity is superconducting even with no present magnetic field. Some critical temperatures for different materials given in table 4.5, where  $H_{C1}$  and  $H_{C2}$  are the upper and lower critical fields. In high-gradient particle accelerators the power dissipated in the waveguide walls is proportional to the square of the accelerating electric field, and so there are large resistive losses per unit length. To counter this problem the electron beams are operated on a pulsed cycle with a bunch width of a few microseconds or less.

$$H_c(T) = H_c(0) \cdot [1 - (\frac{T}{T_c})^2] \quad (4.26)$$

*Equation 4.26: The critical field of a superconducting material can be calculated from the temperature of the system  $T$  and the critical temperature for the corresponding material  $T_c$ .*

Table 4.5: Characteristics of some superconducting materials[118].

Material	$T_c(K)$	$H_{C1}(T)$	$H_{C2}(T)$
Lead	7.7	0.08	0.08
Niobium	9.2	0.17	0.4
$Nb_3Sn$	18	0.05	30
$MgB_2$	40	0.03	3.5

The most effective setup of superconducting RF cavities that has been found is the New Low Surface Field (NLSF) cavity, which has the potential to produce an accelerating gradient of 60MV/m with an optimum operating frequency of 1.5GHz [119]. This design aims to minimise the ratio of the surface electric field to the accelerating gradient and also the ratio of the surface magnetic field to the accelerating gradient, while maximising the fractional bandwidth of the accelerating mode. The NLSF cavity has a maximum electric field on the surface of the cavity of 126MV/m and a maximum magnetic field of about 230mT on the surface, which are within the critical field limitations for Niobium at 2K. There are two models for the NLSF cavity, one which has nine integrating cavities and one which has eight integrating cavities with a superconducting quadrupole package located at the centre of the string.

#### 4.10.1 Focusing

Particle beams naturally diverge, therefore we need a set of magnets to focus the beam to a point. In general optical physics a lens can be used to focus light to the corresponding focal length for the used lens, a diagram of

this is shown below in Figure 4.10. In the optical analogy the rays are converged to the focal point by a focusing angle which depends on the distance from the centre of the lens that the ray enters the lens, this angle is given by  $\tan(\theta) = \frac{x}{f}$ .

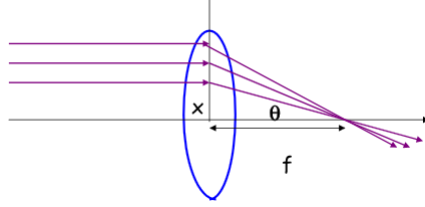


Figure 4.10: An example of a basic focusing lens [120].

For a colliding beam moving with momentum  $p$  a magnetic lens would need to impose a momentum kick of  $\Delta p$  on the beam to focus it. This momentum kick would have to increase with distance from the centre of the magnetic lens like the focusing angle, and so the magnetic field acting on the beam would need to increase with distance from the centre of the lens. The focal length and focusing strength,  $k$ , of a focusing magnet can be derived from the Lorentz force equation as shown below in equations 4.27 and 4.28.

$$\frac{1}{f} = \frac{eL}{pc} \times \frac{dB_y}{dx} = \frac{L}{Bp} \times \frac{dB_y}{dx} \quad (4.27)$$

*Equation 4.27: The focal length of a quadrupole magnet can be calculated from the width of the magnet  $L$ , and the change in magnetic field across the magnet  $\frac{dB_y}{dx}$ .*

$$k[m^{-2}] = \frac{1}{fL} = \frac{e}{pc} \times \frac{dB_y}{dx} = \frac{0.299}{\beta E[GeV]} \times \frac{dB_y}{dx} [T/m] \quad (4.28)$$

*Equation 4.28: The focusing strength of a quadrupole magnet can be calculated from the focal length of the magnet  $f$  and the width of the magnet  $L$ .*

This requirement for a magnetic field which is proportional to the distance from the centre of the magnet is achieved by using a quadrupole magnet, this has four poles at an orientation shown below in Figure 4.11. For a negative particle travelling out of the page, the force on the particle on the right side of the magnet is to the right and the force on the left side of the magnet is to the left, therefore this magnet is horizontally defocusing. However towards the top of the magnet the particle would be subject to a downward force and towards the bottom of the magnet it would feel a force upwards towards the centre of the magnet, therefore a quadrupole magnet focuses the beam in one plane while defocusing it in the other plane.

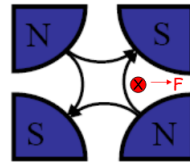


Figure 4.11: A quadrupole magnet [120].

In an accelerator this quadrupole magnet can be used to provide a net focusing in both planes, this is done by using an array of focusing and defocusing magnets called a FODO lattice shown in Figure 4.12, which together produce a focal length which is dependent upon the distance between the two magnets,  $d$ , as shown in equation 4.29.

$$\frac{1}{f_{combined}} = \frac{1}{f_1} + \frac{1}{f_2} + \frac{d}{f_1 f_2} \quad (4.29)$$

*Equation 4.29: The combined focal length of two quadrupole magnets can be calculated from the two magnet focal lengths  $f_1$  and  $f_2$  and the distance between the two magnets  $d$ .*

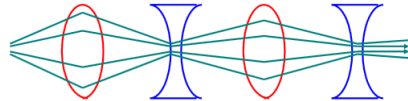


Figure 4.12: An example of a FODO lattice [120].

#### 4.10.2 Main Linac Design

In our main linac we shall be accelerating particle beams up to a maximum energy of 3TeV in order to carry out 6TeV centre of mass collisions. The main linac lattice shall consist of a 9-8-9 RF unit configuration in which there are three cryomodules, the two outside cryomodules consist of 9 niobium superconducting radio frequency (SRF) cavities with the centre cryomodule consisting of 8 niobium SRF cavities and a quadrupole magnet in the middle of these 8 cavities. The RF units shall be 36 metres in length with 2 metres of warm drift space between each RF unit, this means that the distance between each quadrupole magnet shall be 38 metres. A layout of this RF unit configuration is shown below in Figure 4.13.

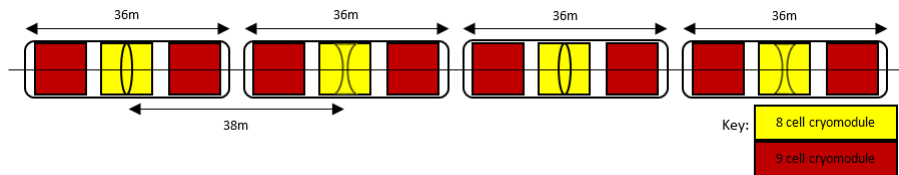


Figure 4.13: The layout of the FODO lattice that we shall be using for our collider, where the red boxes are the 9 cell cryomodules and the yellow boxes are the 8 cell cryomodules.

The quadrupole magnet in the centre cryomodule of each RF unit shall alternate between a focusing and defocusing quadrupole in order to create a FODO lattice that will focus the particle beam along the x and y axes while travelling through the main linac. This FODO lattice will therefore have a distance of 76 metres between each focusing quadrupole, where each FODO cell is 38 metres in length. The phase advance per FODO cell shall be 75 degrees along the x-axis and 60 degrees along the y-axis, leading to a maximum beta-function value of 120 metres in the x-axis and 140 metres in the y-axis.

The niobium SRF cavities used in the main linac shall be cooled in a 2K superfluid-helium bath in order to keep the niobium below its critical temperature of 9.2K, these cavities have the potential to produce an accelerating gradient of 60MV/m functioning with a RF of 1.5GHz and are about 1 metre in length. Assuming that the cavities shall be functioning at 60MV/m, each RF unit shall produce a change in momentum for the beam particles of 1.56GeV and so to accelerate the electrons and positrons to 3TeV from the 10GeV injection energy we shall need 1917 RF units in each linac. This means that each linac will need to be at least 72.9km in length.

In order to run our collider at the four energies we shall turn off RF units that are not required keeping an equal spacing between the RF units that are turned on, the details of how many RF units shall be required to be turned on for each energy is shown in table 4.6. Each RF cavity in the main linac shall have an input power of 9.6MW and so each RF unit shall use 249.6MW of power. The power consumed by these RF units when running at the four different centre of mass energies is also shown in table 4.6.

Table 4.6: The number of RF units required to be turned on for the chosen centre of mass energy collisions and how much power these RF units will use.

Beam Energy (GeV)	RF Units Required On	Distance Between Each RF Unit (m)	Individual Linac RF Power (GW)	Total RF Power Input (GW)
150	90	809	22.46	44.92
500	315	231	78.62	157.24
1500	956	76	238.62	477.24
3000	1917	38	478.48	956.97

#### 4.10.3 Measuring the energy of the collider particle beams *written by Lewis Simmons*

For any collider system it is imperative that the energy of the beams being used is known incredibly precisely. This enables the targeting of certain interaction thresholds and is required for safety concerns. It is beneficial to have multiple methods of determining beam energy to cross-reference readings using independent measurements; this has been deployed at past colliders such as LEP. Since this collider uses RF cavities similar to those proposed at the ILC and has a fairly similar beam structure it is probably wise to use ILC style techniques for determining the energy of the beam.

The main way of measuring a particle beams' energy is via its interaction with a magnetic field in a magnetic chicane. In brief the path of the beam is deviated by some known field and the change in trajectory can be measured using beam position monitors (BPM's). Then the beam energy can be isolated via calculation for depending on the exact arrangement of the chicane. The setup of such a chicane is outlined in Figure 4.14 below. These have been successfully deployed at a variety of experiments to date but never for such high energy electron / positron beams. Despite this, the ILC and CLIC systems are both deploying this technology so it is feasible to scale such a design for TeV scale beam energies. Current ILC predictions show that an arrangement similar to that shown in 4.14 can achieve  $\delta E/E \approx 10^{-4}$  for the 1 TeV ILC beam [114] [115].

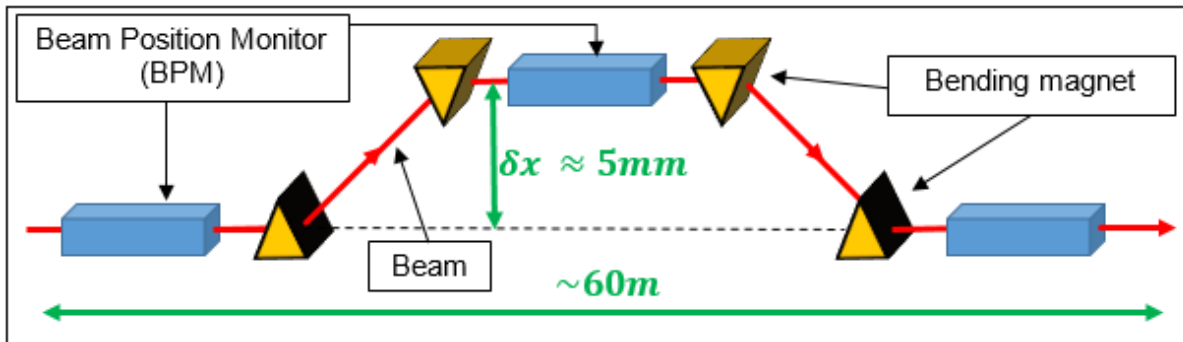


Figure 4.14: A schematic of a 4 magnet chicane with ILC like dimensions [114]

The above equipment is placed a few hundred metres before the interaction point to obtain an energy measurement as close to the beam energy present inside the detector as possible [114]. After the interaction point a variety of other energy measuring techniques can be deployed. Here the beam can be altered as it is no longer required for interactions. With this in mind the conventional choice for measuring beam energy here are synchrotron radiation detectors. The beam will be again deflected with a magnetic field and the radiation released via synchrotron means will be measured rather than beam position. From this a beam energy can be isolated. This requires a less focused beam and no specialised BPM's unlike the method before the interaction point. However, after the deflection process the beam is left in a more diffuse state, unsuitable for collisions. Despite this, it has been demonstrated that this method can achieve similar precisions  $10^{-4}$  as with the above chicane [114] [115].

Using this combination of energy spectrometers and perhaps some of the Compton Scattering based methods currently being tested, the beam energy should be able to be determined to a precision of  $10^{-4}$  for the 1 TeV and lower energies of the collider system. However for the 3/6 TeV regimes further high energy experimentation is required.

#### 4.11 Collimation *written by Lucy Bignell*

In addition to focusing, the beam must also be collimated before it reaches the interaction point. Collimators are located in the beam delivery system in order to mitigate background in the detector and provide protection against mis-steered beams from the main linac. The collimation system also plays an important role in reducing radiation exposure to machinery and personnel [84].

The main objective of the final focus collimators is to remove stray particles from the beams in order to reduce the detector background to an acceptable level. The collimator aims to achieve a smooth Gaussian beam profile by removal of halo particles. These are particles which lie outside of the beam core due to significant energy deviation or betatron amplitude [85]. The beam halo contributes to the detector background by several methods. Firstly, stray particle collisions within range of the detector cause unwanted electromagnetic showers that can interfere with data taking. Moreover, the halo particles can emit synchrotron radiation which is equally unfavourable within the surrounding area of the detector [86].

One of the main issues faced by the collimator is survivability. The beam halo is reduced by physical interception of a number of halo particles and thus the collimator must tolerate continual impact of a significant fraction of the beam. Moreover, as part of its protection functionality, the collimator must also withstand impact from full energy, errant beams and not require frequent replacement [87]. For LEPIC, this means that the collimator must handle a direct hit from a 3TeV pulse of 2000 bunches. In order to reduce the risk of completely destroying the collimator, thin 'spoilers' are employed. The spoilers are located ahead of 'absorbers' in order to reduce the impact of the beam halo [87]. An electromagnetic shower is created when a high density bunch hits the collimator which enables energy to be deposited via pair production and photon radiation. Due to the high density of bunches used in the collider, this will cause rapid heating and thus expansion of a very small volume of material [88]. At an approximate thickness of only one radiation length, the spoilers endure minimal heating upon impact but have a sufficient effect on the beam halo so that the multiple-radiation length absorbers are not damaged. A suitable spoiler material to use is beryllium as it has a radiation length of 35cm and is therefore almost transparent to incident beam particles [87]. Moreover, beryllium is electrically conducting which prevents static charge build up in the material.

The optimum aperture dimensions that will be used for LEPIC beam collimation are  $20\mu\text{m}$  for spoilers and  $200\text{mm}$  for absorbers [87]. Having spoiler apertures that are several orders of magnitude smaller than that for the absorbers is essential for the spoilers to generate sufficient beam divergence. As shown in Figure 4.15, multiple Coulomb scattering at the spoilers causes angular divergence of the beam and thus, upon arrival at the absorbers, the beam size is large enough to not cause extensive damage [89]. The absorber material will be titanium which has a radiation length of 3.56cm [90]. After the energy spread of the beam has been amplified by the spoilers, the absorbers are responsible for complete removal of halo particles.

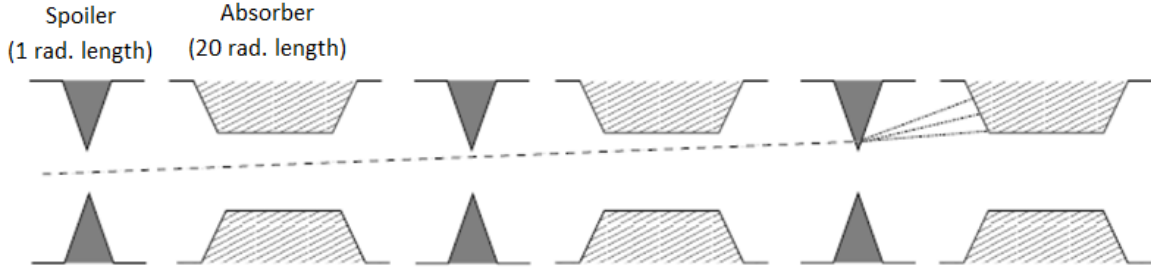


Figure 4.15: The smaller aperture spoilers cause angular beam divergence such that damage is not caused to the absorbers upon impact [89]

In order to provide efficient beam collimation, the spoiler-absorber system must be placed within close range of the high energy beams. However, adverse effects occur if the component apertures are too tight. Specifically, transverse wakefields are generated as a result of beams passing too close to the collimator [88]. Wakefield effects are a severe cause of beam jitter and emittance growth [91] and thus it is important to strike a balance between effective beam halo removal and minimal wakefields. One way to do this is to use tapered spoilers as shown in Figure 4.16.

## 4.12 Machine-Detector Interface *written by Raveena Deol*

The Machine-Detector Interface concerns the region where the electron and positron beams meet and interact with the detector. It specifically looks at the magnets that will be used in the final-focusing of the beams; the components used in maintaining the stability of the beams and ensuring all components within the detector region are aligned to achieve a high luminosity [128].

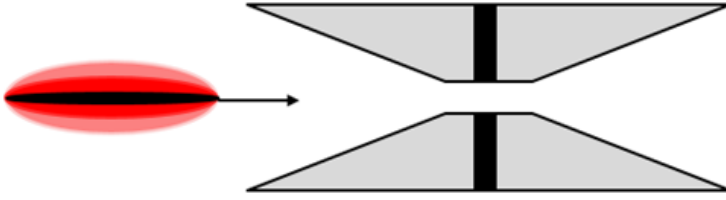


Figure 4.16: Tapering of the spoilers reduces the risk transverse wakefields.

### 4.13 Final Focusing

The quoted luminosity of  $1.85 \times 10^{35} \text{ cm}^{-2} \text{ s}^{-1}$  is most likely to be achieved if the beams are focused to a nanometre-scale [129]. For this a system must be designed to not only focus the incoming beams, but also to re-direct any outgoing beams back towards the interaction point, reducing the particle loss. Strong quadrupole magnets placed close to each other along the beam line can be used as final-focus magnets. The ideal quadrupole magnet has a gradient magnetic field that varies with the distance from the beam rather than a constant field. As seen in equation 4.30 [130] the field is proportional to the distance from the axis:

$$B_x = \Gamma y \quad \text{and} \quad B_y = \Gamma x \quad (4.30)$$

where  $\Gamma$  is the field gradient and is the same in both directions. The strength of the magnetic field should be determined by the final beam sizes required at the interaction point. As stated in table 4.3 Structure the beam dimensions at the interaction point will be  $\sigma_x = 200\text{nm}$  and  $\sigma_y = 2\text{nm}$  indicating a very thin, flat beam. In order to achieve this, a magnetic field strength of 575T/m has been proposed as experiments at CLIC have indicated that this allows the beam to be focussed down to a single nanometre [128].

The setup will use permanent-magnet quadrupoles (PMQ) with adjustable magnetic fields as this will then allow us to vary the field according to beam dimension requirements. In order to do this, the PMQs can be split into separate rings with an outer diameter of 100mm and inner diameter of 55mm, that can then be rotated accordingly as seen in Figure 4.17.

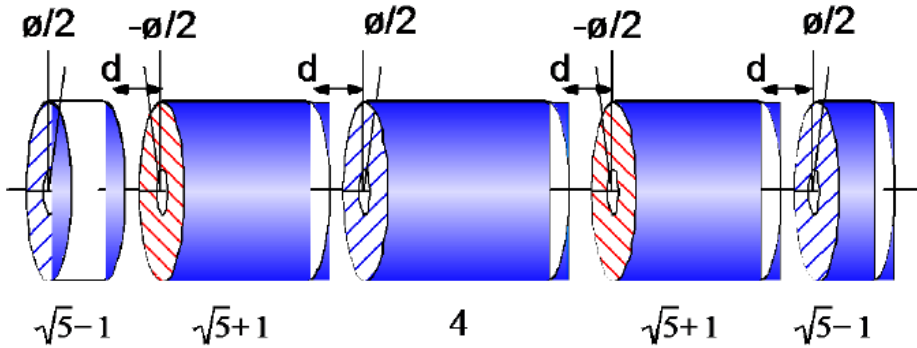


Figure 4.17: Schematic of an adjustable-strength PMQ divided into five rotatable rings [129].

Each ring is rotated so that it is oppositely polarised from the ring before it, this is denoted by the  $\frac{\phi}{2}$  and  $-\frac{\phi}{2}$ . Each of the rings are equally spaced however they have different lengths: 20mm, 55mm, 70mm, 55mm and 20mm [129] from left to right with a total length of 24cm. The total setup will have 12 of these PMQs for each beam and will need to be placed less than 5m away from the interaction point, which places them in the detector region.

Since the final focusing quadrupoles will be in close-proximity with the detector, they are likely to be disrupted by the magnetic fields from the detector solenoid. In order to shield the quadrupoles from this, they can be encased in a magnetic shield pipe that consists of an anti-solenoid coil wound around it. This balances the force applied by

the detector's magnetic field. To add to this, we must also shield the quadrupoles from the magnetic field caused by the outgoing beams. This can simply be resolved by a laminated iron casing [129].

#### 4.14 Stabilising the beam

At the interaction point a very fast system, operating on nanosecond timescales within each bunchtrain, is required to compensate for residual ground-motion-induced jitter on the final quadrupole magnets by steering the electron and positron beams into collision [131].

The proposed system in the intra-train beam-based feedback. The system comprises three stripline beam-position monitors (BPMs) and two stripline kickers, analogue BPM processors, a FPGA-based digital processing board with fast Analogue-to-Digital Converters(ADC), and kicker-drive amplifiers [129]. The setup is shown in Figure 4.18.

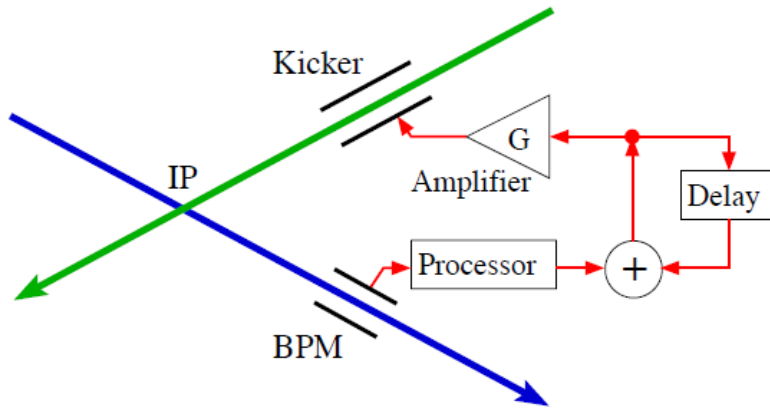


Figure 4.18: Schematic of the intra-train feedback system at the interaction point [128].

The two stripline kickers (K1, K2) are used to provide fast vertical beam corrections. Since we have a flat beam with  $\sigma_x \approx 2\text{nm}$  this is very small and so deviations in this axis are more likely to cause a larger problem in having the correct beam dimensions at the interaction point. However this is essential in increasing our luminosity as it is inversely proportional to the beam dimensions. Two of the BPMs are associated with the two stripline kickers as they provide the analogue signal which is then converted via the ADCs, and the digital signal is then amplified before reaching the kickers. A third stripline BPM (P1) is used to witness the incoming beam conditions. The analogue output is then sampled, digitised and processed in the digital feedback board. Analogue output correction signals are sent to a fast amplifier that drives each kicker.

The (Accelerator Test Facility) ATF can be operated to provide an extracted train that comprises up to 3 bunches separated by an interval that is selectable in the range 140–300 ns. This is ideal as our bunches are separated by  $\approx 200\text{nm}$ . This provides a short train which is be used for controlled feedback system tests . The FONT5 intra-train feedback system aims to stabilise the beam orbit by correcting both the position and angle jitter in the vertical plane on bunch-to-bunch time scales [129]. This is shown in Figure 4.19.

We must ensure that both the electron and positron beams are aligned withing the quadrupole magnets and also that they come in to a collision at the interaction point. We can use the number of events detected in the dectector to tell us if the beams are well aligned as this will give a higher number of events and therefore a higher luminosity.

#### 4.15 Beam Dump *written by Lewis Simmons*

The role of the beam dump within a collider system is to safely dispose of the large powers associated with particle beams. The main design of linear collider electron-positron beam dump was pioneered at SLAC in the 1960's. The design consists of large volumes of cool, pressurised water into which the beam is fired through via a hyper-transparent window. Once the beam enters the water its energy is deposited through scattering processes (and the

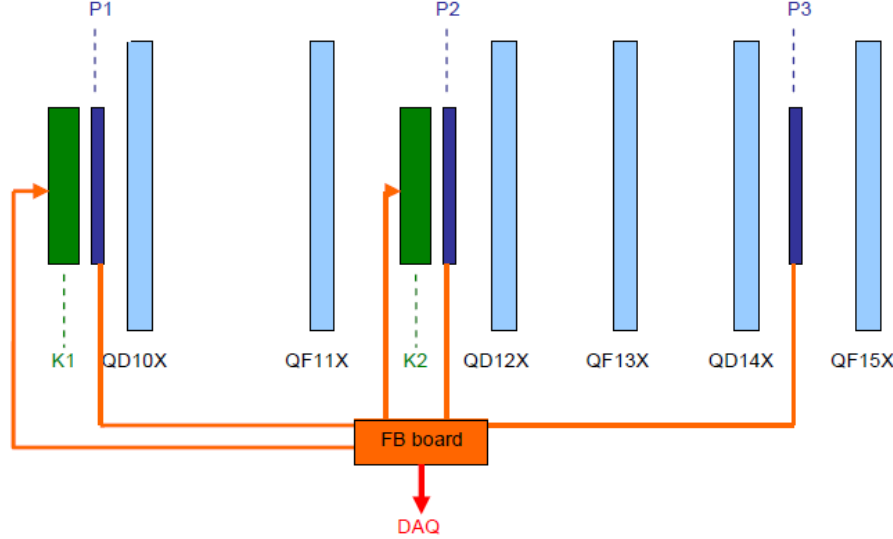


Figure 4.19: Schematic of the two stripline kickers, three BPMs and the ATF quadrupole magnets. [129].

annihilation mechanism for positron beams). The heat generated by these processes allow hotter pockets of water to form, these then dissipate and move, presenting the beam with bulk cool water. This freshly exposed, cool water then heats up and the process repeats. Pressurising the water inhibits boiling and hence gas build up. To absorb any escaping beam particles the water vessel is coated in shielding materials such as tungsten and then isolated further by substantial concrete and iron shielding [109] [110]. Despite these systems not yet being deployed on such high energy beams, research is indicating that the systems should be scalable from the lower energy variants. This is supported by the notion that both the proposed ILC and CLIC systems are adopting this technology. A drawback of these systems is the by-products formed during water-beam interactions. These have to be disposed of to prevent inefficiencies and may be radioactive [109] [112] [113]. The significant challenge for these systems is the design of the window between the beam line and the beam dump. This must be transparent to the beam to prevent the deposit of energy into the window. To ease the burden of creating a hyper-transparent window the beam will be scanned across the window surface to reduce thermal stresses on any one point. The beam can also be made more diffuse using various arrangements of magnets or smaller noble gas beam dumps before the water dump. This reduces the deposited power per unit area of the window by dispersing the beam [LS7] [LS8]. Since the proposed collider will operate up to a centre of mass energy of 6TeV, it is vital that 3 TeV electron / positron beams can be safely disposed of. This also means that a beam power of 192MW must be dissipated without causing large detector backgrounds. Specifications for the main beam dump will be similar to ILC / CLIC systems and are shown in table 4.7 and a simple schematic of the main beam dump is shown in Figure 4.20 [110] [111] [112]:

Table 4.7: Expected beam dump parameters for this collider system.

Parameter	Specifications (Main beam dump)
Length	Approx. 30m
Diameter	Approx. 5-10m
Material	Tungsten casing
Contents	Pressurised water ( $\approx$ 10bar CLIC)
Window	Thin titanium ( $\approx$ mm thick) with beam scanning
Position	200-500m from IP in shielded concrete cavern

Before the beam dump a series of collimation magnets will separate out components of the post interaction beam. This means that positrons produced from beamstrahlung pair production processes can be removed from the spent electron beam and vice versa. This lowers photon background in the detector from annihilation processes. This

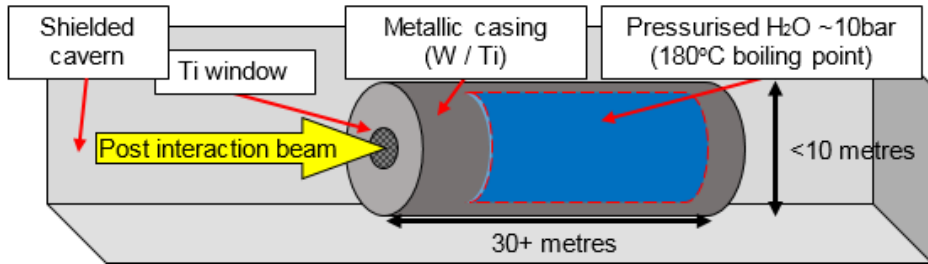


Figure 4.20: A simple schematic of the main beam dump.

apparatus is placed immediately outside the detector to limit annihilation background as soon as possible. Using this technology it is feasible to dispose of the incredibly powerful electron / positron beams required for this collider. With the addition of smaller beam dumps of a similar pressurised water design at other points throughout the system, beams can be safely discarded in the event of system malfunction. Despite this design, the beam dump field is being constantly refined. It may be that advances in hybrid liquid-gas beam dumps could render conventional designs slightly obsolete but sufficient experimentation on such systems has not yet been completed. These certainly require less specialist windows and smaller water vessels / shielding amounts [109] [110].

#### 4.16 Location of the Collider *written by Aaron Byrne*

A physical real world location has not been decided for the accelerator, as this was not required according to the project brief. However, any possible site for the construction of the accelerator would have to meet a set criteria. This criteria is outlined below.

The collider would have to be built below ground. This is mainly to protect people who reside near the location from radiation from beamstrahlung losses or from synchrotron radiation. Also, finding an overground space large enough to accommodate a 150km long accelerator that cannot have any bends within it is also a very unrealistic proposition. As the collider has to be built underground, there cannot be any nearby obstructions or services that may cause large vibrations, as the beam line may be misaligned by vibrations. This rules out areas near to large cities with large underground networks, whether that is sewage pipes, water pipes or train services, such as the underground or the metro. It should also not be located near large groundwater sources or underneath large bodies of water such as reservoirs or lakes, as water may damage the shell of the building.

The accelerator would also have to be built far from fault lines, as any sheering of the fault could cause irreparable damage to the accelerator or the magnets. Also vibrations from tectonic movements would also affect the aligning of the two beams, so avoiding building the accelerator near fault lines is a priority.

One final thought to consider is the type of rock that the accelerator should be situated in, as the type of rock affects the size of the vibrations. The type of rock towards the outer reach of the accelerator does not particularly matter, as it is so far from the central point, but it should be non-porous, as porous rocks may let water reach the outer surface of the building housing the accelerator, and may cause damage or cracks to appear, causing loss of structural integrity. The rock surrounding the centre of the accelerator, where the detector is located, should be a one of the more solid rock types, such as granite. This means that if there were any vibrations towards the outer edges of the detector that were to make the beam line become misaligned, the hard rock at the centre would keep the two beam lines aligned, and so the problem would correct itself, without the need for a computer system to realign as the beams near the detector. Hard rock would also reduce the amplitude of vibrations that would occur close to the detector and so the misalignment of the beams would not be too problematic.

## 5 The Detector Design

### 5.1 Introduction *written by Adrian Cross*

In order to probe the possible new physics processes, described in sections 2 and 3, a detector needs to be built with the capacity to detect and distinguish between different particles as well as make measurements on their energy and momentum. The detector also needs to be able to run effectively at 300GeV, 1TeV, 3TeV, 6TeV with the required resolution. As we have an  $e^+e^-$  collider there will be fewer overall particles being produced compared to a hadron collider meaning that there will be less overall data, from interactions, to analyse. LEPIC contains one detector centred on the interaction point of the collision.

### 5.2 The Detector Layout *written by Adrian Cross*

The detector consists of seven distinct components which fit together to create the detector. The materials and sizes of each component has been calculated individually and then put together to get the overall layout. Figure

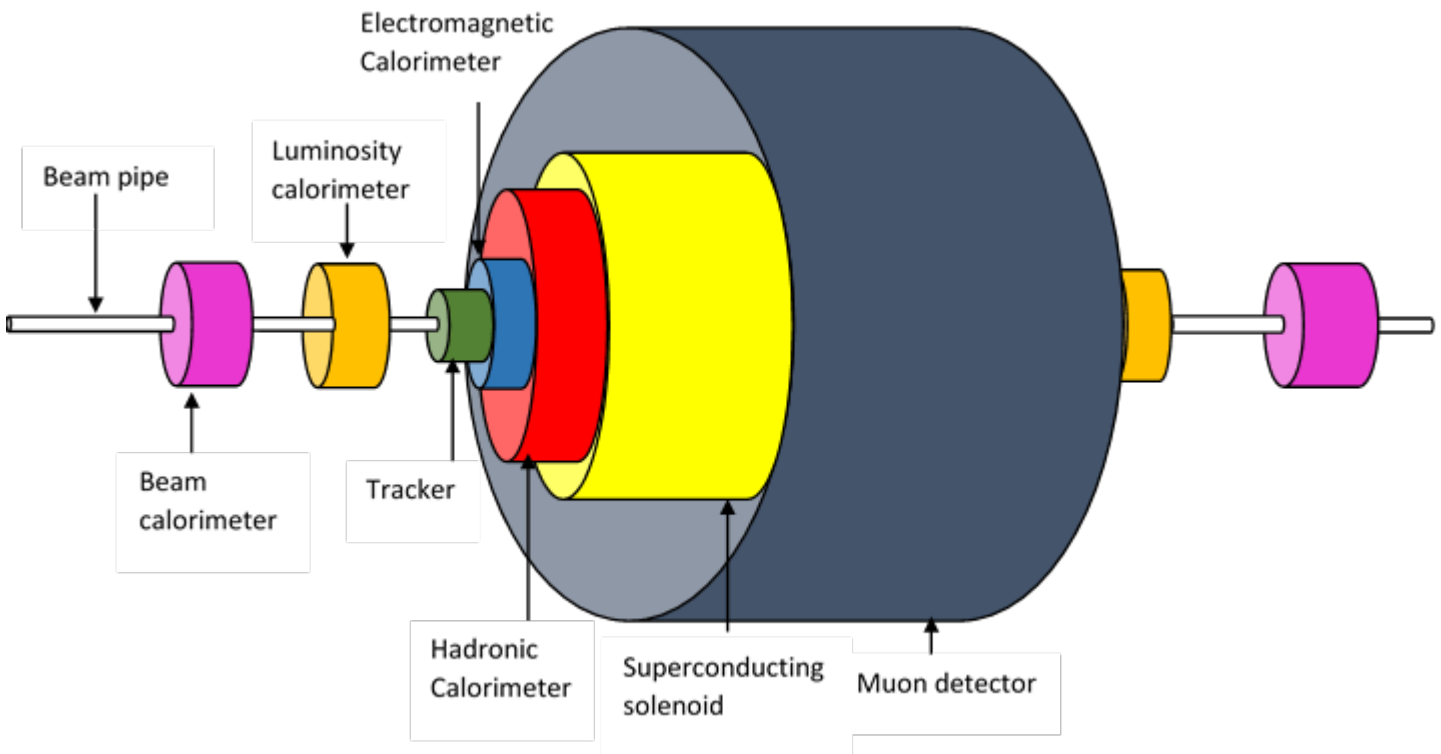


Figure 5.1: Cross section of LEPIC detector with each component labelled

5.1 shows the overall layout of the detector containing the luminosity calorimeter (LumiCal), beam calorimeter (BeamCal), beam pipe, tracker, hadronic calorimeter (HCAL), electromagnetic calorimeter (ECAL), solenoid and muon detector with an overall radius of 5.57m and length of 15m. The dimensions of each component is shown in Figure 5.2.

The high energy electron positron pair enter from the beam pipe and will interact at the interaction point in the centre of the detector. Particles are then created which travel through some of the detector layers. These particle interact with different parts of the detector dependant on their properties, this is shown in Figure 5.3.

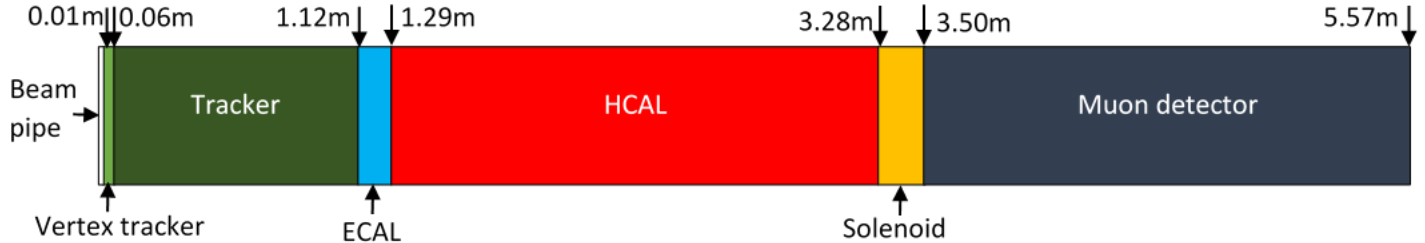


Figure 5.2: Scale diagram of detector components with radii at the component borders

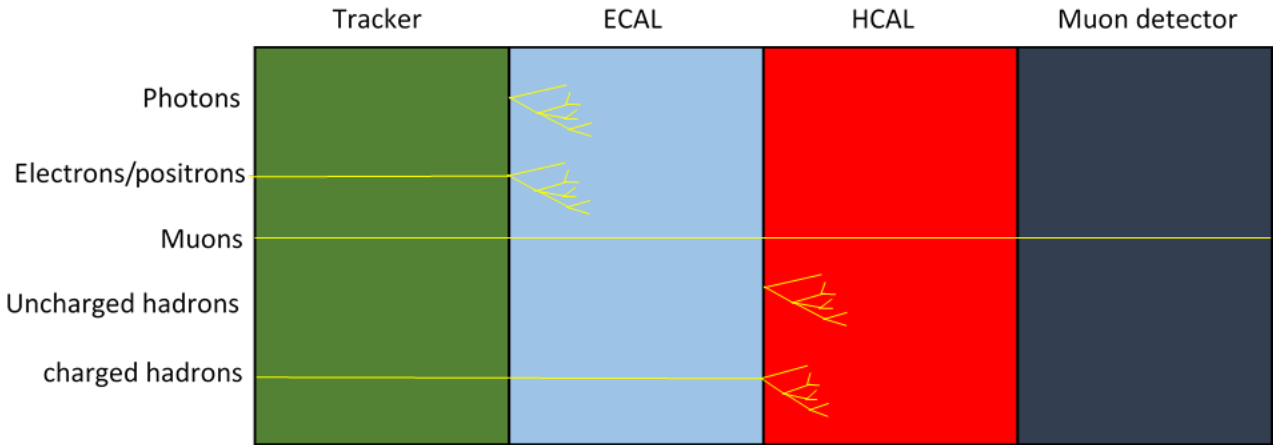


Figure 5.3: Interaction of particle types with different detector components

The charged particles are tracked in the tracking chamber. The ECAL measures the energy of photons, electrons and positrons which enter it, the HCAL measures the energy of charged and uncharged hadrons which enter. Finally the muons, which very rarely interact with the rest of the detector, are picked up mainly in the muon detector. The placement of the solenoid assists with this as it blocks any particles, other than highly penetrating muons, from entering the muon detector and giving false detections.

### 5.3 Coordinate System *written by Andrew Clarke*

The simulations undertaken in this project require us to understand the detector coordinate system that we use. We will use the conventional detector coordinate system where the direction of a particle is determined by pseudorapidity,  $\eta$  and the angle between the projection of the particle onto the x-y plane and the x-axis,  $\phi$ . The direction of the beams are along the z-axis. Figure 5.4 shows a diagram of this coordinate system. Equation 5.1 shows the definition of pseudorapidity. Pseudorapidity is a useful quantity to use as it is invariant under a Lorentz transformation along the z-axis (the beam line). This makes moving between the lab frame and the centre of mass frame, which will differ if there is initial state radiation [141].

$$\eta = -\ln(\tan \frac{\theta}{2}) \quad (5.1)$$

*Equation 5.1:  $\eta$  is the Pseudorapidity,  $\theta$  is the angle between the x-y axis and the beamline (z-axis) in radians.*

### 5.4 Solenoid *written by Adrian Cross and Dwayne Spiteri*

A magnetic field is not required in the muon detector as the tracker has a high momentum resolution. The more momentum a particle has the less the particle is curved in the tracker. Therefore, due to the high energy nature

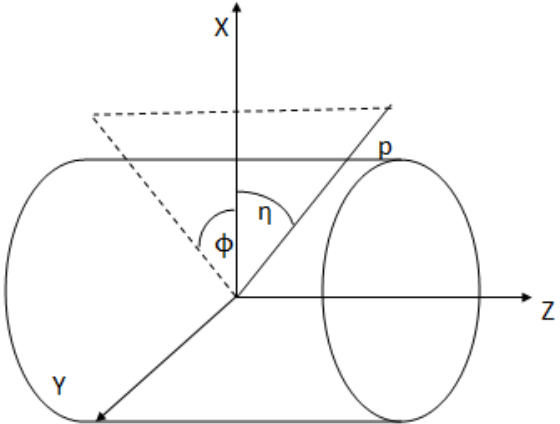


Figure 5.4: The coordinate system used within the detector.  $p$  is the momentum of the particle

of the LEPIC collider, a high magnetic field strength is required in order to attain a high momentum resolution. The size of the LEPIC magnet is also considered. The position of the magnets is an important consideration in a detector. Whatever the size of the magnet, it's inner radius limits the size of all of the components within it. In order to find a realistic solenoid size, position and strength current magnet systems that exist already, ATLAS and CMS, were investigated.

#### 5.4.1 CMS

The CMS magnet[147] consists of a single high strength solenoid which contains the beam pipe, tracker, ECAL and HCAL. This magnet has a strength of 4T, a diameter of 5.9m and 12.9m in length. The material used for magnet is superconducting niobium-titanium coils which are cooled to a temperature of 4.65K.

#### 5.4.2 ATLAS

The ATLAS magnet system has a central solenoid, an air-core barrel toroid and two end-cap toroids which are all superconducting[135, 136, 137, 138] and are made out of varying ratios of Aluminium, Copper and Niobium-Titanium alloy[139]. The alloy wires on a Copper mesh and Aluminium support allow for a rapid charging and discharging time and improves the linearity of the magnetic field such that it is more uniform when compared to single filament conductors[140]. The central solenoid surrounds the tracking chamber and provides the it with a B-field of 2T[135] and the barrel toroid surrounds the muons detectors to supply them with a peak field of 3.9T but at certain  $\eta$  the field from the end-cap magnets adds to the total field felt by a muon[139]. Depending on the point resolution of the muon detectors these toroids may not be needed in our new system (see section 5.9).

It is important to note that the magnetic properties of these materials are recorded at 4.2K. Higher fields can be reached when coolant colder than liquid Helium is used [140]. Another way of achieving a high magnetic field strength would be to use Niobium-Tin as the superconducting filaments alloy instead of Niobium-Titanium but the disadvantage of this is that the material is more brittle and therefore harder to wind.[140]

#### 5.4.3 Setup

The LEPIC solenoid design will be based on the CMS magnet. The solenoid wraps around the beam pipe, tracker, ECAL and HCAL in order to facilitate the bending of particles in the tracker. This also prevents the solenoid from blocking particles entering the calorimeters and instead stops most of the particles entering the muons detector, except for muons. This allows the correct particles to enter the calorimeters and prevents particles, other than muons, being picked up in the muon detector. The material used for the superconducting Rutherford cable is the

NbTi superconductor at a temperature of 4.5K. This low temperature is achieved using a liquid helium coolant. An aluminium alloy is attached to the Rutherford cable for structural reinforcement [142]. Using these materials and parameters a 5T superconducting magnet with an inner radius of 3.28m, an outer radius of 3.50m and 15m in length can be built which suits the purposes of this collider.

## 5.5 Forward Calorimetry *written by Adrian Cross and Dwayne Spiteri*

The forward calorimetry has two main roles; to calculate the luminosity of the experiment after particles meet at the interaction point, and to extend the region of calorimetry closer to the beamline.

### 5.5.1 Luminosity Calorimeters - LumiCal

LumiCal measures luminosity by the detection of Bhabha-scattered electron-positron pairs. Bhabha scattering is the process where  $e^+$  and  $e^-$  interact electromagnetically (pure QED) to produce only  $e^+$  and  $e^-$  in the final state. Figure 5.5 shows some example Feynman diagrams that lead to a pure  $e^+e^-$  final state.

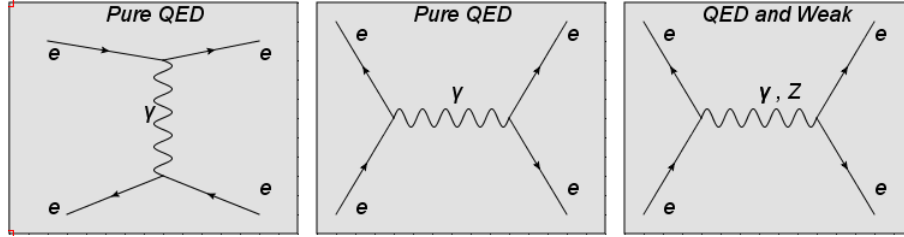


Figure 5.5: The left and centre Feynmann diagrams are for Bhabha scattering and the one on the right shows a process that competes with this.

The cross section for the pure QED case (as opposed to the QED/weak annihilation process) is proportional to  $\frac{1}{\theta^3}$  where  $\theta$  is the angle between the Lumical and the beamline [144]. LumiCals, therefore, have two effective regions: a fiducial region and a non-fiducial region. The fiducial region occupies the inner radial layers where a high sensitivity to Bhabha events ideal for calculating L is present, and the non-fiducial region, made up of the outer radial layers, is used for general calorimetry. CLIC and ILC plan to use silicon and tungsten in the same way that the ECAL works (see section 5.7). The main difference is that the detector segmentation is very fine to allow the trajectories of individual particles to be found. Hence calorimeter distances need to be very precisely known. The Luminosity of the interaction is calculated using Eq.5.2.

$$L = \frac{N}{\sigma_{theory}} [144] \quad (5.2)$$

where N is the number of detected Bhabha events and  $\sigma_{theory}$  is the theoretical cross section of the process.

When a high energy electron or photon is incident on a thick absorber, typically silicon, it initiates an electron shower as shown in Figure 5.6.

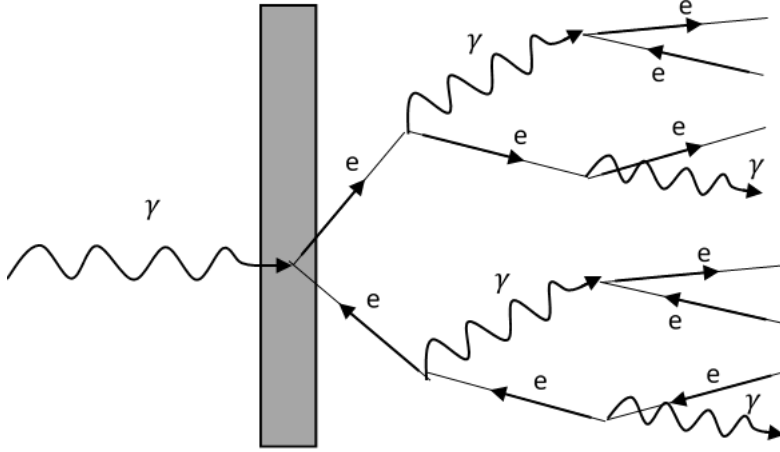


Figure 5.6: Particle shower in a luminosity calorimeter

The incident photon produces a high energy electron positron pair which in turn radiate high energy photons. This process repeats until the electron energy falls below the critical energy,  $E_c$ , which is the point where ionisation loss per radiation length is equal to the electron energy. At this point the electrons lose energy only by ionisation and excitation and no more electrons or positrons are generated[145].

The mean length in which a high energy electron loses all but  $1/e$  of its energy by bremsstrahlung and  $7/9$  of the mean free path for a high energy photon is called the *radiation length*,  $\chi_0$ . The Molière radius models development of the electrons shower in the transverse direction and therefore gives a good approximation of the required size of the luminosity calorimeter. This radius is given by the equation

$$R_M = \chi_0 \frac{E_s}{E_c} \quad (5.3)$$

where the multiple scattering energy  $E_s=21\text{MeV}$ . Using this radius only 10 percent of the EM shower energy lies outside the detector, on average, when positioned around the shower centre. The Molière radius is defined as the radius of a cylinder which would contain on average 90% of the energy of the incident particle. Minimization of this value improves the shower position resolution of the calorimeter as the transverse size of the shower is reduced. This means any showers are contained within a smaller volume which assists the resolving of separate showers.

There are two types of error that correspond to an overall error in the luminosity calorimeter. The statistical error and the reconstruction bias which occurs due to polar biasing[146]. The inverse cubic fall-off of the Bhabha cross-section with the polar angle manifests experimentally as large differences in the Bhabha events counting rate, for small changes in the angular acceptance range[145].

The statistical error, as dictated by Poisson statistics, is given by one over the square root of the number of Bhabha scattering events observed, and the reconstruction bias is given by approximately twice the difference between the reconstructed and generated polar angles divided by the inner bound of the LumiCal most sensitive to Bhabha events, called the fiducial region[145].

The relative error in the luminosity from LumiCal is shown below in Equation 5.4.

$$\frac{\Delta L}{L} = \frac{1}{\sqrt{N_B}} \oplus \frac{2\Delta\theta}{\theta_{min}^f} \quad (5.4)$$

where  $N_B$  is the number of observed Bhabha scattering events,  $\Delta\theta$  is the difference between the generated and reconstructed polar angles and  $\theta_{min}^f$  is the lower bound of the fiducial region of the detector.

While it is possible to borrow the work used by the CLIC collaboration to construct a LumiCal to work in our detector for centre of mass energies of 3TeV or lower, it is not possible to assume that this will work for 6TeV. Assuming that the materials used can stand up to the increased radiation dose, simulations will have to be done

on the distribution of the energy deposited per layer, and the radial distance at which 90 % of the shower energy can be found within for 3TeV beams. This is necessary in the construction of LumiCal's as it sets the size of the fiducial region and the number of layers needed in the Calorimeter.

### 5.5.2 Beam Calorimeters - BeamCal *written by Dwayne Spiteri*

BeamCal is placed on the beampipe further down the beamline than LumiCal and thus occupies a lower polar angle from the interaction point. The advantage of BeamCal, aside from extending the calorimetry to lower polar angles, is that it can use bremsstrahlung pairs and Bhabha scattering to obtain instantaneous Luminosity measurements and allows a two-photon veto which may help suppress the background for possible new particle searches[143].

Due to the fact that BeamCal occupies a low polar angle and is close to the interaction point, the radiation incident of BeamCal is much larger than that incident on LumiCal[145]. The use of silicon to absorb electrons like ECAL would mean that the drop-off in efficiency would be very quick and therefore would require constant maintenance. ILC, operating at a maximum of 1TeV, were having difficulties finding a material that could cope with the estimated  $100\text{Mrad}$  per year of EM-induced radiation and the  $5 \times 10^{13} \text{cm}^{-2}\text{y}^{-1}$  of neutron flux[143]. A possible solution to this problem at these energies is to use radiation hardened materials such as Diamond and GaAs[143].

Operating at 3TeV and 6TeV means a larger amounts of radiation incident on the detectors and the increase in detector hardness required may mean that the existence of low polar region calorimetry may not be possible. However, the research and development into BeamCal materials is ongoing.

## 5.6 Trackers *written by Ryan Jones*

Both the tracking detector and the vertex detector can be considered trackers; both of these components of the detector will be discussed in detail, with parameters decided based on considerations of the beam energies and the nature of electron positron collisions.

### 5.6.1 Tracking Detector

The tracking detector is arguably the most important part of the whole detector; it allows the reconstruction of the paths that are taken by charged particles from the point of collision of the electron and positron beams, data that can be used to determine the position and momentum of particles. This is especially important because momentum data is required to reconstruct particles from the initial collision; missing momenta can therefore be attributed to particles that are unable to be tracked, either because they decay too quickly, or because they are not charged.

The primary operation of the tracking detector involves utilisation of the ionisation process, which occurs as charged particles pass through matter. The material that the tracking detector is comprised of will have energy deposited from the particles, with positive and negative charge pairs being created as a result of this process. These pairs will drift towards the nearest electrodes, which are integral to the tracking detector, where a current will flow as a result of the drift, indicating position of the charged particle by analysis of this process. This will then pass through a circuit designed to amplify the signals so that they can be measured and recorded; the whole process is summarised in Figure 5.7.

The two most considered methods of designing a tracking detector for an electron positron collider are fairly similar [149], but with important differences that provide differing advantages under certain circumstances. These methods are to build a tracking detector with the primary material being silicon, and to build one that is a hybrid of silicon and gaseous materials, in Time Projection Chambers (TPC) format. There are many gasses that can be used in a gas-filled detector, with examples such as argon, each with slightly different advantages that can be seen in [150].

While the differences between these two types of tracking detector are fairly minimal, they are all very significant, as even minimal changes can have large effects on track reconstruction. The efficiency of the material is vital so that the current can actually be picked up and therefore used; this is mainly determined by the primary ionisation. For this, silicon is much more effective; as it is a semiconductor, it has a lower ionisation energy, therefore

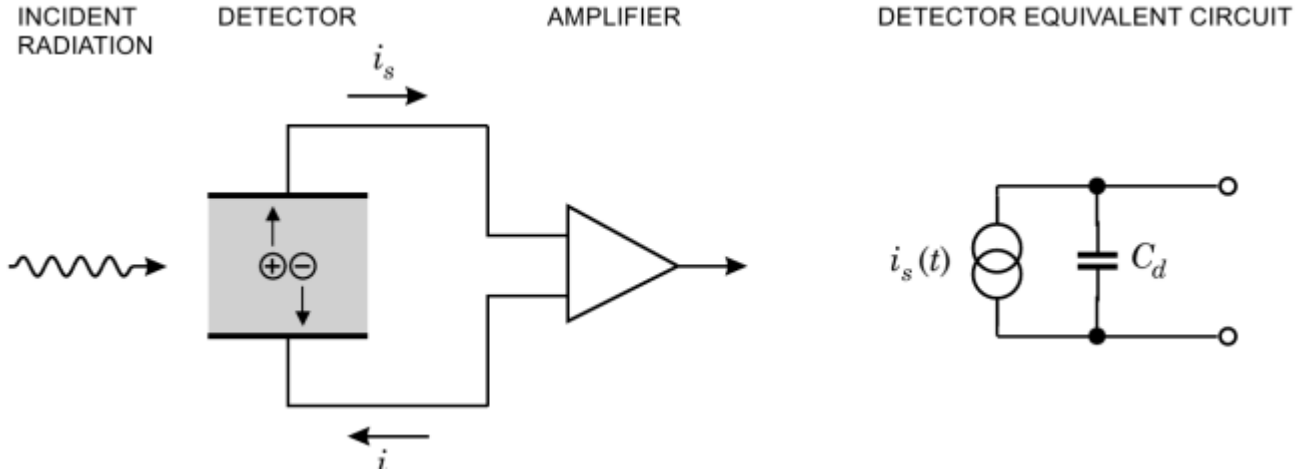


Figure 5.7: Process of ionisation and track detection [148]

there will be more ionisation due to this reduced threshold. In addition, the possibility of multiple scattering needs to be considered; multiple scattering can lead to erroneous tracks and therefore should be minimised where possible. In order to minimise multiple scattering, a larger radiation length  $X_0$  is required; this will be the case in lighter materials, therefore gaseous materials have a distinct advantage in this regard. Another very important factor is size; although the tracking detector is very important, it cannot be too large, otherwise that would impact on the effectiveness of other detector components, specifically the calorimeters. A hybrid system of gaseous and silicon as a TPC would be much larger than a purely silicon system, in order to offset the lower density of the gaseous material. The smaller size also provides another advantage to the purely silicon system; this would facilitate the use of a more powerful solenoid magnet. A more powerful magnet would affect momentum resolution in a positive manner, due to the relation between momentum resolution and magnet strength, which can be seen in equation 5.5:

$$\frac{\sigma(p_T)}{p_T} = \frac{\sigma_x p_T}{0.3BL^2} \frac{\sqrt{720}}{\sqrt{N+4}} \quad (5.5)$$

where  $p_T$  is transverse momentum, L is track length, and N is the number of measurements made along the track length, which is related to the number of layers used as part of the tracking detector. This further benefits the silicon detector, as each layer is thin, so there can be a large amount of layers in a small space, compared to the gaseous material which needs to be contained in a large area in order to be effective.

It has been decided that the best course of action is to utilise a tracking detector, based on these considerations, that is comprised solely of silicon strips.

### 5.6.2 Vertex Detector

The vertex detector is an important component in a different way to the tracking detector; it will provide details on the impact parameter, the charge of a track, and the vertex mass, according to [151]. While there are indeed several ways to construct a vertex detector (VXD), there are only considerations for the construction of a silicon VXD, particularly due to its robustness against the radiation bombardment that will occur due to its close proximity to the beam line, and therefore the collisions. A typical VXD can be seen in Figure 5.8.

### 5.6.3 Parameters

It is important to note that the basis for the detector parameters is derived from the parameters for SiD, the detector that is proposed for the ILC, many parameters of SiD can be found from [153]. The tracking detector will consist of layers of strips of single-sided silicon; it is inefficient to use double sided layers as this could simply result in more multiple scattering, which as previously mentioned, is very much undesirable. These strips extend outwards for approximately 1m, starting from an inner radius of 20cm, and ending at 112.4cm; this is a compromise to allow the calorimeters to work effectively, while still providing enough tracking data, and maintaining an effective momentum

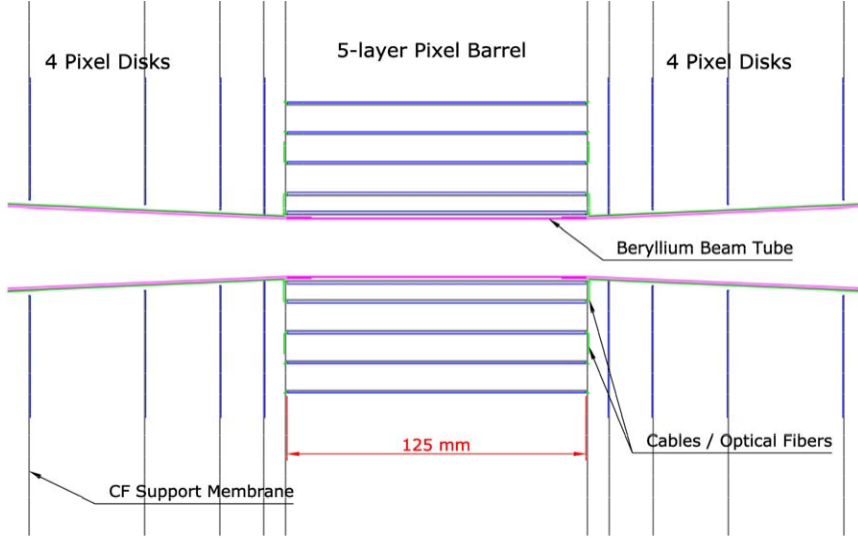


Figure 5.8: An outline of a typical vertex detector [152]

resolution. There will be specifically 5 layers, giving essentially 25 layers of silicon for tracking purposes, again for the purposes of maximising momentum resolution.

Using these values, along with a magnetic field strength of 5.0T, all of which can be applied to equation 5.5, would provide a momentum resolution of approximately  $5 \times 10^{-5} \text{ GeV}$ , which is more than sufficient to remove the need for muon tracking within the muon detector, thus removing any requirement for an outer magnet similar to the ATLAS design.

While the efficiency varies with angle, due to the proximity of the tracking detector to the beam line, there should be a solid angle coverage that approximates to  $\cos \theta \sim 0.98$ , which would be more than sufficient for tracking significant events where necessary. Finally, the tracking detector would have a spatial resolution of around  $8 \mu\text{m}$ ; the lack of drift as a result of using silicon gives such a small value that is a huge aid in reconstructing the track.

The vertex detector, instead of using strips, would use silicon pixels in order to provide 3D readouts of the space points, which is imperative for tagging the tracks and identifying them effectively, which is one of the primary functions of a VXD. It will also extend outwards roughly 5cm, with an inner radius of 1.4cm that is significant as it remains close to the beam line in order to make the VXD most effective, without a significant drop in solid angle coverage as a result; this is aided by the magnetic field strength of 5.0T somewhat.

This inner radius also takes into account the possibility of damage as a result of pair production from beamstrahlung, as described in Section 4.6. High energy electrons and positrons can cause serious damage to the VXD, due to the close proximity to the beam line. A compromise was required, because impact parameter and therefore spatial resolution are affected if the inner radius is further from the beam line, greatly reducing the effectiveness of the VXD. This could not be resolved by increasing the size of the VXD either, as this would either limit the size of the tracking detector, which would reduce performance to a slight extent, or the size of the outer calorimeters, which is not a viable option due to a large reduction in effectiveness if their size is reduced.

Finally, the vertex impact parameter is as follows:

$$\sigma r_\phi = \sigma r_z = 5 \oplus \frac{10}{p \sin^{\frac{3}{2}} \theta} \quad (5.6)$$

where  $\sigma r_\phi$  is the azimuthal impact parameter resolution, and  $\sigma r_z$  is the longitudinal impact parameter resolution. These are considered equal due to the various correlations between the two resolutions. This results in a vertex spatial resolution of  $5 \mu\text{m}$ .

## 5.7 ECAL *written by Andrew Clarke and John Cotterill*

Electromagnetic calorimeters are used for detection of particles that interact via the electromagnetic interaction. More specifically, this involves electrons and photons. Muons pass virtually unimpeded through the detector due to their larger mass restricting the scattering by a nucleus. Additionally, charged hadrons pass through virtually undetected due to the selection of a material with an interaction length, the mean distance taken by a hadron through a material before it interacts, which is large. The detection mechanism of the ECAL is through the interactions with the electrons within the active medium. In comparison the hadronic calorimeter uses the interaction of the particles with the nuclei in the detection material.

Electromagnetic calorimeters can be of two forms: sampling and homogeneous calorimeters. Sampling calorimeters contain alternating strips of absorber and active media. Homogeneous do not have distinct strips as they are made of a single material which performs both absorption and detection processes. Figure 5.9 shows a schematic representation of a sampling ECAL.

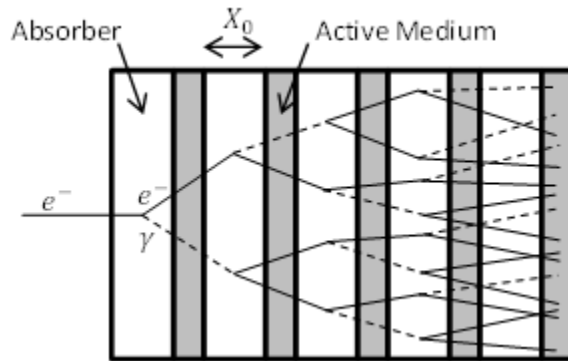


Figure 5.9: Schematic diagram of a sampling ECAL. White and grey regions represent the absorber and active medium respectively. Solid lines represent electrons and dashed lines represent photons produced through bremsstrahlung *designed by John Cotterill*.

When an incident electron passes close to the Coulomb field of a nucleus of the absorber it may interact via the bremsstrahlung process. Providing the resultant photon has sufficient energy, within the Coulomb field of a nucleus it may undergo pair production producing an  $e^+e^-$  pair. These new charged particles may then lose energy through further bremsstrahlung and pair production. This produces an electromagnetic shower and is shown in Figure 5.9.

The process continues giving rise to a shower of particles with a gradually decreasing average energy. This shower stops once the average energy of the particles drops below the critical energy of the medium. This critical energy is when the average photon energy from bremsstrahlung is insufficient to undergo pair production. The electrons and positrons then lose the remainder of their energy through ionisation and thermal excitation of atoms within the absorber - subsequently getting absorbed. Remaining photons lose their energy through Compton scattering.

### 5.7.1 ECAL Requirements *written by John Cotterill*

For selection of an appropriate absorber material the radiation length,  $X_0$ , must be considered. This length is the average distance required for the energy of the incident particle to be degraded to  $\frac{1}{e}$  of its original value. Having a short radiation length reduces the size of the calorimeter required for the detection of incident particles. This is advantageous for both cost and also bringing the components outside of the ECAL closer to the beam line. The small radiation length additionally brings the start of the electromagnetic shower closer to the inner most part of the calorimeter. This consequently reduces any wasted area. Contrastingly, a large interaction length must be chosen in order to reduce the number of hadronic interactions beginning in the ECAL region before reaching the HCAL.

The Molière radius is an additional consideration for the material of the absorber. Minimization of this value improves the shower position resolution of the calorimeter as the transverse size of the shower is reduced. This

means any showers are contained within a smaller volume and are consequently easier to separate.

The ability to resolve separate showers is also governed by the pixel size of the active medium. An active medium with a high pixel granularity/segmentation supports the ability to resolve closely spaced showers. Should larger pixels be used, showers of spacing smaller than the pixel size would not be possible to be resolved as separate. This would cause difficulty in identifying an energy deposition within the ECAL with a tracked particle in the tracker. Consequently, reconstruction of the invariant mass of the particle before decay would be affected.

The achievable momentum resolution must be considered for the selection of an appropriate calorimeter type. The momentum resolution is given by the Gluckstern formula (equation 5.5). This is a particularly important factor in the choice of active medium.

Achievable response times must be considered for the technology of choice, particularly for the high frequency collisions chosen to be performed at LEPIC. Though we are likely to obtain multiple collisions per response time for the detector, this is likely to have little effect on our results.

The final considerations are resistance to radiation damage and cost. The high luminosity and energy of the beams being used means that there will be a large flux of particles with high energy on the ECAL. It is therefore important to select materials which will be able to withstand such fluxes present at LEPIC. In terms of the cost of the electromagnetic calorimeter, though the thickness of the calorimeter is not large, the typical materials used can be expensive. It is therefore favourable to choose materials which are cost effective but support the requirements of the investigations being performed.

### **5.7.2 Homogenous vs Sampling *written by John Cotterill***

The use of separate layers in a sampling calorimeter results in the potential for some energy to be deposited in the absorber. Consequently, the entirety of the energy of the incident particle or photon is not detected and this detrimentally affects the energy resolution. For this reason, a homogenous calorimeter is advantageous. However, a sampling calorimeter has the advantage of allowing the selection of absorption and active media separately. For example, the absorption medium can be selected to be dense – producing an effective shower within a smaller volume – without considering its effectiveness as an active medium. Similarly, there is more freedom of choice for an appropriate active medium fulfilling all requirements such as fine pixel granularity.

It is important for each detector system to be as close to the beam line as possible in order to reduce energy losses before detection. The high energies being probed at LEPIC and consequently high energy particles incident on the detectors results in a requirement of very compact construction. It is for this reason that a sampling calorimeter will be more favourable due to the separate material selection available.

### **5.7.3 ECAL Selection *written by John Cotterill***

#### **5.7.3.1 Scintillation Calorimeter [155]**

Scintillation calorimeters operate through the detection of light emitted from the track of ionisation caused by the particle. They typically use plastic for the active medium and consequently have a lower cost of production. The ease of manufacturing of this material additionally allows the required segmentation of the calorimeter to be achieved easily. Fast response times are characteristic of this material due to the detection mechanism which also gives rise to an easily detectable light signal. Despite the ease of the manufacturing process, nonuniformities within the medium are produced which effects the light collection at a photomultiplier. This increases the constant term in the equation for the resolution and is therefore unfavourable for high resolution requirements.

#### **5.7.3.2 Liquid Calorimeter [155]**

Liquid calorimeters can operate at room temperature or cryogenic temperatures depending on the system. Systems at room temperature suffer from radiation damage which is detrimental to the results. Additional issues arise from

the difficulty in obtaining the necessary purity. To maintain the purity to a sufficient level a purification system must be included. Cryogenic liquid calorimeters are more resistant to radiation damage and have a stable response time. However, the operation of these systems at cryogenic temperatures requires a cryostat which must also be contained within the detector system similarly to the purification system. This cryostat/purifier is the source of an effective dead layer of the detector as no detection will take place within this region. Interactions may occur within this region which would consequently affect the perceived energy of the particles incident on the calorimeter itself.

### 5.7.3.3 Solid-State Calorimeter [155]

Solid-state calorimeters tend to be made with silicon as the active medium. This is because of the lower energy required to create an information carrier (electron-hole pair) within the material. 3.6eV is required to generate an electron-hole pair for silicon in comparison to the order of 100eV required for typical scintillation calorimeters [156]. This means that the active medium has a greater precision of energy detection. Again in comparison to gas calorimeters the active medium is much denser and consequently has a Molière radius significantly lower. This is advantageous for the whole detection system as the ECAL can be contained within a smaller volume. This system has been chosen despite the increased cost for such crystals for the larger resolution in the smaller volume.

### 5.7.4 Resolution and Efficiency *written by Andrew Clarke*

The equation for the energy resolution of a calorimeter, shown in equation 5.7, is dependent on three terms. Firstly there is a stochastic term related to statistical fluctuations, denoted as  $a$  in equation 5.7. The second term is constant and is due to the detector being non-uniform and uncertainty due to the calibration. The term is represented by  $b$  in equation 5.7. There is an electronic noise term, shown as  $c$  in equation 5.7.

$$R = \frac{\sigma(E)}{E} = \frac{a}{\sqrt{E}} \oplus b \oplus \frac{c}{E} \quad (5.7)$$

Equation 5.7: The energy resolution for a calorimeter.  $R$  is the resolution.  
 $E$  is the energy of the particle.  $\sigma(E)$  is the error on the energy of the particle.

Table 5.1 shows the energy resolution for electromagnetic calorimeters made of varying materials. Equation 5.7 is used in the computer program DELPHES, along with calorimeter sizes to determine the resolution of the detector. There are contributions from other parts of the detector. The data in Figure 5.1 was used as a guide to working out the size of the detector and also the materials used.

The efficiency of the electromagnetic calorimeter will be about 98% in the main barrel of the detector and about 95% in the end caps. To achieve this efficiency we will layer the detector in such a way that any inactive regions of the detector do not overlap. This means that when any detectable particle that enters the calorimeter and is not detected in one layer then it will be detected in the subsequent layer. There is very little chance that a detectable particle will go through the calorimeter without being detected leading to the high efficiency.

### 5.7.5 Parameters

To satisfy the requirements described above, silicon has been chosen for the active medium and tungsten for the absorber. Though expensive, silicon supports manufacturing of thin layers which is suitable for the construction of a compact calorimeter with many layers. A large number of layers for a fixed calorimeter depth and magnetic field strength results in an improved momentum resolution as given in equation 5.5. Sufficient pixel granularity can additionally be obtained with  $5 \times 5\text{mm}^2$  pixel sizes being achievable with present technology [143]. Tungsten with its small radiation length, 3.504mm, and Molière radius, 9.327mm, make it suitable for the absorption medium. This radiation length assists in initiating the shower towards the inner most layers of the calorimeter which reduces wasted space. Showers are additionally contained within small regions due the small Molière radius. As these materials are also proposed for the investigations at ILC then they are believed to be suitably radiation resistant for the investigations at LEPIC over 5 years.

The energy resolution of the ECAL is given in equation 5.8. The energy resolution cannot be calculated by

Table 5.1: Typical energy resolutions for an electromagnetic calorimeter. All energies are in GeV. [22]

Technology (Experiment)	Depth	Energy resolution	Date
NaI(Tl) (Crystal Ball)	$20X_0$	$2.7\%/\sqrt{E}^{1/4}$	1983
Bi <sub>4</sub> Ge <sub>3</sub> O <sub>12</sub> (BGO) (L3)	$22X_0$	$2\%/\sqrt{E} \oplus 0.7\%$	1993
CsI (KTeV)	$27X_0$	$2\%/\sqrt{E} \oplus 0.45\%$	1996
CsI(Tl) (BaBar)	$16-18X_0$	$2.3\%/\sqrt{E}^{1/4} \oplus 1.4\%$	1999
CsI(Tl) (BELLE)	$16X_0$	1.7% for $E_\gamma > 3.5$ GeV	1998
PbWO <sub>4</sub> (PWO) (CMS)	$25X_0$	$3\%/\sqrt{E} \oplus 0.5\% \oplus 0.2/E$	1997
Lead glass (OPAL)	$20.5X_0$	$5\%/\sqrt{E}$	1990
Liquid Kr (NA48)	$27X_0$	$3.2\%/\sqrt{E} \oplus 0.42\% \oplus 0.09/E$	1998
Scintillator/depleted U (ZEUS)	$20-30X_0$	$18\%/\sqrt{E}$	1988
Scintillator/Pb (CDF)	$18X_0$	$13.5\%/\sqrt{E}$	1988
Scintillator fiber/Pb spaghetti (KLOE)	$15X_0$	$5.7\%/\sqrt{E} \oplus 0.6\%$	1995
Liquid Ar/Pb (NA31)	$27X_0$	$7.5\%/\sqrt{E} \oplus 0.5\% \oplus 0.1/E$	1988
Liquid Ar/Pb (SLD)	$21X_0$	$8\%/\sqrt{E}$	1993
Liquid Ar/Pb (H1)	$20-30X_0$	$12\%/\sqrt{E} \oplus 1\%$	1998
Liquid Ar/depl. U (DØ)	$20.5X_0$	$16\%/\sqrt{E} \oplus 0.3\% \oplus 0.3/E$	1993
Liquid Ar/Pb accordion (ATLAS)	$25X_0$	$10\%/\sqrt{E} \oplus 0.4\% \oplus 0.3/E$	1996

the properties of the material but instead has to be obtained through experimentation or simulations. We have not carried out any simulations regarding this but have been able to use results from the CALICE collaboration who have investigated silicon tungsten ECALs similar to the one that we have proposed. Therefore the stochastic and constant term from the CALICE collaboration can be used as shown in equation 5.8 [158][159].

The electronic term can only be determined once the electronic part of the calorimeter has been built. The electronic terms from the ATLAS and CMS experiments were looked at as a guideline. We anticipate that the electronic term will be about 120MeV as was the case with the CMS experiment [160]. This will mean that the energy resolution is 1.74% for a particle with an energy of 150 GeV. The energy resolution increase with energy. Therefore the ECal has a sufficient energy resolution to distinguish between particles.

$$R = \frac{16.5\%}{\sqrt{E(\text{GeV})}} \oplus 1.1\% \oplus \frac{120\text{MeV}}{E(\text{GeV})} \quad (5.8)$$

It is proposed that the inner most layers of absorber have a smaller thickness than the outer layers. This design assists with the Higgs investigations at the centre-of-mass energy of 300GeV. The thinner layers support an increased sampling rate which improves the momentum resolution for such lower energy particles. Higher energy particles will pass into the region of lower sampling frequency, however the drop off of the shower with depth makes this less of an issue.

The layer dimensions proposed by the SiD ECAL ILC design [143] are 2.50mm of tungsten alternating with 1.25mm of silicon for the inner 20 layers of the calorimeter. The outer 10 layers have a 5.00mm tungsten thickness alternating with 1.25mm of silicon. These dimensions correspond to a maximum centre-of-mass energy of 1TeV and therefore require alteration for the studies at LEPIC to 6TeV. As the layer thicknesses have been achievable in manufacture for research and development for the ILC design then these dimensions will be duplicated. The alterations proposed are for the number of layers.

The depth of absorber required to absorb on average 98% of the energy of the incident particle is given by the

equation

$$\langle L_{98} \rangle = \frac{5}{2} \left( \ln \frac{E_0}{E_c} + c_i \right) \quad (5.9)$$

where  $E_0$  is the energy of the incident particle,  $E_c$  is the critical energy of the material and  $c_i$  is an additional constant which equals  $-0.5$  or  $+0.5$  for an incident electron or photon respectively [157]. In the case of the investigations at LEPIC, the ECAL must be capable of measuring 3TeV electrons and photons. The required depth of the absorber is then determined using the critical energy of tungsten of 7.68MeV [22] and assuming  $c_i$  is  $+0.5$  for the maximum length of calorimeter required. This results in an absorber of thickness equal to 34 radiation lengths.

The SiD ECAL ILC design uses half of the total tungsten thickness for the finer sampling of the inner layers with the remainder for the less frequent sampling. This same distribution of absorber between the two sampling frequencies has been assumed for the determination of the number of layers required at LEPIC. From the same layer thicknesses outlined above, 24 inner layers with the finer sampling and 12 outer layers with less frequent sampling are proposed. This gives a total size for the ECAL of 16.5cm.

## 5.8 HCAL written by Daniel Hatton

### 5.8.1 Hadronic Showers

Hadronic showers occur due to interactions between hadrons and the nuclei in the calorimeter material. There is a considerable amount of difficulty in describing hadronic showers in detail. However, there are some universal features. Hadronic interactions in a material are characterised by the nuclear interaction length of the material [161] (here denoted  $\lambda_I$ ). The overall thickness of the calorimeter is determined in terms of  $\lambda_I$ . However, it is not just the nuclear interaction length that is important for hadronic calorimetry. Hadronic interactions will produce pions most often due to their small masses. Neutral pions will rapidly decay into two photons. This leads to an electromagnetic component of any hadronic shower [161]. In order to be sensitive to the smaller electromagnetic cascades, the material needs to be sampled on a scale of radiation lengths rather than the, typically, considerably larger interaction length  $\lambda_I$ . For example the ATLAS detector uses iron in the barrel calorimeter sampled every radiation length with scintillator tiles [162].

Resolution in hadronic calorimeters is worse than in electromagnetic calorimeters. This is due to several factors. One is the relative sizes of the showers. Hadronic showers happen over larger distance scales but have components that develop electromagnetically. There is therefore difficulty in observing the shower over these two different length scales. Another factor is due to the complexity of the hadronic shower. Hadronic showers contain delayed energy deposits. These arise from hadrons interacting with nuclei and leaving them in an excited state. The nucleus will then de-excite depositing energy in the calorimeter [161]. In a collider with high repetition frequency (as required for high integrated luminosity) this means that this energy is deposited in later events.

The issue of the depth required for the absorption of a jet is difficult and requires experimental data and simulations. While the collider designed in this project will go to higher energies than other currently proposed colliders, after a certain depth in the calorimeter the shower begins to decrease. This indicates that large increases in depth over other high energy linear  $e^+e^-$  colliders should not be necessary. CLIC, operating at similar energies without a 6 TeV run, plans to have a hadronic calorimeter  $7.5 \lambda_I$  in depth (with  $1 \lambda_I$  in the ECAL) [163]. With the 6 TeV run planned in this project this number should be increased. Whizard simulations, using the PYTHIA hadronisation procedure, of  $W^+W^-$  and  $ZZ$  production at 1 TeV, 3 TeV and 6 TeV indicated that while the maximum energy of the hadrons in the showers did increase with centre of mass energy it was only by a relatively small amount and the majority of the hadrons still fell below 300 GeV. See Figure 5.10. This indicates that a small increase in depth should suffice. For these (and dimensional) reasons a depth of  $9 \lambda_I$  was chosen.

The two component nature of a hadronic shower causes problems for the resolution of the detector. The detector should respond in proportion to the energy of the detected particle. However, the proportionality will be different for the electromagnetic and hadronic components of the shower. This is due to energy loss effects such as the break up of nuclei in the absorber or the emission of slow neutrons that will not be detectable [161, 168]. One method of solving this problem is to chose materials to achieve  $\frac{e}{h}$  (the ratio of electromagnetic to hadronic response) as close to 1 as possible. The canonical reference for such a compensating detector is that of the ZEUS experiment [170, 171]. In this case the absorber material used was uranium. In uranium the slow neutrons that

cannot be detected induce fission which can be detected. The high Z material also absorbs a large proportion of the electromagnetic component meaning that less is deposited in the active medium. For the large detector being built here such an unstable and expensive material would not be practical. This leaves software compensation techniques as the leading option to improve resolution. This involves the use of algorithms to give different weights to electromagnetic and hadronic components. The two can be separated as the radiation length is considerably smaller than the interaction length (in the majority of materials) and the electromagnetic component therefore proceeds faster [168]. This leads to a higher energy density for the electromagnetic part.

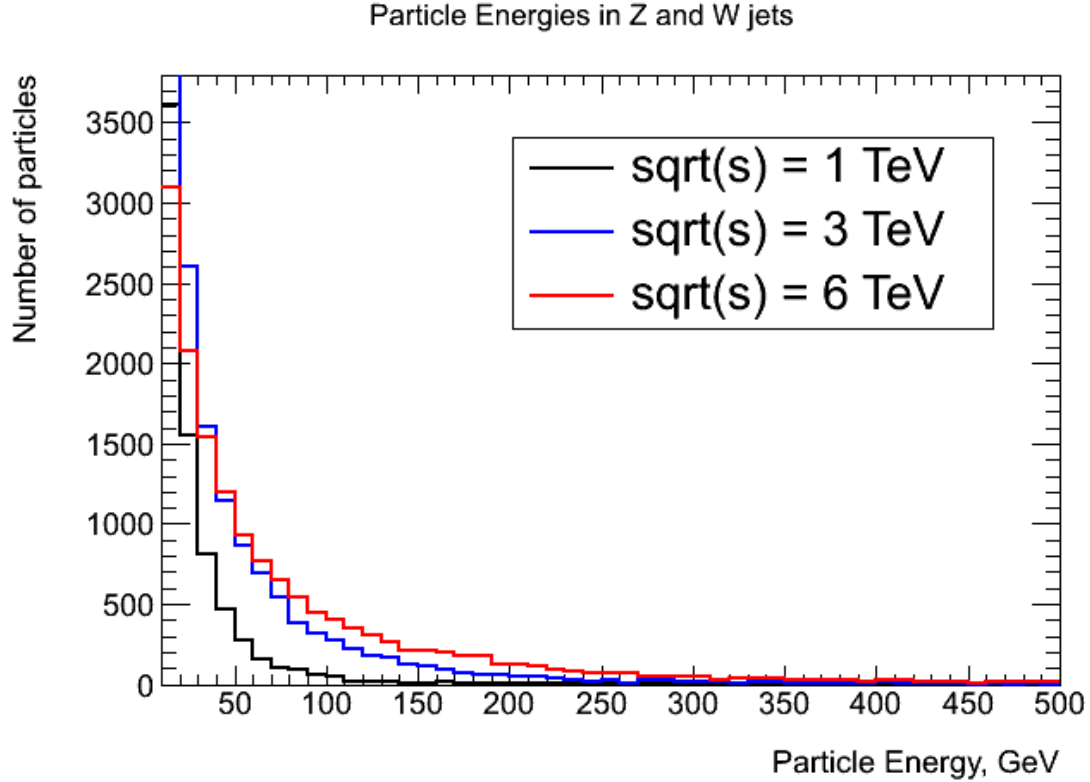


Figure 5.10: Plot of constituent particle energies in jets from 1000  $W^+W^-$  and  $ZZ$  events at  $\sqrt{s} = 1, 3$  and  $6\text{TeV}$ .

### 5.8.2 Particle Flow Algorithm Calorimetry

Particle Flow Algorithm (PFA) calorimetry attempts to significantly improve hadronic calorimeter energy resolution. The method relies on measurements made in the tracking chambers and electromagnetic calorimeters to reconstruct the paths of individual particles within hadronic jets. The momentum resolution obtained in tracking chambers is typically better than in hadronic calorimeters so if particles in the calorimeter can be traced back to the tracking chamber those momentum measurements can be used. Neutral hadrons will not be detected in the tracking chamber so their energy needs to be measured in the calorimeter. This method requires a finely granulated active medium to resolve deposits from individual particles. Both CLIC and ILC intend to follow the PFA paradigm [163, 164].

### 5.8.3 Materials

The absorber materials in the barrel being considered for the ILC and CLIC are steel and tungsten respectively [163, 164]. Tungsten can allow for a more compact design as it has an interaction length of 9.95 cm as opposed to 16.8 cm in steel. However, the radiation lengths are 1.76 cm and 0.35 cm respectively [22]. This means that if sampling is to be maintained at approximately every interaction length, tungsten calorimeters can be thicker than steel calorimeters with an equal sampling rate. The ideal material to use for the absorber would therefore be steel. Steel also has the advantage that the time taken to record the energy deposited in the calorimeter is shorter than

in tungsten. GEANT4 simulations done for the CLIC Conceptual Design Report indicate that in steel 90% of the energy can be recorded in approximately 6 ns while in tungsten it takes approximately 20 ns to record only 80% of the energy [163].

There are several options for the active medium currently being studied by the CALICE collaboration [165] for use in future linear  $e^+e^-$  colliders. The main differences in the technologies is whether the readout will be analog or digital. That is whether the energy deposited in the calorimeter will be measured or just the number of counts. The latter technology is clearly only an option for use in conjunction with PFA methods.

Two main areas of study are scintillating tiles (analog) and gaseous detectors such as resistive plate chambers (digital) [170]. The gaseous detectors can be made more efficient and with higher granularity but apart from that there is not much to distinguish the two other than their analog or digital nature. The scintillating tile option is also more researched and the analog readout could improve the resolution of the calorimeter, although reading out the larger amount of data recorded will take longer. A digital HCAL may suffer from pile-up as two simultaneous hits would be registered as one in a digital detector, whereas an analogue detector would record the energy deposited by every incident particle. The HCAL will therefore use scintillating tiles as the active medium, with fine granularity so that PFA techniques can be used. CALICE have constructed a prototype high granularity scintillating tile calorimeter with  $3\times 3\text{ cm}^2$  readout pads in the central region [167]. The cavities containing the scintillating tiles will be taken to be 6.5 mm deep as they are in the CLIC conceptual design report. The tiles themselves can be made to be  $\sim 3$  mm thick [164] but extra room is required for electronics.

#### 5.8.4 Resolution

A benchmark standard for HCAL energy resolution, used by both the ILC and CLIC, is the separation of W and Z mass peaks obtained from reconstructing the invariant mass of their jet decay products [163, 164]. CLIC aims for a 3.5% jet energy resolution in order to obtain a  $2.5\sigma$  separation of the mass peaks for jets up to 1 TeV in energy [163]. The relation of this jet resolution to the energy resolution equation used by Delphes for individual particles is complicated and requires detailed simulations that were not performed here. This is because, in PFA calorimetry, the best resolution measured in any part of the detector is used for each particle and this varies with the energy of the particle. The resolution in the HCAL decreases with energy while in the tracker it increases (see Section 5.6) so the HCAL will provide better resolution for more energetic particles. Analysis used by CLIC indicates that to achieve a  $2.5\sigma$  separation would require a stochastic term  $\lesssim 30\%$  [169].

With software compensation techniques the CALICE collaboration has produced a prototype steel and scintillating tile calorimeter with a stochastic term of 45% [168]. This was the value entered into the Delphes card used in event simulations and will be the target for this HCAL design.

#### 5.8.5 Parameters

High granularity scintillating tiles with  $3\times 3\text{ cm}^2$  readout pads will be used to allow for PFA techniques with the aim of reducing the effective stochastic term in the energy resolution to  $\sim 30\%$ . This should comfortably accommodate the SUSY search requirements discussed above (a particular case being the distinguishing of 225 GeV and 300 GeV jets). The requirement of W and Z invariant mass reconstruction should allow good enough jet reconstruction for Higgs studies as well. Steel will be used as the absorber because its relatively large radiation length allows frequent sampling. Alternating layers of steel and scintillating tiles with a total of 75 steel layers with thickness 2 cm will be used to give approximately 8.9 interaction lengths in depth. This will give a depth of 1.99 m, depending on the thickness of the active layers. The energy density of a shower decreases further into the calorimeter past a certain point [161]. This means that further into the detector the sampling rate can be reduced. This could be done if spacial or expense concerns required a restriction. The end caps also need to provide good energy resolution. To achieve this a similar design to CLIC will be followed with steel and scintillating tiles ideally sampling as often as the barrel which should provide a similar energy resolution [163]. The coverage should be extended to  $6\eta$  to study the high  $\eta$  jets produced in SUSY searches (see Section 3.4). Twelve azimuthal modules will be used as in the ILC design [164]. The high granularity of the scintillating tiles should allow for sufficient angular resolution.

## 5.9 Muon System *written by Russell Turner*

Due to their long lifetime and high level of penetration, muons can easily escape both of the calorimeters of the detector. Muons are quite unique in this behaviour, so they can easily be identified if a final system of detectors is used in the outer layer of the detector that tracks the motion of particles which escape. Since the nature of this system is based around particle identification rather than measurement of energy or momentum, the tracking resolution only needs to be good enough to match the outer tracks with tracks in the main tracker, where the momentum is measured. This means that the system can be built outside of the solenoid producing the magnetic field. The main source of error for this system arises from pions that escape from HCAL, since they could be misidentified as muons, so the system needs to be designed to minimise this misidentification. Since the solenoid has a length of  $15m$  and an outer radius of  $3.5m$ , the total surface area of detectors needed will be very large. This means that the detector material has to be quite cheap.

### 5.9.1 Design

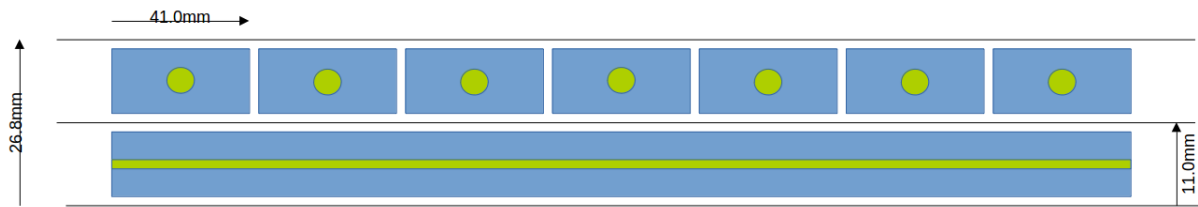


Figure 5.11: Schematic Diagram of one detector layer

First we will look at the technology to be used to detect the particles. For the uses described above, the technology needs to be able to cover a large area due to the number of layers that will be needed and the high radius of the barrels at this point. For this reason, polystyrene scintillating strips will be used. The benefit of using polystyrene strips is that it is much cheaper than other detector materials such as silicon. Each of these strips will be extruded such that the centre can hold a wavelength shifting fibre. These fibres will then transmit the scintillation photons to an array of photodiodes that performs the job of a photomultiplier, i.e. converting the scintillation photons into an electrical signal, at the end of each strip. The WLS fibre will be chosen to maximise the efficiency of the photomultiplier. Finally, the strips will be arranged in orthogonal planes, so that the position of the particles that pass through can be measured in two dimensions at each layer. In the barrel, one of these planes will be parallel to the beam line and one will be axial around it. In the endcap they will simply be vertical and horizontal. These planes will be separated by sheets of aluminium, which is transparent to muons, and the strips will be given a coating of reflective  $TiO_2$  to prevent the movement of scintillation photons between strips. A schematic diagram of this design can be seen in Figure 5.11. With this design, a particle's position can be measured with a precision of  $\pm 2.05cm$ .

Using several layers of the technology described above, the trajectory of particles that leave the inner parts of the detector can be measured. However, this does not solve the issue of misidentifying charged pions as muons. To counteract the issue, layers of steel can be inserted in between the detector layers. These steel layers are important because pions will be absorbed in steel, while muons will penetrate all the steel layers and pass through every detector layer. Requiring that the particle penetrate the equivalent of about 8 nuclear interaction lengths of steel is sufficient to reduce the misidentification fraction to 0.25%. This design is based on the proposed design of SiD at the ILC [143].

With this in mind, the design, for both the endcaps and the barrel, is to have ten layers of 18cm thick steel (so that each layer corresponds to about one nuclear interaction length). These steel layers will alternate with layers of detector planes as described earlier. This design can be seen in Figure 5.12. The thickness of each steel layer being slightly more than a nuclear interaction length allows the photomultipliers to be cased within the steel.

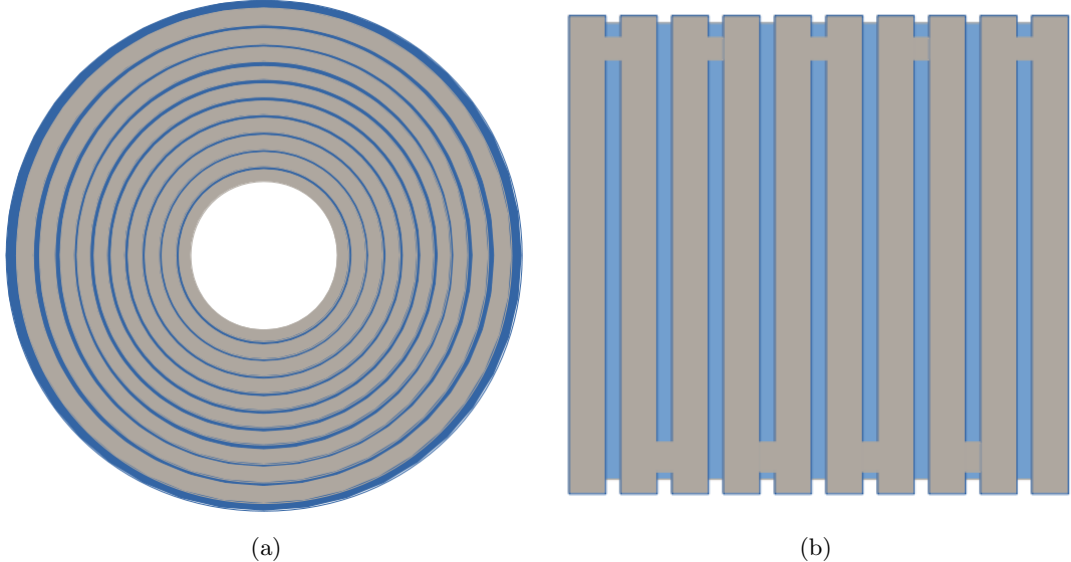


Figure 5.12: Basic design of (a) the barrel and (b) the endcap muon system (not to scale)

### 5.9.2 Parameters

The total thickness of the system with this design is  $206.8\text{cm}$ . Since the nuclear interaction length is the mean distance a hadron can travel without being absorbed [172], the fraction of pions that make it through all the layers of steel can be expressed as

$$\frac{N}{N_0} = e^{-\frac{L}{x_0}} \quad (5.10)$$

which, with the total length of  $180\text{cm}$  and steel's interaction length of  $16.77\text{cm}$ [22], gives the muon system a misidentification fraction of  $2.18 \times 10^{-3}\%$ .

The largest contributor to the response time is the time it takes for the photons to reach the photomultiplier. For a strip of length  $L$ , this can be estimated as

$$t \approx \frac{L}{c} \quad (5.11)$$

For the strips parallel to the beam line, and those in the endcap, this can be minimised simply by placing a photomultiplier at either end of the strip. However, in the axial strips, due to layers further out having a longer circumference to cover, further out layers will need more photomultipliers to maintain an acceptable time resolution. The spacing will be chosen to maintain a response time of  $\leq 20\text{ns}$ .

The solenoid has an outer radius of  $3.5\text{m}$ , so naturally this will also be the muon system's inner radius. Since the thickness of the system is  $206.8\text{cm}$ , the outer radius of the system will be  $5.57\text{m}$ . The endcaps will be discs of radius  $4.0\text{m}$ , to ensure the entire range of pseudorapidity is covered. With this design, the total surface area of muon detectors comes to approximately  $5400\text{m}^2$ .

## 5.10 Time Resolution *written by Adrian Cross*

The current bunch separation of the collider is  $20\text{ns}$  whereas the time resolution of the overall detector is  $\sim 200\text{ns}$  due to electronic effects. This means that approximately ten interactions will have to be integrated over. Table 5.2 shows the number of events which occur within this time frame. The instantaneous luminosity is assumed to be  $1.59 \times 10^{-2} \text{fb}^{-1}\text{s}^{-1}$  at  $1\text{TeV}$ , for the purposes of this calculation.

Table 5.2: Rate of Higgs producing mechanisms at 1TeV with an instantaneous luminosity of  $1.98 \times 10^{-4} fb^{-1}s^{-1}$

Parameter	Cross section ( $fb$ )	interaction rate ( $s^{-1}$ )	interactions per 200ns
$f\bar{f} \rightarrow t\bar{t}$ (s-channel gamma*/ $Z_0$ )	$2.12 \times 10^2$	$4.20 \times 10^{-2}$	$8.40 \times 10^{-9}$
$f\bar{f} \rightarrow H_0 Z_0$ (SM)	$1.74 \times 10^1$	$3.45 \times 10^{-4}$	$6.89 \times 10^{-11}$
$f\bar{f}' \rightarrow H_0 f\bar{f}'$ ( $Z_0 Z_0$ fusion) (SM)	$2.05 \times 10^1$	$4.06 \times 10^{-4}$	$8.12 \times 10^{-11}$
$f_1 f_2 \rightarrow H_0 f_3 f_4$ (W+ W- fusion) (SM)	$2.03 \times 10^2$	$4.02 \times 10^{-2}$	$8.04 \times 10^{-9}$
Total	$4.52 \times 10^2$	$8.95 \times 10^{-3}$	$1.79 \times 10^{-8}$

From table 5.2 it can be seen that there are very few interesting processes produced each second and therefore there is a small probability that more than one of these processes will occur within the time resolution. This is in part due to the clean nature of colliding fermions rather than hadrons.

## 5.11 Detector Card *written by Andrew Clarke and Adrian Cross*

The DELPHES program[173] requires a PYTHIA or WHIZARD input along with a detector card containing the properties of each component, as well as overall dimensions. This detector card was taken and edited to our specifications. The detector card based on the CMS detector is used because it has a similar setup to LEPIC, with different physical dimensions.

The parts of the card are edited for each specific component, starting with the solenoid in which the size, radius and length, have been altered along with the magnetic field strength.

In the tracker the momenta for each charged particle type, electrons, muons and charged hadrons, has been altered for LEPIC's tracker. In both of the calorimeters the energy resolution of each particle depends on their angle and these values have been altered to reflect our detector. These resolutions are entered according to equation 5.7

The jets within the original detector card are incorrectly described. The jets can include muons and electrons which as a group we would not define for jets. The card has been altered so that it defines muons and electrons and then defines the jets. This means the jets are better defined and only occur when there are hadrons in the final state. This is especially useful for reconstructing the Higgs as four jets in the final state is more difficult to resolve than two jets and two muons or electron.

## 6 The Five Year Plan

For our five years of data taking we shall be running at the four different centre of mass energies of 300GeV, 1TeV, 3TeV and 6TeV, with one year spent at each energy apart from 1TeV for which we shall be running for two years. A general outline of our five year plan is shown below in table 6.1. We are assuming that for 1 year of operation time we shall be able to measure data for three quarters of the year, with the other quarter of the time spent carrying out maintenance or any adjustments we wish to make.

Table 6.1: The general outline of our five year plan.

Year of Operation	1	2	3	4	5
Centre of Mass Energy (GeV)	300	1000	1000	3000	6000
Operating Sub-group	Higgs	Higgs	New Particles	New Particles	New Particles

The Higgs sub-group shall be running for the first two years of data taking; with the first year spent measuring the Higgs mass and verifying the Higgs spin and parity at a centre of mass energy of 300GeV and the second year spent measuring the Higgs branching fractions at the centre of mass energy of 1TeV. These two energies were chosen because at 300GeV the cross section for the production of the Higgs through the Higgs-Strahlung process peaks around this energy and the production of the Higgs through the W fusion and Z fusion processes is relatively low, leading to a smaller background of unwanted particles. We have also decided to run at 1TeV because at this energy the process of double Higgs production is possible and so this allows us to investigate the Higgs self-coupling constant along with the other decay schemes of the Higgs.

The number of seconds that the experiment needs to run for to obtain an integrated luminosity of  $L$  is given by Eq.6.1

$$T = \frac{L}{\varepsilon_1 \varepsilon_2 \times L_{inst}} \text{seconds}, \quad (6.1)$$

where  $L_{inst}$  is the instantaneous luminosity of the collider and  $\varepsilon_{1,2}$  is the probability that each beam has at least half the energy required to produce the desired particle in the final state. This efficiency assumes that there is no beam jitter so that the beams are stable and will collide with the maximum amount of beam profile overlap.

For the entirety of the SUSY section  $L$  was taken to be  $100\text{fb}^{-1}$  and instantaneous luminosity of the collider is  $1.98 \times 10^{-4}\text{fb}^{-1}\text{s}^{-1}$  as quoted in section 4.7.

By converting seconds into months and substituting values for  $L$  and  $L_{inst}$ , the run time equation can be simplified to,

$$T = \frac{0.1922}{\varepsilon_1 \varepsilon_2} \text{months}. \quad (6.2)$$

Simulations in GuineaPig suggest that the beam efficiency within 5% of the maximum beam energy is 0.1893 and 0.1961 for a  $\sqrt{s}$  of 1TeV, and 0.1775 and 0.1827 for a  $\sqrt{s}$  of 3TeV as quoted in table 4.2. This represents the lowest efficiency needed to obtain the results given in the section and in practise will be higher if the mass of particle being searched for is much less than the  $\sqrt{s}$  of the beam if they are produced singularly, or less than  $\sqrt{s}/2$  if they are produced in pairs. This obtains a run time at 1TeV of 5.18 months and at 3TeV of 5.93 months to obtain  $100\text{fb}^{-1}$  of data. So at each energy it is required that LEPIC runs for roughly two-thirds of the 9 month operational year. Running for a full year will obtain therefore roughly  $150\text{fb}^{-1}$  of data which will help to distinguish events from the background for 1TeV sleptons at the 3TeV run. To further separate results from the background, the beams can be polarised to suppress some standard model events. While this is helpful for the 1TeV run, with the benchmark that was used, it is vital for chargino searches at 3TeV. Running for a year with polarised beams at 1TeV and a year with polarised beams at 3TeV should be a more than adequate environment to test for SUSY sparticles.

Direct searches for the  $Z'$  will be made at all operational centre-of-mass energies over the 5 year period. These searches will attempt to locate a resonance peak in the cross section of the di-muon decay mode after direct production of the  $Z'$ . Should a resonance peak not be obtained, indirect searches will be performed at 6TeV for a period of 1 year (operational time of 9 months). The precision measurements of the di-muon cross section at this energy

will examine deviations from the standard model predictions. If a deviation is observed then the  $Z'$  boson may be inferred to exist. Alternatively, an increased lower limit of the  $Z'$  mass can be set.

## 7 Conclusion by Dwayne Spiteri, Lucy Bignell, Andrew Clarke, Adrian Cross and Chris Francis

LEPIC is an 150km linear  $e^+e^-$  collider designed to confirm theoretical predictions of a Standard Model Higgs boson and search for new particles. Its detector has been designed to maximise the probability of success in this regard within a 5 year total run time.

Searches for the Higgs boson will be focused at centre of mass energies of 300GeV and 1TeV, which allows the study of the couplings of the Higgs to other particles and itself. The aim of LEPIC will be to find the mass of the Higgs boson to a precision of 0.05GeV and confirm the spin and parity to be  $J^P = 0^+$ . However, the main focus of the 2 year run will be centred on investigating the branching fractions of the decays of the Higgs boson as these values are predicted accurately by the Standard Model. This will then allow us to confirm theoretical predictions for a Standard Model Higgs boson.

In the clean leptonic environment there are possibilities to resolve slepton and chargino events from the background in the benchmarks used, if they exist. Higgs boson and squark production seem much less promising. It also seems likely that our collider will not reach sufficient energies to find direct evidence of Z primes as these could have masses upwards of 50TeV. However a plan for detecting these particles has been developed though direct and indirect searching methods.

The linear collider geometry has been chosen in order to limit energy losses and allow a maximum collision energy of 6TeV to be achieved for the probing of non-standard model particles. The deactivation of accelerating cavities along the main linac allows for additional centre of mass energies of 300GeV, 1TeV and 3TeV. The former two are useful for probing the Higgs boson and the latter two for supersymmetric processes. To help enhance the search for new physics in the third and fourth years of run time, polarised particle beams will be used to suppress standard model processes and thus help to distinguish supersymmetric and other exotic events from background.

A detector has been designed according to the specifications outlined in both the new particle and Higgs sections of this report. Each component of the detector has been designed with these specifications in mind. The various parameters have been calculated according to their dimensions, the technologies used within them, and the materials from which they are made. These parameters were then used to produce a detector card for use in detector simulations of physics processes.

## References

- [1] S. L. Wu, “Brief history for the search and discovery of the Higgs particle - A personal perspective,” Mod. Phys. Lett. A **29** (2014) 9, 1330027 [arXiv:1403.4425 [hep-ex]].
- [2] G. Aad *et al.* [ATLAS Collaboration], “Evidence for the spin-0 nature of the Higgs boson using ATLAS data,” Phys. Lett. B **726** (2013) 120 [arXiv:1307.1432 [hep-ex]].
- [3] G. Aad *et al.* [ATLAS Collaboration], “Observation of a new particle in the search for the Standard Model Higgs boson with the ATLAS detector at the LHC,” Phys. Lett. B **716** (2012) 1 [arXiv:1207.7214 [hep-ex]].
- [4] P. P. Giardino, K. Kannike, I. Masina, M. Raidal and A. Strumia, “The universal Higgs fit,” JHEP **1405** (2014) 046 [arXiv:1303.3570 [hep-ph]].
- [5] D. B. Chitwood *et al.* [MuLan Collaboration], “Improved measurement of the positive muon lifetime and determination of the Fermi constant,” Phys. Rev. Lett. **99** (2007) 032001 [arXiv:0704.1981 [hep-ex]].
- [6] M. Strassler, “The Known Particles — If The Higgs Field Were Zero,” Of Particular Significance (Online) (2011)
- [7] H. Yukawa, Proc. Phys. Math. Soc. Jap. **17** (1935) 48.
- [8] M. Strassler, “Why the Higgs Field is Necessary,” Of Particular Significance (Online) (2012)
- [9] M. Strassler “The Basic Idea,” Of Particular Significance (Online) (2012)
- [10] S. Dawson, hep-ph/9901280
- [11] “Higgs Discovery on the Brink, but is it THE Higgs?,” viXra (2012)
- [12] Evidence for the direct decay of the 125 GeV Higgs boson to fermions, CMS Collaboration. May 22 2014  
<http://www.nature.com/nphys/journal/v10/n8/full/nphys3005.html>
- [13] Evidence for the spin-0 nature of the Higgs boson using ATLAS data, ATLAS Collaboration (Georges Aad (Freiburg U.) et al.). Jul 4, 2013.  
<http://arxiv.org/pdf/1307.1432v1.pdf>
- [14] Looking for the Higgs at LHC, High Energy Physics Group Imperial College London CMS. Jul 24, 2008  
<http://www.hep.ph.ic.ac.uk/cms/physics/higgs.html>
- [15] Precise determination of the mass of the Higgs boson and studies of the compatibility of its couplings with the standard model, CMS Collaboration. 2014  
<http://cds.cern.ch/record/1728249?ln=en>
- [16] Higgs cross sections for European Strategy studies in 2012, CERN. Oct 27 2014  
<https://twiki.cern.ch/twiki/bin/view/LHCPhysics/HiggsEuropeanStrategy2012>
- [17] Study of the Mass and Spin-Parity of the Higgs Boson Candidate Via Its Decays to Z Boson Pairs, CMS Collaboration (Serguei Chatrchyan (Yerevan Phys. Inst.) et al.). Dec 2012.  
<http://arxiv.org/pdf/1212.6639v2.pdf>
- [18] Toward High Precision Higgs-Boson Measurements at the ILC, The Higgs Working Group, 2005  
<http://arxiv.org/pdf/hep-ph/0511332v2.pdf>
- [19] Measuring the spin of the Higgs boson, D.J. Miller et al., 2001  
<http://www.sciencedirect.com/science/article/pii/S0370269301003173>
- [20] LHC experiments join forces on the Higgs boson, CERN. Mar 18 2015  
<http://press.web.cern.ch/press-releases/2015/03/lhc-experiments-join-forces-zoom-higgs-boson>
- [21] T. Sjöstrand, S. Ask, J. R. Christiansen, R. Corke, N. Desai, P. Ilten, S. Mrenna and S. Prestel *et al.*, “An Introduction to PYTHIA 8.2,” arXiv:1410.3012 [hep-ph].
- [22] K. A. Olive *et al.* [Particle Data Group Collaboration], “Review of Particle Physics,” Chin. Phys. C **38** (2014) 090001.

- [23] H. Ono and A. Miyamoto, “A study of measurement precision of the Higgs boson branching ratios at the International Linear Collider,” Eur. Phys. J. C **73** (2013) 3, 2343 [arXiv:1207.0300 [hep-ex]].
- [24] S. Dittmaier, M. Kramer, Y. Liao, M. Spira and P. M. Zerwas, “Higgs radiation off top quarks in e+ e- collisions,” Phys. Lett. B **441** (1998) 383 [hep-ph/9808433].
- [25] J. Tian *et al.* [ILD Collaboration], “Measurement of Higgs couplings and self-coupling at the ILC,” PoS EPS -HEP**2013** (2013) 316 [arXiv:1311.6528 [hep-ph]].
- [26] F. Simon, “Prospects for Precision Higgs Physics at Linear Colliders,” PoS ICHEP **2012** (2013) 066 [arXiv:1211.7242 [hep-ex]].
- [27] Castanier et al. Higgs self coupling measurement in  $e^+e^-$  collisions at centre-of-mass energy of 500 GeV (2001)
- [28] Baer et al. Physics at the International Linear Collider (Feb 2013)
- [29] Rodriguez et al. The Triple Higgs Boson Self-Coupling at Future Linear  $e^+e^-$  Colliders (2008)
- [30] M. Strassler, “Decays of the Standard Model Higgs,” Of Particular Significance (Online) (2011) <http://profmattstrassler.com/articles-and-posts/the-higgs-particle/the-standard-modelhiggs/decays-of-the-standard-model-higgs/>
- [31] ”Beam-Beam Effects in Particle Colliders” presentation, M. Pivi, 1/3/15
- [32] ”Concept of Luminosity in Particle Colliders” presentation, W. Herr and B. Muratori, 1/3/15
- [33] ”Physics and Detectors at CLIC” presentation, P.Roloff, 24/1/15
- [34] A. Leike, S.Riemann, T. Riemann, ZZ’ Mixing in Presence of Standard Weak Loop Corrections, Theory Division, CERN, LMU-91/06, (1991)
- [35] J. Kang, P.Langacker, Z’ Discovery For Supersymmetric E6 Models, Department of Physics and Astronomy, University of Pennsylvania, UPR-1076-T, (2008)
- [36] W. Kilian, T. Ohl and J. Reuter, “WHIZARD: Simulating Multi-Particle Processes at LHC and ILC,” Eur. Phys. J. C **71** (2011) 1742 [arXiv:0708.4233 [hep-ph]].
- [37] G. Aad et al., Search for high-mass dilepton resonances in pp collisions at  $\sqrt{s} = 8\text{TeV}$  with the ATLAS detector, ATLAS Collaboration, Physical Review D 90, 052005, (2014)
- [38] J. Hauptman, Particle Physics Experiments at High Energy Colliders, John Wiley and Sons, 2011, pp 106, ISBN: 978-3-527-40825-2
- [39] H. H. Ku, Notes on the Use of Propagation of Error Formulas, Journal of Research of the National Bureau of Standards, Vol. 70C, No. 4, 1966
- [40] S. Weinberg, *The Quantum Theory of Fields Volume III*. Cambridge University Press, 2000
- [41] M. Drees, R. Godbole and P. Roy, *Theory and Phenomenology of Sparticles*. World Scientific Publishing Co., 2004
- [42] S. Weinberg, *Implications of dynamical symmetry breaking*. Physical Review D, 1976, Vol. 13(4), pp.974-996
- [43] L. Susskind, *Dynamics of spontaneous symmetry breaking in the Weinberg-Salam theory*. Physical Review D, 1979, Vol. 20(10), pp.2619-2625
- [44] A. Datta, B. Mukhopadhyaya and A. Raychaudhuri, eds., *Physics at the Large Hadron Collider*. Springer, 2009
- [45] ATLAS Experiment. 2015. *ATLAS Experiment - Public Results*. [Online]. [Accessed 20 March 2015]. Available from: <https://twiki.cern.ch/twiki/bin/view/AtlasPublic>
- [46] CMS Experiment. 2015. *CMS Physics Results*. [Online]. [Accessed 20 March 2015]. Available from: <https://twiki.cern.ch/twiki/bin/view/CMSPublic/PhysicsResults>
- [47] U. Ellwanger, J. F. Gunion and C. Hugonie, *NMHDECAY: A Fortran Code for the Higgs Masses, Couplings and Decay Widths in the NMSSM*. Journal of High Energy Physics, 2005, Vol.2005(02), pp.066-066

- [48] U. Ellwanger and C. Hugonie, *NMSPEC: A Fortran code for the sparticle and Higgs masses in the NMSSM with GUT scale boundary conditions*. Computer Physics Communications, 2007, Vol.177(4), pp.399-407
- [49] U. Ellwanger, C.-C. Jean-Louis and A.M. Teixeira, *Phenomenology of the General NMSSM with Gauge Mediated Supersymmetry Breaking*. Journal of High Energy Physics, 2008, Vol.2008(05), p.044
- [50] D. Das, U. Ellwanger and Ana M. Teixeira, *NMSDECAY: A Fortran Code for Supersymmetric Particle Decays in the Next-to-Minimal Supersymmetric Standard Model*. arXiv:1106.5633 [hep-ph]
- [51] M. Muhlleitner, A. Djouadi and Y. Mambrini, *SDECAY: A Fortran code for the decays of the supersymmetric particles in the MSSM*. Computer Physics Communications, 2005, Vol.168(1), pp.46-70
- [52] W. Kilian, T. Ohl and J. Reuter, *WHIZARD: Simulating Multi-Particle Processes at LHC and ILC*. The European Physical Journal C, 2011, Vol.71(9), pp.1-29
- [53] M. Moretti, T. Ohl and J. Reuter, *O'Mega: An Optimizing matrix element generator*. arXiv: hep-ph/0102195-rev.
- [54] B. C. Allanach, et al. *SUSY Les Houches Accord 2*. Computer Physics Communications, 2009, Vol.180(1), pp.8-25
- [55] Particle Data Group. 2014. *Particle Data Group Summary Tables*. [Online]. [Accessed 22 March 2015]. Available from: [http://pdg.lbl.gov/2014/tables/contents\\_tables.html](http://pdg.lbl.gov/2014/tables/contents_tables.html)
- [56] SLHA File
- [57] <http://pdg.lbl.gov/2012/listings/rpp2012-list-z-boson.pdf>
- [58] <http://arxiv.org/pdf/hep-ph/9511275.pdf>
- [59] J. Kang, P. Langacker, Z' Discovery Limits For Supersymmetric E 6 Models (2004)
- [60] E. Accomando et al., Z' physics with early LHC data (2010)
- [61] B. Trocme, F. Ledroit, M. Schaefer Distinguishing Z' models in ATLAS (2005)
- [62] J-J. Blaising, J.D. Wells, Physics performances for Z' searches at  $\sqrt{s} = 3$  TeV and 1.4 TeV at CLIC (2012)
- [63] D. Hayden, C. Willis, and R. Brock, Z Prime: A Story (2013)
- [64] G. Aad et al., Search for high-mass dilepton resonances in pp collisions at  $\sqrt{s} = 8$  TeV with the ATLAS detector, (ATLAS Collaboration) (2014)
- [65] T.Reis, Search for new Massive Resonances in Dilepton Mass Spectra in pp Collisions at  $\sqrt{s} = 8$  TeV with CMS, (CMS Collaboration) (2014)
- [66] AN INTRODUCTION TO TECHNICOLOR, Kenneth Lane, (1994)
- [67] The Ideas of Particle Physics: An Introduction for Scientists, G. D. Coughlan, J.E.Dodd, 2nd Edition, Cambridge University Press (1991)
- [68] Technicolor, Francesco Sannino, 03/2012
- [69] S.S. AbdusSalam, B.C. Allanach, H.K. Dreiner, J. Ellis, U. Ellwanger, J. Gunion, S. Heinemeyer, M. Krämer, M. Mangano ,K.A.Olive, S. Rogerson, L.Roszkowski, M. Schlaffer, G. Weiglein, Benchmark models, planes, lines and points for future SUSY searches at the LHC, published 17/12/2011.
- [70] CMS collaboration, Precise determination of the mass of the Higgs boson and tests of compatibility of its couplings with the standard model predictions using proton collisions at 7 and 8 TeV, 30/12/2014.
- [71] ATLAS collaboration Measurement of the Higgs boson mass from the H->gamma gamma and H->ZZ\*->4l channels in pp collisions at center of mass energies of 7 and 8 TeV with the ATLAS detector 17/06/2014.
- [72] O. Buchmueller J. Marrouche, Universal mass limits on gluino and third-generation squarks in the context of Natural-like SUSY spectra, 05/02/2014.
- [73] B.C. Allanach, Comput. Phys. Commun. 143 (2002) 305-331, hep-ph/0104145
- [74] Wikipedia, “Neutralino,” <http://en.wikipedia.org/wiki/Neutralino>, (2015).

- [75] Wikipedia, "Chargino," <http://en.wikipedia.org/wiki/Chargino>, (2015).
- [76] S. Ambrosanio and B. Mele, "Neutralino production as SUSY discovery process at LEP-2," Phys. Rev. D **52** (1995) 3900 [[hep-ph/9503362](#)].
- [77] N. de Filippis, K. Desch, G. Grenier, C. Hensel, A. Perrotta and S. Rosier-Lees "Combined LEP Chargino Results, up to 208 GeV for low DM," LEP2 SUSY Working Group, [http://lepsusy.web.cern.ch/lepsusy/www/inoslowdmsummer02/charginolowdm\\_pub.html](http://lepsusy.web.cern.ch/lepsusy/www/inoslowdmsummer02/charginolowdm_pub.html), (2002).
- [78] B. Abbott *et al.* [D0 Collaboration], "Measurement of the high mass Drell-Yan cross-section and limits on quark electron compositeness scales," Phys. Rev. Lett. **82** (1999) 4769 [[hep-ex/9812010](#)].
- [79] K. Hagiwara, K. Hikasa and M. Tanabashi, "Searches for Quark and Lepton Compositeness,"
- [80] M. Drees, R. M. Godbole and P. Roy "Theory and Phenomenology of Sparticles," World Scientific Publishing Company, (2004). ISBN-981-02-3739-1
- [81] D. Green, "The Physics of Particle Detectors," Cambridge University Press, (2000).
- [82] <http://cms.web.cern.ch/news/recent-results-susy-searches-cms>, V. Martinez, B. Hooberman
- [83] Sibs Prasad Das, Amitava Datta and Monoranjan Guchait, *Four Body Decay of the Stop Squark at the Upgraded Tevatron*, 2001
- [84] <http://www.slac.stanford.edu/cgiwrap/getdoc/slacpub8934.pdf>
- [85] <http://uspas.fnal.gov/programs/JAS/JAS14RedaelliLecture.pdf>
- [86] [http://link.springer.com/chapter/10.1007/9783662085813\\_6](http://link.springer.com/chapter/10.1007/9783662085813_6)
- [87] <http://uspas.fnal.gov/materials/11ODU/collimation.pdf>
- [88] <http://accelconf.web.cern.ch/AccelConf/p07/papers/thpmn068.pdf>
- [89] <https://indico.cern.ch/event/87907/contribution/1/material/slides/0.pdf>
- [90] [http://pdg.lbl.gov/2014/AtomicNuclearProperties/HTML/titanium\\_Ti.html](http://pdg.lbl.gov/2014/AtomicNuclearProperties/HTML/titanium_Ti.html)
- [91] <http://citeseerx.ist.psu.edu/viewdoc/download?doi=10.1.1.382.6195&rep=rep1&type=pdf>
- [92] CLIC detector and physics study. CLIC FAQ. (2014). Available: <http://clicdp.web.cern.ch/content/clicfaq>. [Last accessed 26th Mar 2015].
- [93] RB. Appleby et al. The 2 mrad Crossing Angle Scheme for the International Linear Collider. (2008). Proceedings of EPAC08, Italy [EPAC No: MOPP005] Available: <https://accelconf.web.cern.ch/accelconf/e08/papers/mopp005.pdf>. [Last accessed 26th Mar 2015].
- [94] JT. Seeman. The Stanford Linear Collider. (1991). Report No. SLAC-PUB-5607. Available: <http://www.slac.stanford.edu/cgi-wrap/getdoc/slacpub5607.pdf>. [Last accessed 26th Mar 2015].
- [95] N. Walker. "ILC Design Overview". (2012). GDE Internal Cost Review FNAL 13-11-12. Available: <http://www.fnal.gov/directorate/ILCPAC/2012Dec/PACTDRrevfinalWalker.pptx>. [Last accessed 26th Mar 2015].
- [96] CLIC Seminar. (2010). CLIC Parameter List 3TeV. Available: <http://clic-meeting.web.cern.ch/clic-meeting/clictable2010.html>. [Last accessed 26th Mar 2015].
- [97] Synchrotron Radiation, W. Barletta, USPAS, 2009  
[http://uspas.fnal.gov/materials/09UNM/Unit\\_11\\_Lecture\\_18\\_Synchrotron\\_radiation.pdf](http://uspas.fnal.gov/materials/09UNM/Unit_11_Lecture_18_Synchrotron_radiation.pdf)
- [98] Insertion Devices - Slide 8, I. Reichel, USPAS, June 2012  
<http://uspas.fnal.gov/materials/12MSU/DampingRingsLecture4.pdf>
- [99] Superconducting cavities for accelerators, Dieter Proch. November 11 1997  
<http://uspas.fnal.gov/materials/05UCB/Proch.pdf>
- [100] Superconducting cavities for accelerators, Dieter Proch. November 1997  
<http://uspas.fnal.gov/materials/05UCB/Proch.pdf>

- [101] Magnetic Chicane Bunch Compressors, PBPL  
[http://pbpl.physics.ucla.edu/Research/Technologies/Magnets/Electromagnets/Dipoles/Chicane\\_Bunch\\_Compressors/](http://pbpl.physics.ucla.edu/Research/Technologies/Magnets/Electromagnets/Dipoles/Chicane_Bunch_Compressors/)
- [102] Accelerator Physics at LEP, D.Brandt, H.Burkhardt, M.Lamont, S. Myers and J.Wenninger, (2000)
- [103] TLEP, first step in a long-term vision for HEP, M. Koratzinos, A.P. Blondel et al, (2013)
- [104] <http://physics.nist.gov/cuu/Constants/Citations/Search.html>, Accessed on 12/03/2015
- [105] The CLIC Programme: Towards a Staged e+e- Linear Collider Exploring the Terascale : CLIC Conceptual Design Report, P. Lebrun, L. Linssen, et al, 08/08/2012
- [106] Paul Avery, Synchrotron Radiation in Particle Accelerators, (2013)
- [107] W.Chou Preliminary Conceptual Design of the CEPC-SPPC- (2015)
- [108] Report of the ICFA Beam Dynamics Workshop: Accelerators for a Higgs Factory: Linear vs. Circular, Alain Blondel, Alex Chao, Weiren Chou, Jie Gao, Daniel Schulte and Kaoru Yokoya, (2013)
- [109] The International Linear Collider beam dumps, R. Appleby, L. Keller, T. Markiewicz, A. Seryi, D. Walz, R. Sugahara, (2006)
- [110] Introduction to dump issues, R. Appleby, 2005 at Snowmass (2005)
- [111] ILC technical Design Report, Volume 4, Chris Adolphsen, Maura Barone et al, (June 2013)
- [112] CLIC Post-Collision Line and Dump, CLIC Post-Collision Team (including R. Appleby, A. Apyan, K. Elsener Barbara Dalena et al, (2010)
- [113] BACKGROUND AT THE INTERACTION POINT FROM THE CLIC POST-COLLISION LINE, M.D. Salt, R. Appleby, A. Apyan, K. Elsener, E. Gschwendtner, A.Ferrari, 23-28/05/2010.
- [114] The International Linear Collider Technical Design Report, Volume 4: Detectors
- [115] Polarimeters and Energy Spectrometers for the ILC Beam Delivery System, S. Boogert, A.F. Hartin et al., 07/10/2009
- [116] <http://home.web.cern.ch/about/engineering/radiofrequencycavities>, 22/02/15
- [117] "RF-accelerators: RF-cavities" presentation, W.A. Barletta, 22/02/15
- [118] "Superconducting RF Cavities for Particle Accelerators: An Introduction" presentation, I. Ben-Zvi, 01/03/15
- [119] High Gradient SRF Cavity with Minimized Surface E.M. Fields and Superior Bandwidth for the ILC, N. Juntong and R.M. Jones, 01/03/15
- [120] "Magnetic Fields and Magnet Design" presentation, J. Holmes, S. Henderson and Y. Zhang, 22/02/15
- [121] Fitzpatrick, Richard. The Larmor Formula. Relativity and Electromagnetism. [Online] 2nd February 2006. [Cited: 22nd March 2015.] <http://farside.ph.utexas.edu/teaching/em/lectures/node130.html>.
- [122] Steane, Andrew M. Relativity Made Relatively Easy. Oxford : Oxford University Press, 2012. ISBN: 978-0199662869.
- [123] Fitzpatrick, Richard. Radiation Losses. Relativity and Electromagnetism. [Online] 2nd February 2006. [Cited: 22nd March 2015.] <http://farside.ph.utexas.edu/teaching/em/lectures/node131.html>.
- [124] Wikipedia, "Beamstrahlung," <http://en.wikipedia.org/wiki/Beamstrahlung>, (2014).
- [125] D. V. Schroeder, "Beamstrahlung and QED backgrounds at future linear colliders," SLAC-0371, SLAC-371, SLAC-R-0371, SLAC-R-371.
- [126] C. Grah and A. Sapronov, "Beam parameter determination using beamstrahlung photons and incoherent pairs," *JINST* **3** (2008) P10004.
- [127] D. Schulte, "Beam-beam simulations with GUINEA-PIG," CERN-PS-99-014-LP, CERN-PS-99-14-LP, CLIC-NOTE-387, CERN-CLIC-NOTE-387.
- [128] CLIC Conceptual Design Report, Geneva (2012)

- [129] ILC TDR Volume 3.1:Accelerator- R&D in the Technical Design Phase (2013)
- [130] R.L Taylor Magnetic measurements of quadrupole focusing magnets at SLAC (1991) J.G Perez et al. Options for final focussing quadrupoles (June 2012)
- [131] P.N Burrows et al. Nanosecond-timescale intra-bunch-train feedback for the linear collider: Results of the FONT2 run, SLAC (2004)
- [132] T. Nishitani et al., Highly polarized electrons from GaAsGaAsP and InGaAsAlGaAs strained-layer superlattice photocathodes,” J. Appl. Phys. **97**, 094907 (2005).
- [133] Image from: <http://www.synchrotron.org.au/synchrotron-science/how-issynchrotron-light-created>
- [134] ILC electron and positron sources, Wei Gai, PAC review, KEK Japan, 2012
- [135] ATLAS Collaboration, “ATLAS central solenoid: Technical design report,” CERN-LHCC-97-21.
- [136] ATLAS Collaboration, “ATLAS barrel toroid: Technical design report,” CERN-LHCC-97-19.
- [137] ATLAS Collaboration, “ATLAS endcap toroids: Technical design report,” CERN-LHCC-97-20.
- [138] ATLAS Collaboration, “ATLAS magnet system: Technical design report,” CERN-LHCC-97-18.
- [139] A. Airapetian *et al.* ATLAS Collaboration, “ATLAS: Detector and physics performance technical design report. Volume 1,” CERN-LHCC-99-14, ATLAS-TDR-14.
- [140] American Magnetics Inc., “American Magnets,” <http://www.americanmagnetics.com/charactr.php> (2012).
- [141] Beyond Standard Model Phenomenology at the LHC, Priscila de Aquino, Springer Science & Business Media, Switzerland, 2013
- [142] M. Aicheler, M. Aicheler, P. Burrows, M. Draper, T. Garvey, P. Lebrun, K. Peach and N. Phinney *et al.*, “A Multi-TeV Linear Collider Based on CLIC Technology : CLIC Conceptual Design Report,” CERN-2012-007, SLAC-R-985, KEK-Report-2012-1, PSI-12-01, JAI-2012-001.
- [143] T. Behnke, J. E. Brau, P. N. Burrows, J. Fuster, M. Peskin, M. Stanitzki, Y. Sugimoto and S. Yamada *et al.*, “The International Linear Collider Technical Design Report - Volume 4: Detectors,” arXiv:1306.6329 [physics.ins-det].
- [144] G. Abbiendi *et al.* [OPAL Collaboration], “Precision luminosity for Z0 line shape measurements with a silicon tungsten calorimeter,” Eur. Phys. J. C **14** (2000) 373 [hep-ex/9910066].
- [145] H. Abramowicz *et al.*, “A Luminosity Calorimeter for CLIC,” 2009. Tech. Rep.. LCD-Note-2009-02
- [146] I. Sadehi, “Luminosity Measurement at the International Linear Collider,” 2008. Physics and Astronomy, Tel Aviv University
- [147] G. L. Bayatian *et al.* [CMS Collaboration], “CMS physics: Technical design report,” CERN-LHCC-2006-001, CMS-TDR-008-1.
- [148] H. Spieler, “Semiconductor detector systems,” Ser. Semicond. Sci. Tech. **12** (2005) 1.
- [149] A. Besson, “Vertex and Tracking Detectors at the ILC,” Vertex 2014. (Presentation)
- [150] S.S. Kapoor “Nuclear Radiation Detectors,” (1986).
- [151] Gregor, I.-M. 2009, arXiv:0901.2228
- [152] “Far Forward Tracking Requirements for the ILC,” <http://ifid.uv.es/vos/ilc/ilcFastForward/DetectorLayout.html> (2015)
- [153] Aihara, H., Burrows, P., & Oreglia, “SiD: Letter of Intent,” M. 2009, arXiv:0911.0006
- [154] R. L. Gluckstern, “Uncertainties in track momentum and direction, due to multiple scattering and measurement errors,” Nucl. Instrum. Meth. **24** (1963) 381.
- [155] C. W. Fabjan and F. Gianotti, “Calorimetry for particle physics,” Rev. Mod. Phys. **75** (2003) 1243.
- [156] G.F. Knoll, “Radiation Detection and Measurement,” John Wiley & Sons Inc., (2010).

- [157] R. M. Brown and D. J. A. Cockerill, “Electromagnetic calorimetry,” Nucl. Instrum. Meth. A **666** (2012) 47.
- [158] Daniel Jeans for the CALICE collaboration ,CALICE Silicon-Tungsten ECAL, Laboratoire Leprince-Ringuet – Ecole polytechnique – CNRS/IN2P3 .
- [159] CALICE Collaboration, Response of the CALICE Si-W Electromagnetic Calorimeter Physics Prototype to Electrons, 14/11/08, arXiv:0811.2354
- [160] Francesca Cavallari, Performance of calorimeters at the LHC, 2011 J. Phys.: Conf. Ser. 293 012001.
- [161] D. Green, *The Physics of Particle Detectors*. Cambridge University Press, 2000
- [162] W. W. Armstrong *et al.* [ATLAS Collaboration], “ATLAS: Technical proposal for a general-purpose p p experiment at the Large Hadron Collider at CERN,” CERN-LHCC-94-43.
- [163] CLIC Collaboration, *Physics and Detectors at CLIC: CLIC Conceptual Design Report*. arXiv:1202.5940 [physics.ins-det]
- [164] ILC Collaboration, *The International Linear Collider Technical Design Report - Volume 4: Detectors*. arXiv:1306.6329 [physics.ins-det]
- [165] CALICE Collaboration. 2015. *CALICE*. [Online]. [Accessed 20 March 2015]. Available from: <https://twiki.cern.ch/twiki/bin/view/CALICE/WebHome>
- [166] G. Drake, J. Repond, D. Underwood and L. Xia, *Resistive Plate Chambers for Hadron Calorimetry: Tests with Analog Readout*. Nucl. Instrum. Methods Phys. Res. A, 2007, Vol.578(1)
- [167] CALICE Collaboration, *Validation of GEANT4 Monte Carlo Models with a Highly Granular Scintillator-Steel Hadron Calorimeter*. Journal of Instrumentation, 2013, Vol.8(07), p.P07005
- [168] CALICE Collaboration, *Hadronic energy resolution of a highly granular scintillator-steel hadron calorimeter using software compensation techniques*. JINST 7 P09017 (2012)
- [169] M. A. Thomson, *Particle Flow Calorimetry and the PandoraPFA Algorithm*. Nuclear Instruments and Methods in Physics Research, Section A: Accelerators, Spectrometers, Detectors and Associated Equipment, 21 November 2009, Vol.611(1), pp.25-40
- [170] ZEUS Experiment. 2014. *The ZEUS Experiment*. [Online]. [Accessed 25 March 2015]. Available from: <http://www-zeus.desy.de/>
- [171] M. Derrick, et al., *Design and construction of the ZEUS barrel calorimeter*. Nucl. Instrum. Methods A, 1991, Vol.309
- [172] M. Thomson, “Modern particle physics,”
- [173] J. de Favereau *et al.* [DELPHES 3 Collaboration], “DELPHES 3, A modular framework for fast simulation of a generic collider experiment,” JHEP **1402** (2014) 057 [arXiv:1307.6346 [hep-ex]].
- [174] G. Moortgat-Pick, T. Abe, G. Alexander, B. Ananthanarayan, A. A. Babich, V. Bharadwaj, D. Barber and A. Bartl *et al.*, “The Role of polarized positrons and electrons in revealing fundamental interactions at the linear collider,” Phys. Rept. **460** (2008) 131 [hep-ph/0507011].
- [175] Density of Materials, <http://www.psyclops.com/tools/technotes/materials/density.html>, (2015).

## A MSSM and NMSSM slha file outputs for the benchmarks used throughout the report

### MSSM01

```

Block MINPAR          # SUSY breaking input parameters
  3   2.00000000e+01  # tanb, DRbar, Feynman gauge
  4   1.00000000e+00  # sign(mu)
  1   3.00000000e+02  # m0
  2   2.00000000e+03  # m12
  5   -2.00000000e+03 # A0
Block EXTPAR          # scale of SUSY breaking BCs
  0   1.17996451e+16  # MX scale
# SOFTSUSY-specific non SLHA information:
# MIXING=0 Desired accuracy=1.00000000e-06 Achieved accuracy=8.20996926e-07
Block MASS             # Mass spectrum
# PDG code      mass      particle
  24    8.03981703e+01  # MW
  25    1.25399821e+02  # h0
  35    2.64569984e+03  # H0
  36    2.64569456e+03  # A0
  37    2.64703927e+03  # H+
1000021   4.15079711e+03  # ~g
1000022   8.75744929e+02  # ~neutralino(1)
1000023   1.63664321e+03  # ~neutralino(2)
1000024   1.63680642e+03  # ~chargino(1)
1000025   -2.50984233e+03 # ~neutralino(3)
1000035   2.51313843e+03  # ~neutralino(4)
1000037   2.51357193e+03  # ~chargino(2)
1000001   3.75568277e+03  # ~d_L
1000002   3.75497496e+03  # ~u_L
1000003   3.75564929e+03  # ~s_L
1000004   3.75494148e+03  # ~c_L
1000005   3.33402417e+03  # ~b_1
1000006   2.75843706e+03  # ~t_1
1000011   1.34558153e+03  # ~e_L
1000012   1.34297769e+03  # ~nue_L
1000013   1.34545510e+03  # ~mu_L
1000014   1.34285104e+03  # ~numu_L
1000015   6.45437280e+02  # ~stau_1
1000016   1.29995066e+03  # ~nu_tau_L
2000001   3.56534694e+03  # ~d_R
2000002   3.58484117e+03  # ~u_R
2000003   3.56528944e+03  # ~s_R
2000004   3.58482717e+03  # ~c_R
2000005   3.46958547e+03  # ~b_2
2000006   3.35275011e+03  # ~t_2
2000011   8.04517994e+02  # ~e_R
2000013   8.04090685e+02  # ~mu_R
2000015   1.30524506e+03  # ~stau_2

```

### NMSSM01

```

BLOCK MINPAR
  3   2.00000000E+00  # TANBETA(MZ)
BLOCK EXTPAR
  1   4.50000000E+02  # M1

```

```

2      9.0000000E+02    # M2
3      2.7000000E+03    # M3
11     1.2000000E+03    # ATOP
12     1.5000000E+02    # ABOTTOM
13     1.0000000E+03    # ATAU
16     1.0000000E+03    # AMUON
31     5.0000000E+02    # LEFT SELECTRON
32     5.0000000E+02    # LEFT SMUON
33     5.0000000E+02    # LEFT STAU
34     5.0000000E+02    # RIGHT SELECTRON
35     5.0000000E+02    # RIGHT SMUON
36     5.0000000E+02    # RIGHT STAU
41     1.0000000E+03    # LEFT 1ST GEN. SQUARKS
42     1.0000000E+03    # LEFT 2ND GEN. SQUARKS
43     1.0000000E+03    # LEFT 3RD GEN. SQUARKS
44     1.0000000E+03    # RIGHT U-SQUARKS
45     1.0000000E+03    # RIGHT C-SQUARKS
46     1.0000000E+03    # RIGHT T-SQUARKS
47     1.0000000E+03    # RIGHT D-SQUARKS
48     1.0000000E+03    # RIGHT S-SQUARKS
49     1.0000000E+03    # RIGHT B-SQUARKS
61     6.6150000E-01    # LAMBDA
62     2.0280000E-01    # KAPPA
63     1.0000000E+02    # ALAMBDA
64     -5.0000000E+02   # AKAPPA
65     3.0000000E+02    # MUEFF
#
# 66     2.09585229E+06   # XIF
# 67     -7.09378643E+08  # XIS
124    1.90000000E+03   # MA AT QSTS
125    1.00000000E+02   # MP AT QSTS
#
BLOCK MASS  # Mass spectrum
# PDG Code    mass          particle
25      1.26079708E+02  # lightest neutral scalar
35      1.23958671E+03  # second neutral scalar
45      1.87850515E+03  # third neutral scalar
36      9.98509634E+01  # lightest pseudoscalar
46      1.87908002E+03  # second pseudoscalar
37      1.87733076E+03  # charged Higgs
1000001 9.02697944E+02 # ~d_L
2000001 9.01734736E+02 # ~d_R
1000002 9.00553125E+02 # ~u_L
2000002 9.01083267E+02 # ~u_R
1000003 9.02697944E+02 # ~s_L
2000003 9.01734736E+02 # ~s_R
1000004 9.00553125E+02 # ~c_L
2000004 9.01083267E+02 # ~c_R
1000005 9.01695262E+02 # ~b_1
2000005 9.02744187E+02 # ~b_2
1000006 7.88985521E+02 # ~t_1
2000006 1.02200119E+03 # ~t_2
1000011 5.01264188E+02 # ~e_L
2000011 5.01102780E+02 # ~e_R
1000012 4.97624575E+02 # ~nue_L
1000013 5.01264188E+02 # ~mu_L
2000013 5.01102780E+02 # ~mu_R

```

```

1000014    4.97624575E+02  # ~numu_L
1000015    5.00472440E+02  # ~tau_1
2000015    5.01899826E+02  # ~tau_2
1000016    4.97624575E+02  # ~nutau_L
1000021    2.59767358E+03  # ~g
1000022    1.96075734E+02  # neutralino(1)
1000023    2.99719658E+02  # neutralino(2)
1000025    -3.29280270E+02 # neutralino(3)
1000035    4.56150968E+02  # neutralino(4)
1000045    9.15392033E+02  # neutralino(5)
1000024    2.96342477E+02  # chargino(1)
1000037    9.15336072E+02  # chargino(2)

```

## NMSSM02

```

BLOCK MINPAR
 3    2.00000000E+00  # TANBETA(MZ)
BLOCK EXTPAR
 1    4.50000000E+02  # M1
 2    9.00000000E+02  # M2
 3    2.70000000E+03  # M3
11    1.20000000E+03  # ATOP
12    1.50000000E+02  # ABOTTOM
13    1.00000000E+02  # ATAU
16    1.00000000E+02  # AMUON
31    1.00000000E+03  # LEFT SELECTRON
32    1.00000000E+03  # LEFT SMUON
33    1.00000000E+03  # LEFT STAU
34    1.00000000E+03  # RIGHT SELECTRON
35    1.00000000E+03  # RIGHT SMUON
36    1.00000000E+03  # RIGHT STAU
41    1.00000000E+03  # LEFT 1ST GEN. SQUARKS
42    1.00000000E+03  # LEFT 2ND GEN. SQUARKS
43    1.00000000E+03  # LEFT 3RD GEN. SQUARKS
44    1.00000000E+03  # RIGHT U-SQUARKS
45    1.00000000E+03  # RIGHT C-SQUARKS
46    1.00000000E+03  # RIGHT T-SQUARKS
47    1.00000000E+03  # RIGHT D-SQUARKS
48    1.00000000E+03  # RIGHT S-SQUARKS
49    1.00000000E+03  # RIGHT B-SQUARKS
61    6.61500000E-01  # LAMBDA
62    2.02800000E-01  # KAPPA
63    1.00000000E+02  # ALAMBDA
64    -5.00000000E+02 # AKAPPA
65    3.00000000E+02  # MUEFF
# 66    2.33167965E+06  # XIF
# 67    -7.96137640E+08 # XIS
124   2.00000000E+03  # MA AT QSTS
125   1.00000000E+02  # MP AT QSTS
#
BLOCK MASS  # Mass spectrum
# PDG Code      mass          particle
 25    1.26636803E+02  # lightest neutral scalar
 35    1.31336094E+03  # second neutral scalar
 45    1.97773746E+03  # third neutral scalar
 36    9.98641655E+01  # lightest pseudoscalar
 46    1.97829395E+03  # second pseudoscalar

```

```

37      1.97663786E+03  # charged Higgs
1000001  9.02695765E+02  # ~d_L
2000001  9.01734366E+02  # ~d_R
1000002  9.00554940E+02  # ~u_L
2000002  9.01084006E+02  # ~u_R
1000003  9.02695765E+02  # ~s_L
2000003  9.01734366E+02  # ~s_R
1000004  9.00554940E+02  # ~c_L
2000004  9.01084006E+02  # ~c_R
1000005  9.01694804E+02  # ~b_1
2000005  9.02742096E+02  # ~b_2
1000006  7.88987855E+02  # ~t_1
2000006  1.02200129E+03  # ~t_2
1000011  1.00063147E+03  # ~e_L
2000011  1.00055091E+03  # ~e_R
1000012  9.98816571E+02  # ~nue_L
1000013  1.00063147E+03  # ~mu_L
2000013  1.00055091E+03  # ~mu_R
1000014  9.98816571E+02  # ~numu_L
1000015  1.00014686E+03  # ~tau_1
2000015  1.000103848E+03  # ~tau_2
1000016  9.98816571E+02  # ~nutau_L
1000021  2.59767357E+03  # ~g
1000022  1.96120541E+02  # neutralino(1)
1000023  2.99979786E+02  # neutralino(2)
1000025  -3.29304652E+02  # neutralino(3)
1000035  4.58648358E+02  # neutralino(4)
1000045  9.22179038E+02  # neutralino(5)
1000024  2.96474104E+02  # chargino(1)
1000037  9.22124871E+02  # chargino(2)

```

### NMSSM03

```

BLOCK MINPAR
 3      2.00000000E+00  # TANBETA(MZ)
BLOCK EXTPAR
 1      4.50000000E+02  # M1
 2      9.00000000E+02  # M2
 3      2.70000000E+03  # M3
11      1.20000000E+03  # ATOP
12      1.50000000E+02  # ABOTTOM
13      1.00000000E+03  # ATAU
16      1.00000000E+03  # AMUON
31      1.47000000E+03  # LEFT SELECTRON
32      1.47000000E+03  # LEFT SMUON
33      1.47000000E+03  # LEFT STAUP
34      1.47000000E+03  # RIGHT SELECTRON
35      1.47000000E+03  # RIGHT SMUON
36      1.47000000E+03  # RIGHT STAUP
41      9.00000000E+02  # LEFT 1ST GEN. SQUARKS
42      9.00000000E+02  # LEFT 2ND GEN. SQUARKS
43      9.00000000E+02  # LEFT 3RD GEN. SQUARKS
44      9.00000000E+02  # RIGHT U-SQUARKS
45      9.00000000E+02  # RIGHT C-SQUARKS
46      9.00000000E+02  # RIGHT T-SQUARKS
47      1.00000000E+03  # RIGHT D-SQUARKS

```

```

48      1.0000000E+03  # RIGHT S-SQUARKS
49      1.0000000E+03  # RIGHT B-SQUARKS
61      6.6150000E-01  # LAMBDA
62      2.0280000E-01  # KAPPA
63      1.0000000E+02  # ALAMBDA
64      -5.0000000E+02 # AKAPPA
65      3.0000000E+02  # MUEFF
# 66      2.33428522E+06 # XIF
# 67      -7.96759478E+08 # XIS
124     2.0000000E+03  # MA AT QSTSB
125     1.0000000E+02  # MP AT QSTSB
#
BLOCK MASS  # Mass spectrum
# PDG Code   mass       particle
    25      1.27415528E+02 # lightest neutral scalar
    35      1.31433527E+03 # second neutral scalar
    45      1.98129020E+03 # third neutral scalar
    36      9.99803035E+01 # lightest pseudoscalar
    46      1.98184054E+03 # second pseudoscalar
    37      1.98017572E+03 # charged Higgs
1000001  7.53387027E+02 # ~d_L
2000001  8.76641204E+02 # ~d_R
1000002  7.50798342E+02 # ~u_L
2000002  7.51439590E+02 # ~u_R
1000003  7.53387027E+02 # ~s_L
2000003  8.76641204E+02 # ~s_R
1000004  7.50798342E+02 # ~c_L
2000004  7.51439590E+02 # ~c_R
1000005  7.42470016E+02 # ~b_1
2000005  8.67680892E+02 # ~b_2
1000006  5.91540890E+02 # ~t_1
2000006  8.87646999E+02 # ~t_2
1000011  1.47043167E+03 # ~e_L
2000011  1.47037557E+03 # ~e_R
1000012  1.46919242E+03 # ~nue_L
1000013  1.47043167E+03 # ~mu_L
2000013  1.47037557E+03 # ~mu_R
1000014  1.46919242E+03 # ~numu_L
1000015  1.47016120E+03 # ~tau_1
2000015  1.47064815E+03 # ~tau_2
1000016  1.46919242E+03 # ~nutau_L
1000021  2.59443039E+03 # ~g
1000022  1.95898562E+02 # neutralino(1)
1000023  2.99743749E+02 # neutralino(2)
1000025  -3.28943774E+02 # neutralino(3)
1000035  4.60067876E+02 # neutralino(4)
1000045  9.23414343E+02 # neutralino(5)
1000024  2.96111349E+02 # chargino(1)
1000037  9.23360446E+02 # chargino(2)

```

## B Total Ionisation Energy Loss (IEL) in the collider

The total energy loss due to ionisation by a particle is given by

$$IEL = \frac{\partial E}{\partial x} \sum (\rho_X \cdot r_X) \quad (B.1)$$

where X denotes a certain material, and  $\rho$  and  $r$  are the density of that material in  $gcm^{-3}$ , and it's radial distance in cm respectively.

There are 4 main components in the detector that cause ionisation losses. The tracker, The electronic calorimeter (ECAL), the hadronic calorimeter (HCAL) and the muon tracker. The summation is done over every material in these four detectors.

The relevant parameters for this calcualtion are as follows; The tracker is made mainly of silicon and is 106.5cm long radially, as seen in section 5.6, the ECAL is 16.5cm long and is made up of 12cm of Tungsten and 4.5cm of Silicon, as seen in section 5.7, the HCAL is 199cm long and is made up of Steel, as seen in section 5.8, and the muon tracker is 206.8cm long and is made up of 180cm Steel and 26.8cm Titanium Oxide as seen in section 5.9. As the densities of Silicon, Tungsten, Iron and Titanium Oxide are 2.33, 19.4, 7.87 and 4.25  $gcm^{-3}$  respectively [175]. The total Ionisation energy loss is therefore equal to;

$$\begin{aligned} IEL &= \frac{\partial E}{\partial x} (\rho_{Si} \cdot r_{Si} + \rho_W \cdot r_W + \rho_{Fe} \cdot r_{Fe} + \rho_{TiO_2} \cdot r_{TiO_2}) \\ &= 5.77 \times ((2.23 \times (106.5 + 4.5)) + 19.4 \times 12 + 7.87 \times (199 + 180) + 26.8 \times 4.25) MeV \\ &= 20,617 MeV = 20.62 GeV \end{aligned} \quad (B.2)$$

## C GuineaPig Data Plots

This appendix contains the histograms and CDFs produced from the GuineaPig data for centre of mass energies 300GeV, 1TeV and 6TeV. These plots show the energy spread within the simulated bunches and were used to calculate the beam efficiencies for use by the SUSY and Z' research groups. All histograms have twenty bins, making each of a width corresponding to an energy range of 5% of the initial beam energy, except the refined 6TeV histograms, which have one hundred bins and so have width corresponding to a 1% energy range.

### C.1 300 GeV Centre of Mass Energy plots

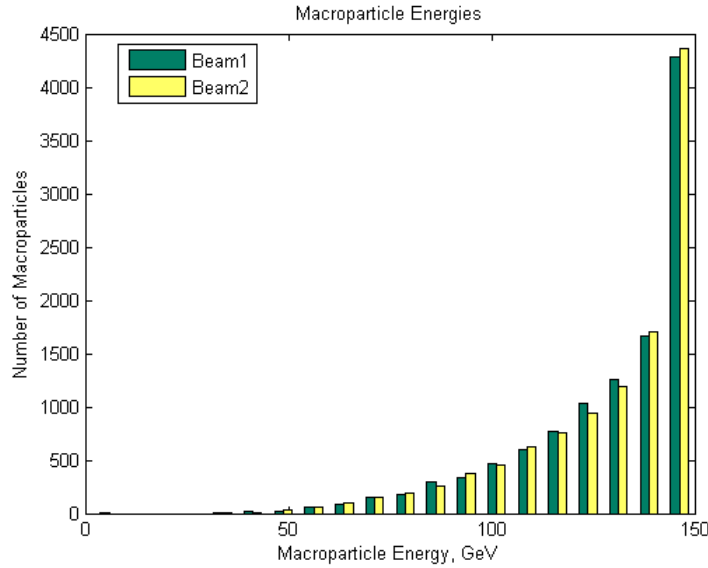


Figure C.1: The distribution of macro-particle energy after beam-beam interactions for a 300 GeV centre of mass.

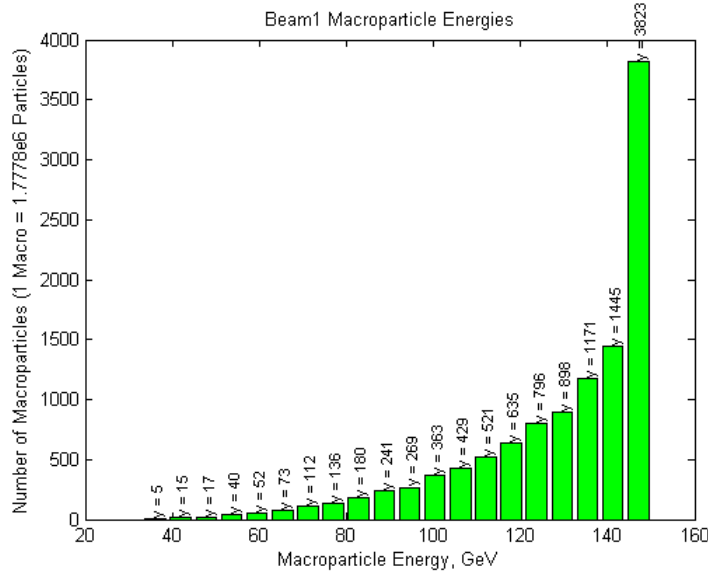


Figure C.2: The distribution of macro-particle energy within Beam 1, after beam-beam interactions, for a 300 GeV centre of mass.

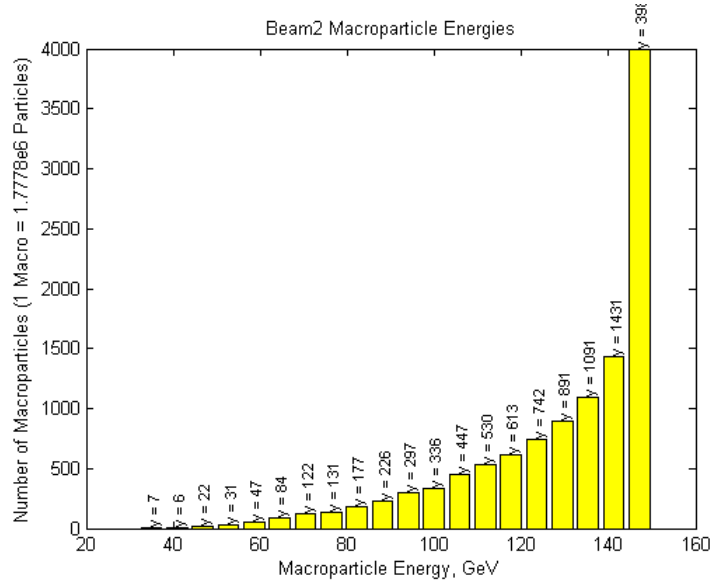


Figure C.3: The distribution of macro-particle energy within Beam 2, after beam-beam interactions, for a 300 GeV centre of mass.

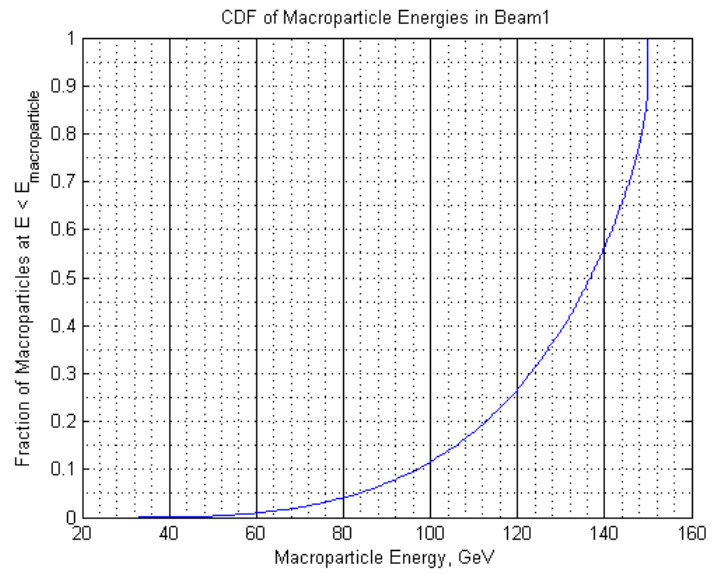


Figure C.4: The cumulative frequency distribution of macro-particle energy within Beam 1, after beam-beam interactions, for a 300 GeV centre of mass.

## C.2 1 TeV Centre of Mass Energy plots

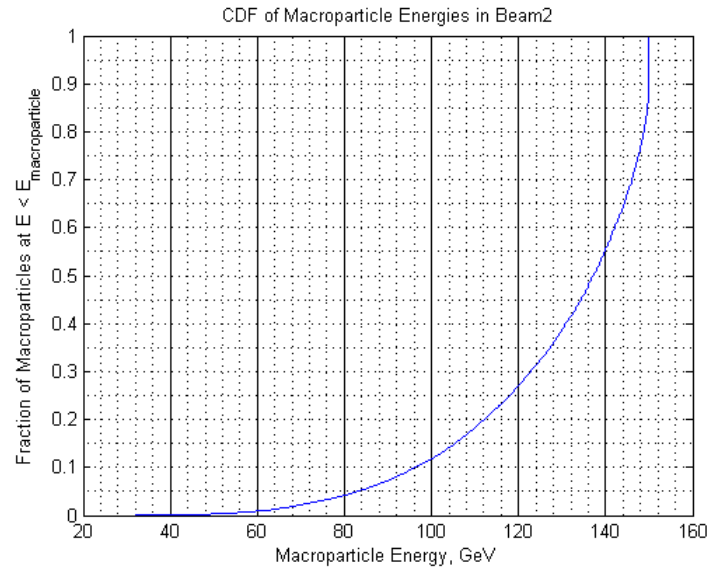


Figure C.5: The cumulative frequency distribution of macro-particle energy within Beam 2, after beam-beam interactions, for a 300 GeV centre of mass.

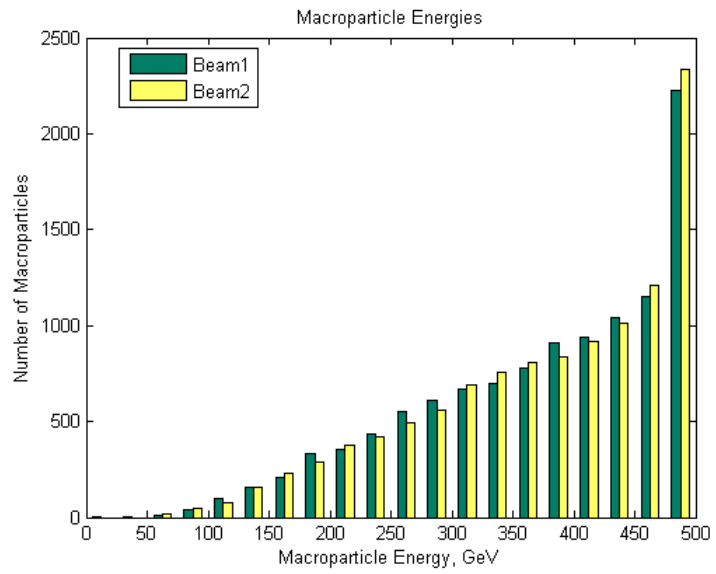


Figure C.6: The distribution of macro-particle energy after beam-beam interactions for a 1 TeV centre of mass.

### C.3 6 TeV Centre of Mass Energy plots

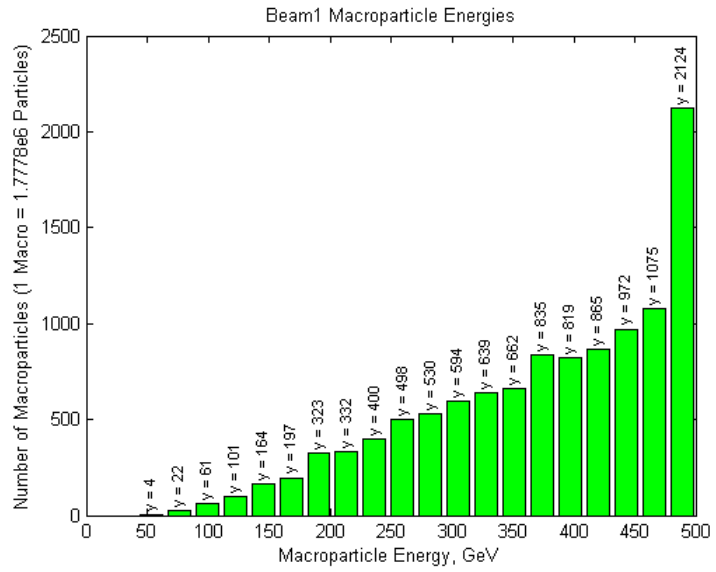


Figure C.7: The distribution of macro-particle energy within Beam 1, after beam-beam interactions, for a 1 TeV centre of mass.

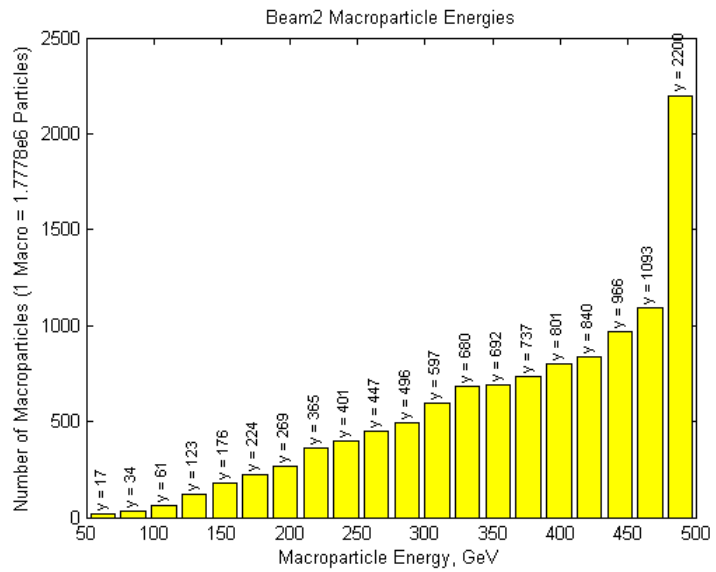


Figure C.8: The distribution of macro-particle energy within Beam 2, after beam-beam interactions, for a 1 TeV centre of mass.

#### C.4 Refined 6 TeV Centre of Mass Energy plots

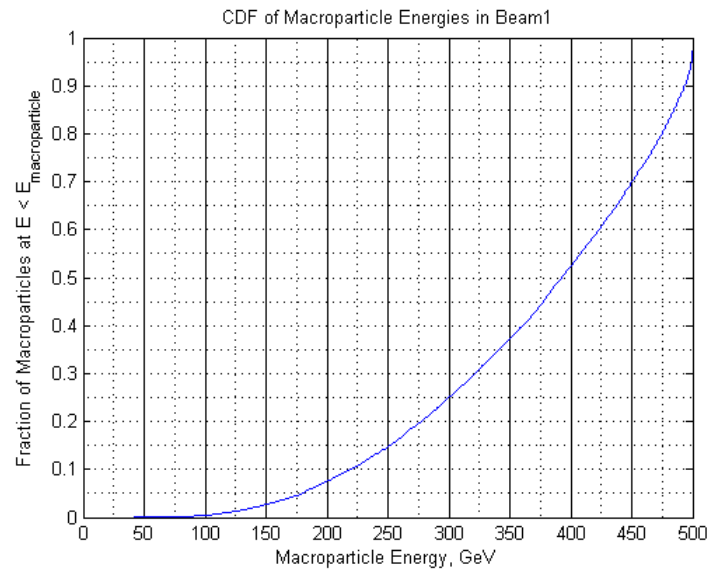


Figure C.9: The cumulative frequency distribution of macro-particle energy within Beam 1, after beam-beam interactions, for a 1 TeV centre of mass.

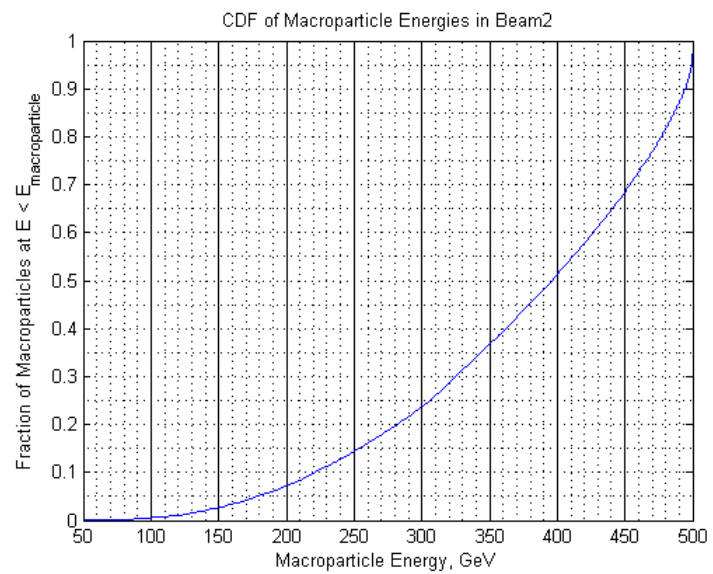


Figure C.10: The cumulative frequency distribution of macro-particle energy within Beam 2, after beam-beam interactions, for a 1 TeV centre of mass.

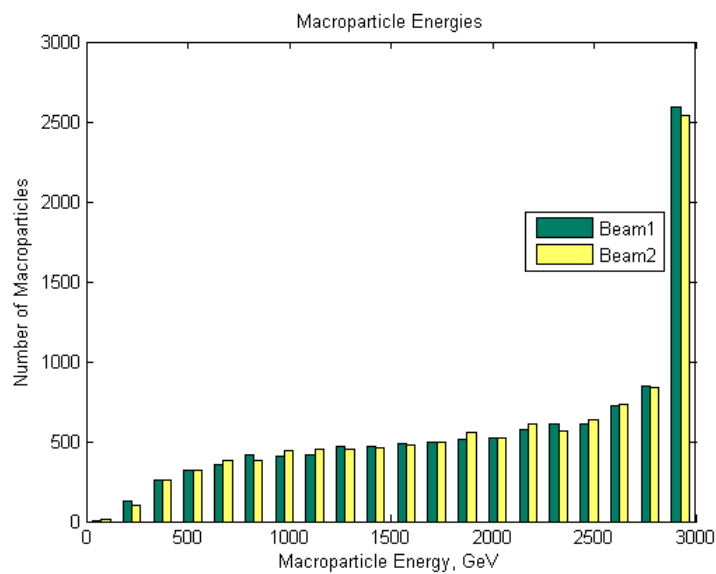


Figure C.11: The distribution of macro-particle energy after beam-beam interactions for a 6 TeV centre of mass.

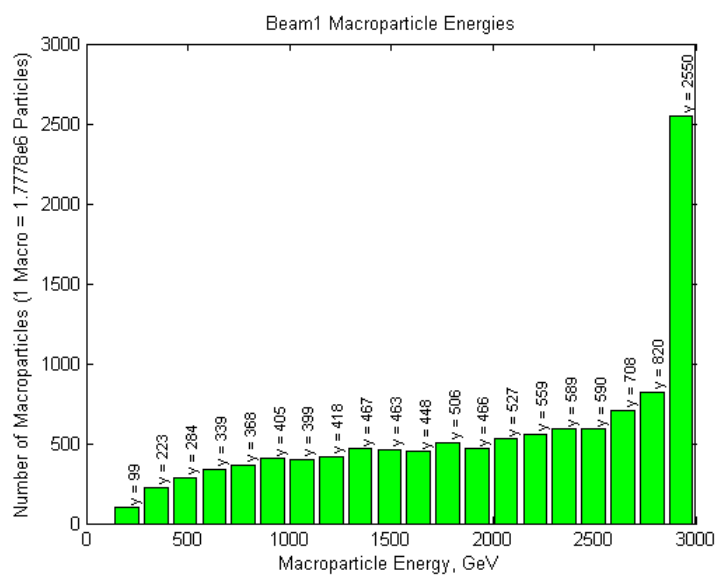


Figure C.12: The distribution of macro-particle energy within Beam 1, after beam-beam interactions, for a 6 TeV centre of mass.

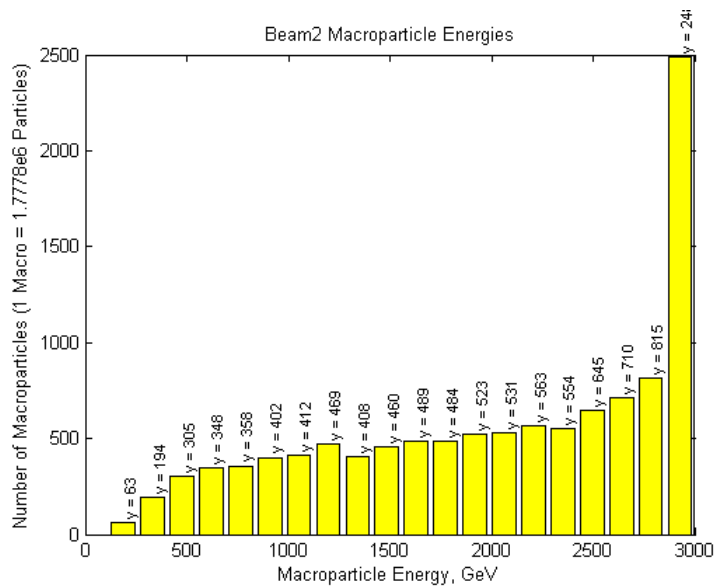


Figure C.13: The distribution of macro-particle energy within Beam 2, after beam-beam interactions, for a 6 TeV centre of mass.

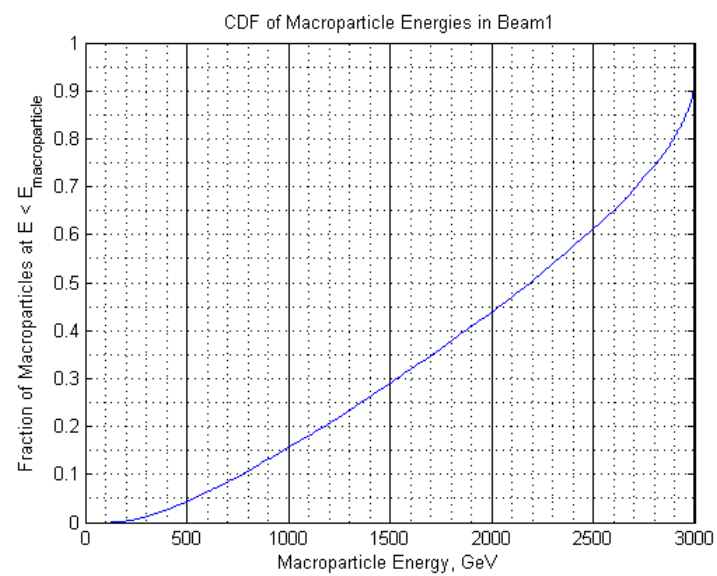


Figure C.14: The cumulative frequency distribution of macro-particle energy within Beam 1, after beam-beam interactions, for a 6 TeV centre of mass.

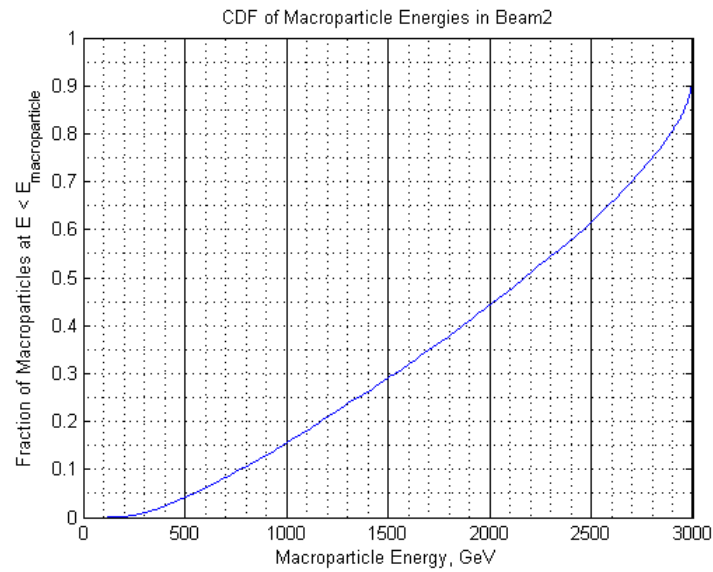


Figure C.15: The cumulative frequency distribution of macro-particle energy within Beam 2, after beam-beam interactions, for a 6 TeV centre of mass.

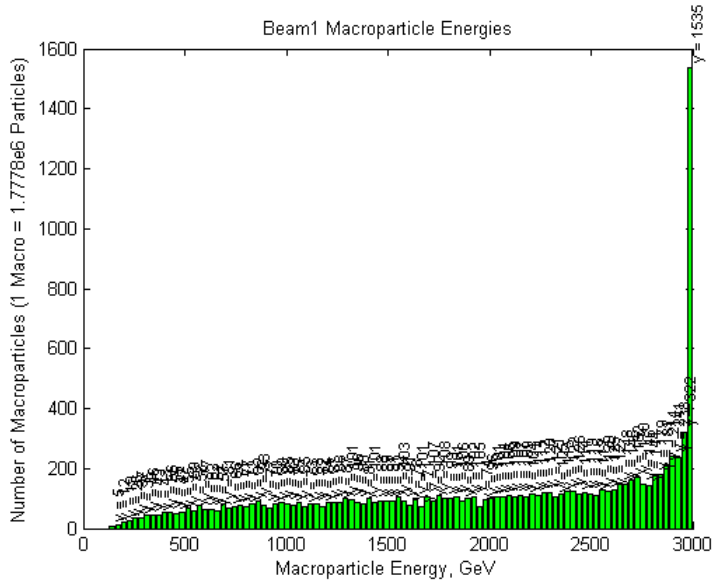


Figure C.16: A 100 bin histogram of the distribution of macro-particle energy within Beam 1, after beam-beam interactions, for a 6 TeV centre of mass.

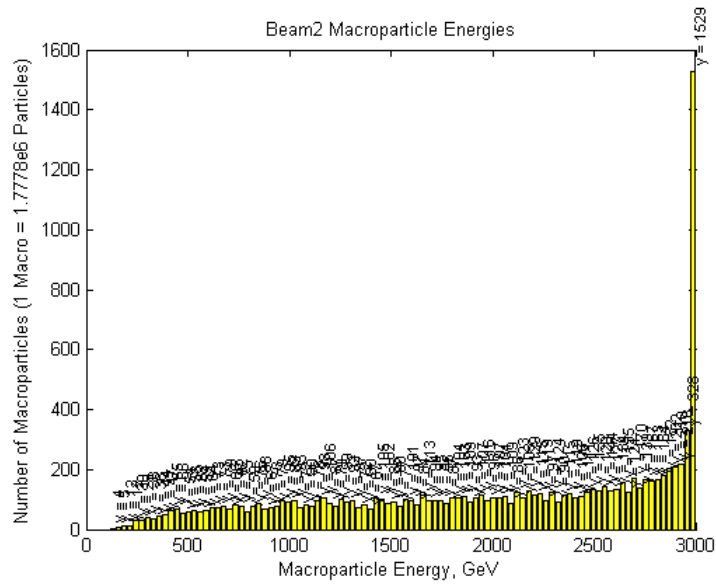


Figure C.17: A 100 bin histogram of the distribution of macro-particle energy within Beam 2, after beam-beam interactions, for a 6 TeV centre of mass.